

CONTENTS

Introduction	1
1 The Standard Model and Supersymmetry	3
1.1 The Standard Model	3
1.1.1 Electroweak Symmetry Breaking and the Higgs mechanism	6
1.1.2 Limitations of the Standard Model	9
1.2 Supersymmetry and the MSSM	11
1.2.1 Minimal Supersymmetric Standard Model	13
1.2.2 Phenomenology of Supersymmetry	15
2 The ATLAS Experiment at the LHC	20
2.1 The LHC	20
2.2 The ATLAS Detector	22
2.2.1 The Magnet System	24
2.2.2 The Inner Detector	25
2.2.3 The Calorimeters	28
2.2.4 The Muon Spectrometer	29
2.3 The ATLAS Trigger System	31
3 The ATLAS Trigger System	32
3.1 Overview	32
3.2 Level-1 Trigger	34
3.3 High-Level Trigger	36
3.3.1 Inner detector tracking	36
3.3.2 Performance of HLT	37
4 Event Simulation and Object Reconstruction	43
4.1 Generation of Monte Carlo-simulated events	44
4.2 Object Reconstruction	47
5 Analysis strategy and optimisation	57

5.1	SUSY signals	57
5.1.1	Benchmark processes	58
5.1.2	MC samples	59
5.2	Objects definition	59
5.3	Triggers used	61
5.4	Event selection	61
5.4.1	Event cleaning	62
5.5	Standard Model backgrounds	62
5.5.1	MC samples	64
5.6	Signal Regions optimisation	64
5.6.1	Preliminary selection and discriminating key variables	65
5.6.2	Optimisation strategy	68
6	Background estimation	76
6.1	Nominal background estimation	76
6.1.1	Control regions	78
6.1.2	Validation regions	79
6.2	Estimation of the irreducible background	80
6.3	Systematic uncertainties	84
6.3.1	Experimental uncertainties	84
6.3.2	Theory uncertainties	88
7	Results and statistical interpretation	90
7.1	Statistical analysis	90
7.1.1	Estimation of the parameters and the statistical hypothesis testing . . .	91
7.1.2	Discovery and exclusion	94
7.2	Results and Interpretation	94
7.2.1	Background-only fit	94
7.2.2	Opening Pandora's box: unblinded Signal Regions (SRs)	96
7.2.3	Setting the limits	100
Conclusions		106
A	$t\bar{t}+Z$ estimation for a Dark Matter search	108
A.1	Overview of the analysis	108
A.2	The estimation of the irreducible $t\bar{t}+Z$ background	109
A.3	Results	110
B	Summary of the background estimation	114
Glossary		119
Bibliography		123

INTRODUCTION

*The journey, not the destination
matters.*

Thomas S. Eliot

One of the first connection between space-time symmetries and the conservation laws of physics was drawn by Emmy Noether. An informal statement of her theorem could be “*If a system has a continuous symmetry property, then there are corresponding quantities whose values are conserved in time*” [1], which means for example that the symmetry of the laws of physics under time translation result in the conservation of energy, or that a symmetry under spatial translation results in the conservation of momentum.

The Higgs boson discovery in 2012 by the ATLAS and CMS collaborations was a milestone in the scope of particle physics [2, 3]. However, it did leave some unanswered questions. When attempting a unified description of the weak force and the electromagnetic force, whose intensities are enormously different, the interactions of the Higgs field with the so-called gauge bosons break the symmetry. It is known that the gauge bosons of the Standard Model (SM), W and Z , acquire mass through their interactions with the Higgs field, but the photon does not, resulting in a huge difference in terms of interaction range: finite for W and the Z , infinite for the photon. Kenneth Wilson in the early 1970’s noticed a problem that today is known as the *hierarchy problem*: the Higgs boson, that gives mass to all fundamental particles, and to itself, happens to have a mass that is theoretically unstable and around a factor of 10^{16} larger than the electroweak scale. Such difference is considered “unnatural”. Around the same time, a new symmetry was proposed: Supersymmetry (SUSY). Such theory essentially extends the space-time symmetries into the quantum domain connecting classical quantities, such as space and time, to the spin of a particle. Most importantly, SUSY gives rise to a particle that fits in with all the characteristics of a dark matter candidate, providing at the same time a natural solution to the hierarchy problem by cancelling the terms in the calculation of the Higgs boson mass, arising from interactions of the Higgs boson with SM particles.

The work presented in this thesis was carried out during a 3.5-year PhD on the ATLAS experiment at the Large Hadron Collider (LHC) within the scope of a third-generation SUSY search:

the search for the supersymmetric partner of the top quark in final states with jets and missing transverse momentum that was published in a paper in the Journal of High Energy Physics in September 2017 [4]. This analysis was carried out as part of the A Toroidal LHC ApparatuS (ATLAS) collaboration and as it can be non-trivial to isolate the work of a person from the collaboration, it is fair to state that the work presented here is a combination of the work carried out both by the author and by other members of the ATLAS collaboration. In particular, Chapters 1, 2, and 4 do not contain work carried out by the author but rather a description of the theoretical framework, the experimental setup relevant for the scope in which this thesis is positioned, and the techniques used to reconstruct the physics objects needed to perform the analyses; Chapter 3 contains both the description of the trigger, which is the work of other members of the ATLAS collaboration, and the author’s contribution on the evaluation of the performance of the inner detector trigger; Chapters 5 and 6 present the analysis carried out by the author as part of the *stop zero-lepton* analysis team within the ATLAS-SUSY working group. The author contributed to the analysis effort providing an optimisation strategy of the regions in which the SUSY signal was searched for, and a data-driven technique for the estimation of the irreducible background $t\bar{t} + Z(\rightarrow \nu\nu)$ and its relative theory uncertainties; finally, Chapter 7 does not contain any author’s contribution but rather an overview of the statistical tools used to produce the results of this analysis, such as the fit.

THE STANDARD MODEL AND SUPERSYMMETRY

1

A theory is something nobody believes, except the person who made it. An experiment is something everybody believes, except the person who made it.

Albert Einstein

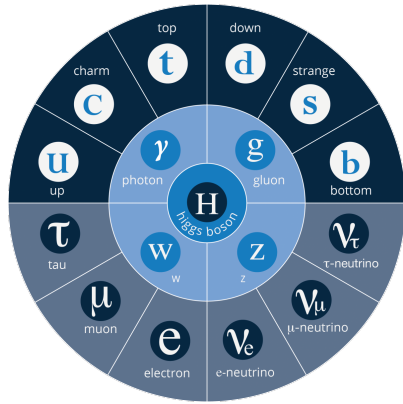


Figure 1.1: The elementary particles of the SM. From the outermost to the innermost; fermions (quarks, top-half wheel, leptons, bottom-half wheel), vector bosons, and the Higgs boson.

Section 1.1 presents an overview of the SM of particle physics, together with its limitations (Section 1.1.2) and the need of an extension. One of the most popular of these extensions, SUSY, will be discussed in Section 1.2 where an overview of the theory and the motivations behind its success will be presented. The description of the Minimal Supersymmetric Standard Model (MSSM) in Section 1.2.1, and finally the phenomenology of supersymmetry, with particular attention to third-generation supersymmetry - as the most relevant theoretical support to this work - will be discussed in Section 1.2.2.

1.1 The Standard Model

The SM is an effective theory that aims to provide a general description of fundamental particles and their interactions.

The 20th century can be considered a quantum revolution. Several experiments led to discoveries which were found to be, together with the formalised theory, a solid base of the SM of particle physics and our description of nature. Several particles were first predicted and then

experimentally observed e. g. the W and the Z bosons, the τ lepton, [5], and more recently the Higgs boson at the LHC discovered by the ATLAS [2] and CMS [3] collaborations.

The SM is a Quantum Field Theory (QFT) where particles are treated like excitations of quantum fields in a four-dimensional Minkowski space-time [6]. It can describe three of the four fundamental forces; weak, electromagnetic, and strong, but not gravity.

The most general classification of the elementary particles within the SM can be made by means of spin and their behaviour under Poincaré transformations [7]: *fermions* (leptons and quarks), usually referred to as matter particles, which have half-integer spin values, in unit of \hbar , and *bosons*, usually referred to as information carriers, which have integer-spin values. A noteworthy subset of bosons is formed by the Spin-1 bosons, also known as gauge bosons. These can be considered mediators of the forces. Figure 1.1 displays the elementary particles of the Standard Model known as of today.

Symmetries and Gauge Groups

In 1915, the German mathematician and theoretical physicist Emmy Noether (23 March 1882 – 14 April 1935) proved that every differentiable symmetry of the action - defined as the integral over space of a Lagrangian density function $S = \int \mathcal{L} dt$ - of a physical system has a corresponding conservation law [8]. More generally, a symmetry is a property of a physical system and under certain transformations this property is preserved.

A gauge theory in QFT, is a theory in which the Lagrangian is invariant under a continuous group of local transformations. Group theory was adopted to describe the symmetries conserved in the SM. The gauge group of the SM is the *Lie Group* which contains all the transformations between possible gauges [7]. The Lie algebra of group generators is associated to any Lie group and for each group generator there emerges a corresponding field, called the gauge field, and the quanta of such fields are called *gauge bosons*.

The three SM interactions can therefore be mathematically described by the following:

$$U(1)_Y \otimes SU(2)_L \otimes SU(3)_C \quad (1.1)$$

Here, Y is the weak hypercharge, used to estimate the correlation between the electric charge (Q) and the third component of the weak isospin (I_3) via the relation $Q = I_3 + Y/2$, where I_3 can either be $\pm 1/2$ or 0 for left-handed and right-handed particles, respectively; L the left-handedness; and C the colour charge.

Quantum Electrodynamics (QED) is an Abelian gauge theory described by the symmetry group $U(1)$. The electromagnetic four-potential is its gauge field and the photon its gauge boson [9]. The interactions between charged fermions occurs by the exchange of a massless photon.

The weak interaction is described by the non-Abelian gauge group $SU(2)$. The $SU(2)$ generators are the massless gauge bosons $W_\mu^{\alpha=1,\dots,3}$ and they violate parity by acting only on left-

handed particles. As a consequence of non-Abelianity, $SU(2)$ gauge bosons can self-interact as the generator commutators are non-vanishing. Additionally, quarks can also interact through weak interaction as mixtures of SM eigenstates as described by the CKM matrix [10].

Finally, the strong interaction, described by the symmetry group $SU(3)$, has eight massless gauge bosons, the gluons, $G_\mu^{\alpha=1,\dots,8}$ which can be exchanged between quarks and can also self-interact.

Fermions

There are twelve fermions in the SM: six quarks and six leptons. In particular, fermions can be grouped into three generations. Each generation contains four particles; one up- and one down-type quark, one charged lepton and one neutral lepton. The masses of the charged leptons and quarks increase with the generation. The six quarks of the SM can be grouped into three $SU(2)$ doublets;

$$\begin{pmatrix} u \\ d \end{pmatrix}, \quad \begin{pmatrix} c \\ s \end{pmatrix}, \quad \begin{pmatrix} t \\ b \end{pmatrix}$$

The up-type quarks (*up, charm, top*) have charge $+\frac{2}{3}e$ and the down-type quarks (*down, strange, beauty/bottom*) have charge $-\frac{1}{3}e$, where e is the electron charge. Quarks also have another quantum number that can be seen as the analogue of the electric charge; the colour charge. This can exist in three different states; *red, green* and *blue*, but they cannot exist as free particles. They rather group to form hadronic matter, also known as *hadrons*. There are two kinds of hadrons; mesons and baryons. Mesons are quark-antiquark systems, e. g. the pion, and baryons are three-quark system, e. g. protons and neutrons. Quarks and anti-quarks have a baryon number of $\frac{1}{3}$ and $-\frac{1}{3}$, respectively.

There are six leptons and they can be classified in charged leptons (electron e , muon μ , tau τ) and neutral leptons (electron neutrino ν_e , muon neutrino ν_μ , tau neutrino ν_τ):

$$\begin{pmatrix} \nu_e \\ e^- \end{pmatrix}, \quad \begin{pmatrix} \nu_\mu \\ \mu^- \end{pmatrix}, \quad \begin{pmatrix} \nu_\tau \\ \tau^- \end{pmatrix}$$

Each lepton has a characteristic quantum number, called lepton number (L). Negatively (positively) charged leptons have $L = -1$ ($L = 1$) and neutral leptons have $L = 1$. The lepton number is conserved in all the interactions.

Forces of Nature

Forces in the SM are described by gauge theories, where the interactions are mediated by a vector gauge boson.

QED describes the electromagnetic force, which only affects charged leptons (neutrinos are instead affected by the weak force, mediated by the W^\pm and Z^0 bosons) and quarks and it is mediated by the photon (γ).

The weak interaction is associated with *handedness* i. e., the projection of a particle spin onto its direction of motion. Both leptons and quarks have left- and right-handed components. However, only the left-handed (right-handed) component for neutrinos (anti-neutrinos) has been observed. This means that nature prefers to produce left-handed neutrinos and right-handed anti-neutrinos, which is the so-called *parity violation* [11].

The strong interaction, mediated by the gluon, electrically neutral and massless, is described by Quantum Chromodynamics (QCD). Its coupling (α_s) increases with increasing distance and is smaller at short range. In particular, α_s evolves as a function of the transferred four-momentum squared, Q^2 , as follows:

$$\alpha_s(Q^2) \propto \frac{1}{n_f \log\left(\frac{Q^2}{\Lambda_{\text{QCD}}^2}\right)} \quad (1.2)$$

where n_f is the number of quarks with mass below Q^2 and Λ_{QCD} is the QCD characteristic scale. Eq. 1.2 shows that α_s decreases as a function of Λ_{QCD} , but at the same time it quickly diverges when Q^2 gets closer to Λ . In other words, as the condition $\alpha_s \ll 1$ only holds for $Q^2 \gg \Lambda_{\text{QCD}}$, QCD can be treated perturbatively¹ only at high energy scales². Furthermore, QCD has three important features:

- *confinement*: quarks or gluons cannot be observed as free particles, but only colourless “singlet” states can be observed as “jets”, namely collimated cone-shaped sprays of hadrons;
- *asymptotic freedom*: interactions between quarks and gluons become weaker as the energy scale increases and the corresponding length scale decreases, as $\alpha_s \rightarrow 0$ for $Q^2 \rightarrow \infty$
- *hadronisation*: when quarks or gluons are pulled apart, the production of pairs of hadrons, produced from the vacuum, is energetically preferred to an increase in distance.

Table 1.1 summarises the forces described in the SM and the main characteristics of the mediators. The gravitational force is believed to be mediated by the graviton, but as already mentioned, since it is not included in the SM, it will not be further discussed.

1.1.1 Electroweak Symmetry Breaking and the Higgs mechanism

In 1979 Sheldon Glashow, Abdus Salam, and Steven Weinberg were awarded the Nobel Prize in Physics for their contributions to the so-called electroweak unification [12, 13, 14]. In the

¹ Perturbation theory (quantum mechanics) is an approximation to describe a complicated quantum system in terms of a simpler one.

² Perturbation theory can only be used when the coupling constant (expansion parameter) is small.

Table 1.1: Forces and mediators described by the SM

Force	Name	Symbol	Mass [GeV]	Charge
Electromagnetic	Photon	γ	0	0
Weak	W	W^\pm	80.398	$\pm e$
	Z	Z^0	91.188	0
Strong	Gluon	g	0	0

mathematical description of the SM in 1.1, the electroweak interaction is described by $U(1)_Y \otimes SU(2)_L$.

The four electroweak physical bosons W^\pm , Z and γ are related to the four unphysical gauge bosons $W_\mu^{\alpha=1,\dots,3}$ and B_μ . In particular, to obtain the physical bosons the gauge bosons have to mix as follows;

$$A_\mu = W_\mu^3 \sin \theta_W + B_\mu \cos \theta_W \quad (1.3)$$

$$Z_\mu = W_\mu^3 \cos \theta_W - B_\mu \sin \theta_W \quad (1.4)$$

$$W_\mu^\pm = \frac{1}{\sqrt{2}} \left(W_\mu^1 \mp i W_\mu^2 \right) \quad (1.5)$$

Here, θ_W is the so-called *Weinberg angle* which is the angle by which spontaneous symmetry breaking rotates the original gauge bosons W_μ^3 and B_μ into the physical Z and γ . A_μ and Z_μ are the photon and the Z boson fields, respectively. The θ_W angle can be experimentally determined in terms of the coupling strengths, of the $B_\mu(g_1)$ and the $W_\mu^\alpha(g_2)$ to the fermions, using the relation $\tan \theta_W = g_1/g_2$.

The mass terms for both gauge bosons and fermionic fields are forbidden by the electroweak gauge as they are not invariant under gauge transformations. Nonetheless, it was experimentally proven that W and Z bosons are massive [9], therefore in order for the SM assumption to hold, the electroweak symmetry must be broken.

The SM Lagrangian can be written as the sum of the various Lagrangians describing the three interactions and the masses of the elementary particles as follows:

$$\mathcal{L}_{\text{SM}} = \mathcal{L}_{\text{EWK}} + \mathcal{L}_{\text{QCD}} + \mathcal{L}_{\text{Mass}} \quad (1.6)$$

In order for the SM Lagrangian to remain a re-normalisable theory, the mass terms ($\mathcal{L}_{\text{Mass}}$) cannot be inserted by hand. A mechanism, that can preserve the gauge symmetry in the SM and can solve the inconsistency arisen from the mass difference between the gauge bosons and the physical ones is needed. A British theoretical physicist, Peter Higgs (29 May 1929, Newcastle upon Tyne, UK), came up with a brilliant solution for which he was awarded the Nobel Prize in Physics in 2013. Higgs proposed [15] that broken symmetry in the electroweak theory could

explain the origin of masses of elementary particles, and in particular of W and Z bosons. The mechanism introduces a scalar field, known as the Higgs field, thought to couple to both massive fermions and bosons. The $SU(2)$ doublet is then introduced in the SM;

$$\phi = \begin{pmatrix} \phi^+ \\ \phi^0 \end{pmatrix} \quad (1.7)$$

with ϕ^+ and ϕ^0 generic complex fields:

$$\phi^+ = \frac{\phi_1 + i\phi_2}{\sqrt{2}}, \quad \phi^0 = \frac{\phi_3 + i\phi_4}{\sqrt{2}} \quad (1.8)$$

Consider a Lagrangian of the form:

$$\mathcal{L}_{\text{Higgs}} = (\partial_\mu \phi)^* (\partial^\mu \phi) - V(\phi) \quad (1.9)$$

where $V(\phi)$ is now the Higgs potential. Re-normalisability and $SU(2)_L \otimes U(1)_Y$ invariance require the Higgs potential to be of the following form:

$$V(\phi) = \mu^2 \phi^\dagger \phi + \lambda (\phi^\dagger \phi)^2 \quad (1.10)$$

The Lagrangian in Eq. 1.9 is the Higgs Lagrangian if ϕ is chosen to be the following:

$$\phi = \begin{pmatrix} \phi^+ \\ \phi^0 \end{pmatrix} = \begin{pmatrix} G^+ \\ \frac{1}{\sqrt{2}}(v + H + iG^0) \end{pmatrix}$$

Here, the complex scalar field G^\pm and the real scalar field G^0 correspond to Goldstone bosons, and the real scalar field H is the SM Higgs boson field [16]. These massless scalars are absorbed due to the gauge transformations by the electroweak gauge bosons of the SM:

$$\phi = \begin{pmatrix} \phi^+ \\ \phi^0 \end{pmatrix} = \begin{pmatrix} 0 \\ \frac{1}{\sqrt{2}}(v + H) \end{pmatrix} \quad (1.11)$$

The Higgs potential in Eq. 1.10 is displayed in Figure 1.2 if λ and μ are chosen to be real. Such potential has a non-zero ground state, v , also known as Vacuum Expectation Value (VEV):

$$\phi_0 = \begin{pmatrix} 0 \\ \frac{1}{\sqrt{2}}v \end{pmatrix} \quad (1.12)$$

Such representation remains invariant under $U(1)$ allowing electric charge conservation. However, the SM gauge symmetry 1.1 is broken into $SU(2)_L \otimes U(1)_Y$.

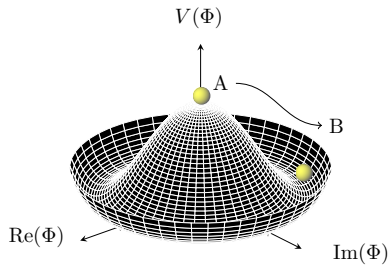


Figure 1.2: The Higgs potential in the complex plane.

In summary, to generate particle masses gauge symmetry must be broken. However, in order for the theory to remain renormalisable, the global Lagrangian symmetry must be preserved. This can be solved introducing the concept of *spontaneous symmetry breaking* (SSB): a mechanism that allows a symmetric Lagrangian, but not a symmetric vacuum. In particular, given a Lagrangian invariant under a certain transformation, T_X , and a generic set of states, that transform under T_X as the elements of a multiplet, the symmetry is spontaneously broken if one of those states is arbitrarily chosen as the ground state of the system. The interaction of the Higgs field with the $SU(2) \otimes U(1)$ gauge fields, $W_\mu^{\alpha=1,2,3}$, result in the three gauge bosons fields acquiring mass whilst the A_μ field remains massless.

1.1.2 Limitations of the Standard Model

The SM has been extensively validated at the Large Electron-Positron Collider (LEP) (European Organization for Nuclear Research (CERN)), Tevatron at Fermilab, and SLAC. Run 1 of the LHC extended the validation beyond the energy limits of previous colliders as shown in Figure 1.3: the agreement, between the measured production cross-section of various SM processes and the SM predictions, looks very good. However, there are some fundamental questions that still have no answer.

Hierarchy Problem

Due to the coupling of the Higgs field to the fermionic fields, the one-loop corrections to the Higgs mass receive several contributions [18]. In particular, looking at Figure 1.4:

$$\Delta m_H^2 = -\frac{|\lambda_f|^2}{8\pi^2} \Lambda_{\text{UV}}^2 + \dots \quad (1.13)$$

where, λ_f is the coupling constant to the fermionic field; Δm_H^2 is the difference between the observed Higgs mass m_H^2 and the bare mass, m_H^0 (Lagrangian parameter); Λ_{UV} is the ultraviolet momentum cut-off, selected to be at the Planck scale ($\sim 2 \cdot 10^{18}$ GeV), at which a QFT description of gravity is believed to become possible. The correction to the Higgs mass will be around 30 orders of magnitude larger than Higgs mass itself, in opposition to what has been measured. This difference just mentioned, between the electroweak scale and the Planck scale arisen from the quantum corrections to the Higgs mass, is the so-called Hierarchy Problem [18].

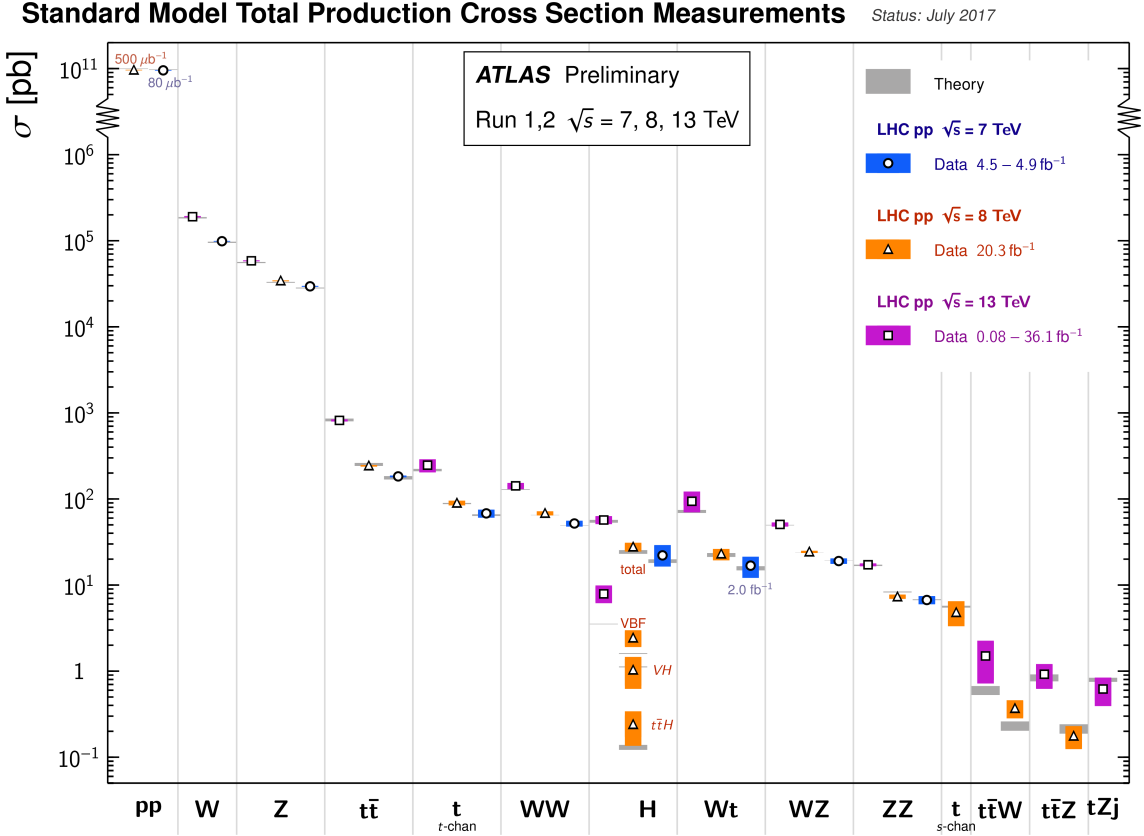


Figure 1.3: Summary of several SM total production cross-section measurements, corrected for leptonic branching fractions, compared to the corresponding theoretical expectations. All theoretical expectations were calculated at NLO or higher. The luminosity used for each measurement is indicated close to the data point. Uncertainties for the theoretical predictions are quoted from the original ATLAS papers. They were not always evaluated using the same prescriptions for PDFs and scales. Not all measurements are statistically significant yet [17].

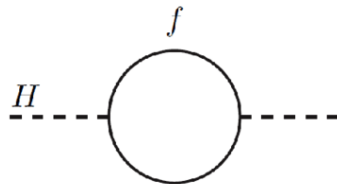


Figure 1.4: One-loop quantum corrections to the Higgs mass. A fermion correction with coupling λ_f .

Neutrino Masses

The Super-Kamiokande Collaboration in 1998 [19], and SNO Collaboration in 2001 [20], have provided measurements of the neutrino flux from solar and atmospheric sources. The Nobel Prize in Physics 2015 was awarded jointly to Takaaki Kajita and Arthur B. McDonald “for the discovery of neutrino oscillations, which shows that neutrinos have mass” [21]. Such feature contradicts the description of the neutrinos in the SM, which are assumed to be massless, therefore there needs to be a mechanism that generates neutrino masses. One possibility would be to add Majorana mass terms or adding additional right-handed neutrinos with a very heavy mass, known as the see-saw mechanism [22].

Dark Matter

Although Dark Matter (DM) has never been directly observed, its existence is inferred from its gravitational effects. For example, looking at galaxies rotation, it was observed that the rotation speed was higher than expected, given the amount of visible matter [23]. Two different reasoning arose during the last century to justify such effect: there is either matter that cannot be seen by us (in terms of visible light), which contributes to the galactic mass, or the general relativity works differently at galactic distances. The former is believed to be the most likely and it implies the existence of new particles which do not interact via electromagnetic interaction, the so-called Weakly Interacting Massive Particle (WIMP) [24].

1.2 Supersymmetry and the MSSM

One of the main motivations for SUSY is the cancellation of quadratic divergences to Δm_H^2 via the introduction of the so-called SUSY particles with a half-integer spin difference with respect to their SM partners. This provides a solution to the hierarchy problem as the Higgs mass squared potential receives corrections from a new scalar of mass of the form:

$$\Delta m_H^2 = -\frac{|\lambda_S|^2}{16\pi^2} \left[\Lambda_{\text{UV}}^2 - 2m_S^2 \ln(\Lambda_{\text{UV}}/m_S) + \dots \right] \quad (1.14)$$

where, λ_S is the coupling of SUSY particles to the Higgs field. This term cancels the fermionic contributions in Eq. 1.13 since the couplings are the same, which means that the experimentally measured mass of the Higgs boson can be obtained without performing any unnatural *tuning* of the parameters [25, 26]. This is what makes SUSY a *natural* theory³.

The running of gauge coupling constants⁴ is predicted by the SM, but, as previously mentioned, although the electroweak unification occurs at ~ 100 GeV, it is not the case for the strong force. In the MSSM, a supersymmetric extension of the SM, due to addition of *new* particles involved in the gauge interactions, a new set of coefficients arise. As shown in Figure 1.5 the three lines, representing electromagnetic (dashed blue), weak (dashed red) and strong (solid green) interactions respectively, do not meet at one point, but they do with the introduction of supersymmetry. This can therefore be considered an approximate unification, of all three gauge couplings, at the Planck scale, which is an indication for a potential Grand Unification Theory (GUT) that could be obtained within a supersymmetric model. In addition, together with the unification at the GUT scale, another good motivation for SUSY searches is that, if SUSY is MSSM-like (m_{SUSY} not heavier than ~ 1 TeV), it can be discovered at the LHC.

SUSY introduces a space-time symmetry that relates bosons to fermions and vice-versa, via

³ The Naturalness of a theory is a property for which dimensionless ratios between free parameters should assume sensible values and that free parameters are not fine-tuned.

⁴ The coupling strength, as a function of energy, is calculable given a value at a fixed scale.

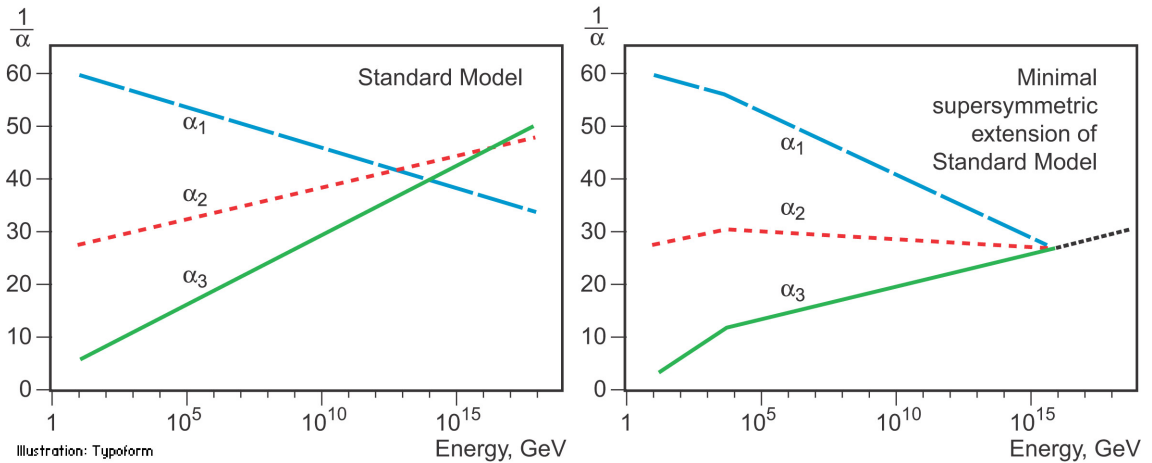


Figure 1.5: The inverse couplings of electromagnetic (dashed blue), weak (dashed red) and strong (solid green) interactions with the SM (left) and a supersymmetric model (right). In the SM the three lines do not meet at one point, but with the introduction of supersymmetry, and assuming that the supersymmetric particles are not heavier than about 1 TeV, they do meet.

a transformation of the form of:

$$Q |\text{fermion}\rangle = |\text{boson}\rangle, \quad Q |\text{boson}\rangle = |\text{fermion}\rangle \quad (1.15)$$

For each SM particle there exists a supersymmetric partner, generally called *sparticle* (where the s stands for “scalar”), with a spin difference of $\Delta s = 1/2$. Each pair of partners is arranged in a so-called *supermultiplet*. The two components have same masses and quantum numbers, but different spin, due to their relation to the Q operator (and its properties).

Sleptons and *squarks* interact as their SM equivalent. The superpartners of the left-handed fermion components couple weakly, while the superpartners of the right-handed SM fermion components do not. Gauge supermultiplets contain a vector boson and two spin- $\frac{1}{2}$ fermions. Spin-1 bosons are arranged in gauge multiplets, and their superpartners, referred to as *gauginos*, are spin- $\frac{1}{2}$ fermions. Unlike the SM, the Spin-0 Higgs boson has two supermultiplets containing sparticles with different weak isospin values, referred to as H_u and H_d , which are required to give mass to both the up- and down-type sparticles. Higgs SUSY partners are called the *Higgsinos*.

As of today, SUSY particles have not been observed, resulting in the assumption that SUSY must be a broken symmetry, otherwise superpartners would have the same masses as their SM equivalent. However, if sparticles were to be too heavy (close to the Planck scale), the hierarchy problem would be re-introduced and therefore would still remain unsolved. The *soft* SUSY breaking mechanism, described in Section 1.2.1, overcomes this problem by imposing constraints on the masses of sparticles to a range that can be experimentally explored.

1.2.1 Minimal Supersymmetric Standard Model

There does not exist a unique extension of a supersymmetric SM, i. e. SUSY is not a well-defined model but it is more a framework within which various SM extensions can be derived. The MSSM, a minimal supersymmetric extension of the SM [27], is defined by essentially doubling up the number of particles in the SM theory in order to include all the SM particles as well as their corresponding superpartners.

Soft SUSY breaking

The mass spectrum of the SUSY particles must sit somewhere at a larger scale than the SM one, as supersymmetric particles have not been discovered at the mass scale of their SM partners. This gives us a hint that supersymmetry cannot be an exact symmetry and therefore it is broken. There has to be an analogy with the electroweak symmetry breaking discussed in 1.1.1, where the symmetry is broken by a non-zero VEV. The mechanism must be spontaneous in order for the broken supersymmetry to still provide a solution to the hierarchy problem: a big alteration of the relationship between the fermionic and scalar couplings will result in a non-cancellation of the corrections to the Higgs mass squared parameter. This equates to adding terms to the SUSY Lagrangian which are gauge invariant and violate SUSY, but contain only masses and couplings with positive mass dimension. The total Lagrangian is defined as;

$$\mathcal{L}_{\text{MSSM}} = \mathcal{L}_{\text{SUSY}} + \mathcal{L}_{\text{soft}} \quad (1.16)$$

where all the additional terms are contained within $\mathcal{L}_{\text{soft}}$ and the original SUSY invariant interaction terms are contained within $\mathcal{L}_{\text{SUSY}}$. A new set of parameters is then introduced into this SM extension. These parameters determine the mixing between the flavour eigenstates and the SUSY phenomenology, which will be discussed in Section 1.2.2.

MSSM mass spectrum

As per the SM gauge bosons, the gaugino masses are affected by electroweak symmetry breaking. The new states, introduced in the $\mathcal{L}_{\text{soft}}$, mix to form the mass eigenstates of the sparticles. The neutral Winos (\tilde{W}^0), Binos (\tilde{B}^0), and Higgsinos (\tilde{H}^0) mix to form the four *neutralinos* $\tilde{\chi}_i^0$ ($i = 1, 2, 3, 4$) as it follows;

$$\begin{pmatrix} \tilde{\chi}_1^0 \\ \tilde{\chi}_2^0 \\ \tilde{\chi}_3^0 \\ \tilde{\chi}_4^0 \end{pmatrix} = \begin{pmatrix} M_1 & 0 & -c_\beta s_W m_Z & c_W s_\beta m_Z \\ 0 & M_2 & c_\beta c_W m_Z & -c_W s_\beta m_Z \\ -c_\beta s_W m_Z & c_\beta s_W m_Z & 0 & -\mu \\ s_\beta c_W m_Z & -s_\beta c_W m_Z & -\mu & 0 \end{pmatrix} \begin{pmatrix} \tilde{B}^0 \\ \tilde{W}^0 \\ \tilde{H}_u^0 \\ \tilde{H}_d^0 \end{pmatrix} \quad (1.17)$$

Here, $c_\beta = \cos \beta$, $(s_\beta) = \sin \beta$, $c_W = \cos \theta_W$ and $(s_W) = \sin \theta_W$. M_1 , M_2 are related to gaugino masses and μ to Higgsinos mass, $\tan \beta$ is the ratio of the VEVs of the two Higgs doublet fields,

θ_W is the ratio of the electroweak coupling constants and, m_Z (m_W) is the mass of the Z (W) boson. The neutralino indices are conventionally assumed to increase with their masses. The charged winos (\tilde{W}^\pm) and Higgsinos (\tilde{H}^\pm) mix to form four *charginos*, $\tilde{\chi}_i^\pm$ ($i = 1, 2$) as it follows;

$$\begin{pmatrix} \tilde{\chi}_1^\pm \\ \tilde{\chi}_2^\pm \end{pmatrix} = \begin{pmatrix} M_2 & \sqrt{2}m_W s_\beta \\ \sqrt{2}m_W c_\beta & \mu \end{pmatrix} \begin{pmatrix} \tilde{W}^\pm \\ \tilde{H}^\pm \end{pmatrix} \quad (1.18)$$

Charginos and neutralinos mix as described in Eq. 1.18 and 1.17 and will be referred to as bino-like, wino-like or higgsino-like depending on their phenomenology. Gluinos do not mix as they carry colour charge.

The Higgs sector is also affected. There are five mass eigenstates, h^0, H^0, A^0 , and H^\pm . These, together with the other MSSM particles are listed in Table 1.2.

Table 1.2: SUSY particles in the MSSM

Name	Spin	Gauge Eigenstates	Mass Eigenstates
Squarks (\tilde{q})	0	$\tilde{u}_L \tilde{u}_R \tilde{d}_L \tilde{d}_R$	(same)
		$\tilde{c}_L \tilde{c}_R \tilde{s}_L \tilde{s}_R$	(same)
		$\tilde{t}_L \tilde{t}_R \tilde{b}_L \tilde{b}_R$	$\tilde{t}_1 \tilde{t}_2 \tilde{b}_1 \tilde{b}_2$
Sleptons (\tilde{l})	0	$\tilde{e}_L \tilde{e}_R \tilde{\nu}_L$	(same)
		$\tilde{\mu}_L \tilde{\mu}_R \tilde{\nu}_L$	(same)
		$\tilde{\tau}_L \tilde{\tau}_R \tilde{\nu}_\tau$	$\tilde{\tau}_1 \tilde{\tau}_2 \tilde{\nu}_\tau$
Higgs bosons	0	$H_u^0 H_d^0 H_u^+ H_d^-$	$h^0 H^0 A^0 H^\pm$
Neutralinos ($\tilde{\chi}_j^0$)	1/2	$\tilde{B}^0 \tilde{W}^0 \tilde{H}_u^0 \tilde{H}_d^0$	$\tilde{\chi}_1^0 \tilde{\chi}_2^0 \tilde{\chi}_3^0 \tilde{\chi}_4^0$
Charginos ($\tilde{\chi}_i^\pm$)	1/2	$\tilde{W}^\pm \tilde{H}_u^+ \tilde{H}_u^-$	$\tilde{\chi}_1^\pm \tilde{\chi}_2^\pm$
Gluino	1/2	\tilde{g}	(same)
Gravitino	3/2	\tilde{G}	(same)

In the MSSM the squark sector is specified by the mass matrix in the basis $(\tilde{q}_L, \tilde{q}_R)$ with $\tilde{q} = \tilde{t}$ or \tilde{b} [28]. A rotation matrix can be defined also for left- and right-handed squarks and sleptons, although in the MSSM the mixing is assumed to be non-zero only for the third-generation scalar partners. Stop (\tilde{t}_L, \tilde{t}_R), sbottom (\tilde{b}_L, \tilde{b}_R), and stau ($\tilde{\tau}_L, \tilde{\tau}_R$) rotate into mass eigenstates, $\tilde{t}_1, \tilde{t}_2, \tilde{b}_1, \tilde{b}_2, \tilde{\tau}_1, \tilde{\tau}_2$, respectively, as described in Eq. 1.19 [29].

$$\mathcal{M}_{\tilde{q}}^2 = \begin{pmatrix} m_{\tilde{q}_L}^2 & a_q m_q \\ a_q m_q & m_{\tilde{q}_R}^2 \end{pmatrix} \quad (1.19)$$

with

$$\begin{aligned}
m_{\tilde{q}_L}^2 &= M_{\tilde{Q}}^2 + m_Z^2 \cos 2\beta \left(I_3^{q_L} - e_q \sin^2 \theta_W \right) + m_q^2, \\
m_{\tilde{q}_R}^2 &= M_{\{\tilde{U}, \tilde{D}\}}^2 + m_Z^2 \cos 2\beta e_q \sin^2 \theta_W + m_q^2, \\
a_q m_q &= \begin{cases} (A_t - \mu \cot \beta) m_t, & (\tilde{q} = \tilde{t}) \\ (A_b - \mu \tan \beta) m_t, & (\tilde{q} = \tilde{b}) \end{cases}
\end{aligned} \tag{1.20}$$

Here, $I_3^{q_L}$ is the third component of the weak isospin and e_q the electric charge of the quark q . $M_{\{\tilde{Q}, \tilde{U}, \tilde{D}\}}$ and $A_{t,b}$ are soft SUSY-breaking parameters, μ is the higgsino mass parameter, and $\tan \beta$, as previously mentioned, is the ratio of Higgs field VEVs. By using the matrix in Eq. 1.19 one gets the mass eigenstates

$$\tilde{q}_1 = \tilde{q}_L \cos \theta_{\tilde{q}} + \tilde{q}_R \sin \theta_{\tilde{q}} \tag{1.21}$$

$$\tilde{q}_2 = -\tilde{q}_L \sin \theta_{\tilde{q}} + \tilde{q}_R \cos \theta_{\tilde{q}} \tag{1.22}$$

with the mass eigenvalues $m_{\tilde{q}_1}$, $m_{\tilde{q}_2}$ ($m_{\tilde{q}_1} < m_{\tilde{q}_2}$) and the mixing angle $\theta_{\tilde{q}}$ ($-\pi/2 < \theta_{\tilde{q}} \leq \pi/2$).

1.2.2 Phenomenology of Supersymmetry

As previously mentioned, the introduction of SUSY particles overcomes the problem of an unnatural fine-tuning to the Higgs mass due to its quadratic corrections.

R-parity

The most general MSSM can contain operators that violate baryon and/or lepton number, thus allowing proton decays. The non-observation of proton decays forbids the existence of such terms. A possibility to avoid these operators is to introduce a new discrete symmetry named *R*-parity. The conserved quantum number is defined as;

$$P_R = (-1)^{3(B-L)+2s} \tag{1.23}$$

where B , L , and s are the baryon, lepton, and spin number, respectively.

The SM particles have $R = 1$ and SUSY partners have $R = -1$. When *R*-parity conservation is imposed on MSSM models, the mixing between particles and sparticles cannot occur, resulting in the number of SUSY particles to be even at every interaction vertex. Furthermore, all sparticles must be pair-produced and the Lightest Supersymmetric Particle (LSP) has to be stable and can be a good Dark Matter candidate.

Although SUSY searches in an *R*-parity violating (RPV) scenario have been extensively investigated by the particle-physics community, in this work only *R*-parity conserving (RPC) models, where the $\tilde{\chi}_1^0$ is assumed to be the LSP, were considered.

Phenomenological MSSM (pMSSM)

As mentioned in 1.2.1, once the SUSY soft breaking occurred, the unconstrained MSSM has more than 100 parameters in addition to the SM ones. This makes the SUSY searches, e. g. finding regions, in parameter space, that are consistent with the data, rather impractical. However, the number of free parameters can be reduced down to 19 if the following assumptions are made;

- no new source of CP-violation (CKM matrix is the only source)
- no Flavour Changing Neutral Currents (FCNC)
- masses of the first- and second-generation sfermions are identical (first- and second-generation universality)

The introduction of such parameters, summarised in Table 1.3, defines the so-called Phenomenological MSSM (pMSSM).

Table 1.3: Parameters in the pMSSM.

Parameter	Description	N. of parameters
M_1, M_2, M_3	Bino, Wino and gluino masses	3
M_A	pseudo-scalar Higgs boson mass	1
μ	higgsino mass	1
$m_{\tilde{q}}, m_{\tilde{u}_R}, m_{\tilde{d}_R}$, $m_{\tilde{Q}_L}, m_{\tilde{t}}, m_{\tilde{b}}$	first- and second-generation squark masses third generation squark masses	3 3
$m_{\tilde{l}}, m_{\tilde{e}_R}$ $m_{\tilde{L}}, m_{\tilde{\tau}_R}$	first- and second-generation slepton masses third-generation slepton masses	2 2
A_t, A_b, A_τ	third-generation trilinear couplings	3
$\tan \beta$	two-higgs-doublet fields VEVs ratio	1

Such parameter space is still rather large and it makes pMSSM searches extremely challenging and difficult to exclude. To overcome this problem *simplified models* are introduced. In other words, a certain signal process is extracted from the model and only particles contributing to a certain decay mode will be considered, e. g. $\tilde{t}_1 \rightarrow t + \tilde{\chi}_1^0$ only targets the 2-body decay ignoring the remaining SUSY mass spectrum. The number of parameters will then boil down to 2; $m_{\tilde{t}}$ and $m_{\tilde{\chi}^0}$, allowing the reinterpretation of the results and providing a powerful tool to constrain various models.

In this work only analyses based on such simplified models will be presented.

Phenomenology of the top squark

Figure 1.6 shows SUSY particles production cross-sections in pp collisions at $\sqrt{s} = 13$ TeV for squarks that do not contribute to gluino production diagrams and vice versa, i. e. treating squarks and gluinos as *decoupled* making the cross-section of squark pair-production be the same for all families. While gluino pair-production cross-sections are fairly large, SUSY electroweak production cross-sections of neutralinos and charginos are considerably lower. Slepton production cross-section, which is not displayed, would sit just below higgsino-like chargino/neutralino production cross-section.

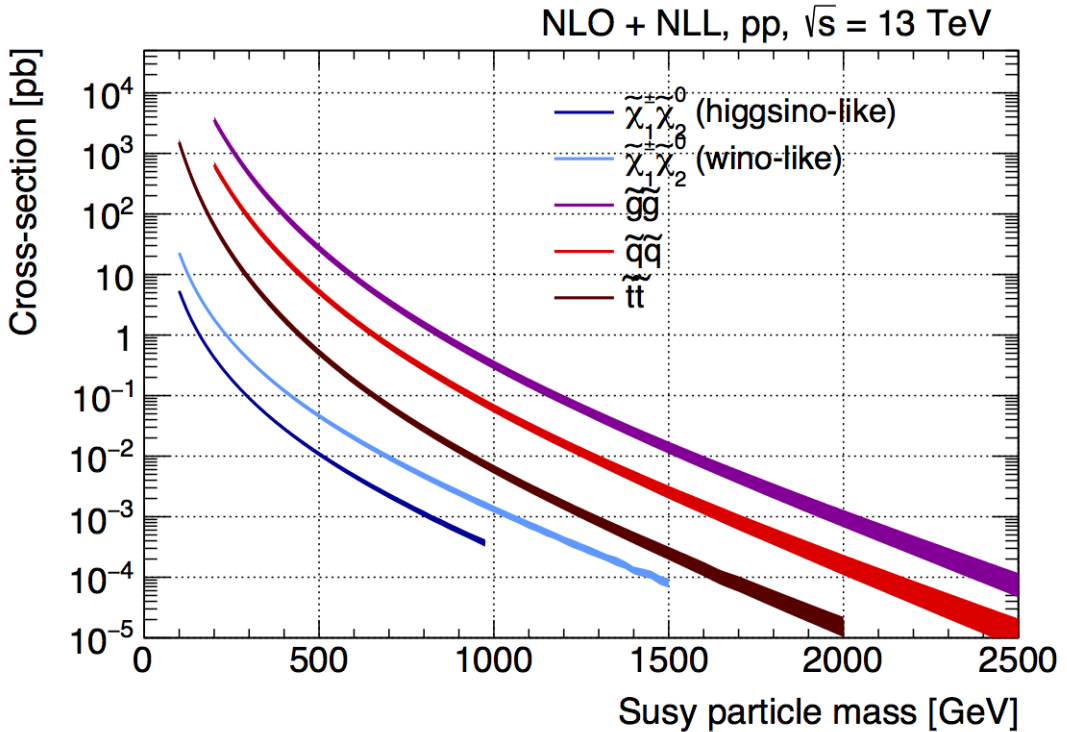


Figure 1.6: NLO+NLL production cross-sections as a function of mass at $\sqrt{s} = 13$ TeV [30]

There exists various decay modes of pair-produced stops, depending on the masses of the decay products;

- $\tilde{t} \rightarrow t \tilde{\chi}_1^0$
- $\tilde{t} \rightarrow b \tilde{\chi}_1^\pm \rightarrow b W \tilde{\chi}_1^0$ (on/off-shell W) or $\tilde{t} \rightarrow b W \tilde{\chi}_1^0$ (off-shell top)
- $\tilde{t} \rightarrow c \tilde{\chi}_1^0$
- $\tilde{t} \rightarrow b f f' \tilde{\chi}_1^0$

Figure 1.7 shows a schematic representation of the parameter space $(m_{\tilde{t}_1}, m_{\tilde{\chi}_1^0})$ and the different regions where each of the above-mentioned process dominates.

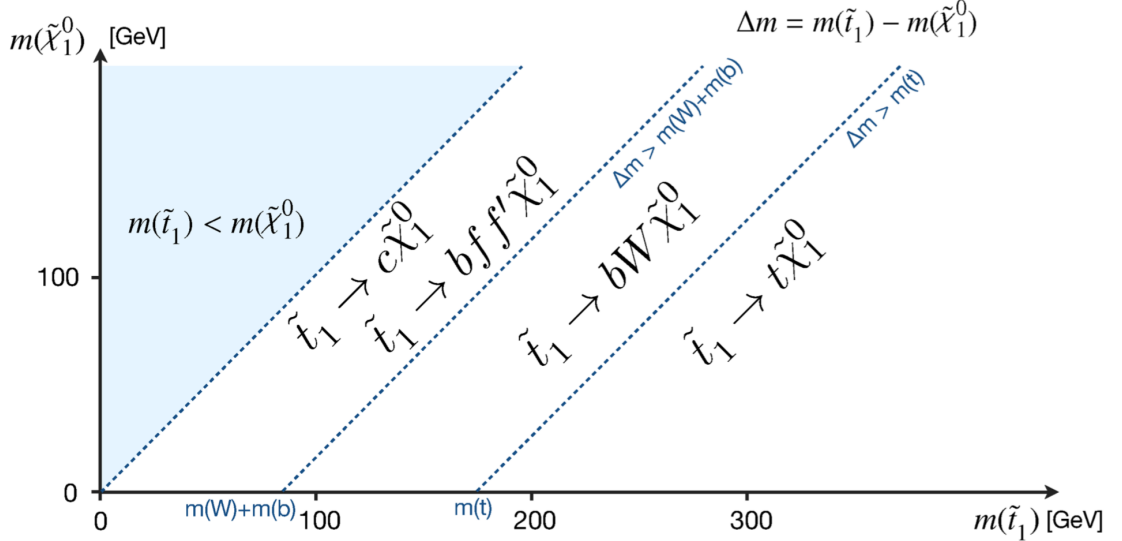


Figure 1.7: Illustration of stop decay modes in the $(m_{\tilde{t}_1}, m_{\tilde{\chi}_1^0})$ mass place where the $\tilde{\chi}_1^0$ is assumed to be the lightest supersymmetric particle. The dashed blue lines indicate thresholds separating regions where different processes dominate.

In the models considered in this work, either $\tilde{\chi}_2^0$ or $\tilde{\chi}_1^\pm$ is assumed to be the so-called Next Lightest Supersymmetric Particle (NLSP). Three different decay scenarios were considered in this work; (a) where both top squarks decay via $\tilde{t} \rightarrow t^{(*)} \tilde{\chi}_1^0$ ⁵; (b) at least one of the stops decays via $\tilde{t} \rightarrow b \tilde{\chi}_1^\pm \rightarrow b W^{(*)} \tilde{\chi}_1^0$; (c) where $m_{\tilde{\chi}_2^0}$ is small enough to allow one stop to decay via $\tilde{t} \rightarrow t \tilde{\chi}_2^0 \rightarrow h/Z \tilde{\chi}_1^0$. Here, h is the SM Higgs boson (125 GeV), as illustrated in Figure 1.8(a)–(c), respectively. Furthermore, top squarks can also be indirectly produced through the so-called gluino-mediated stop production, as shown in Figure 1.8(d).

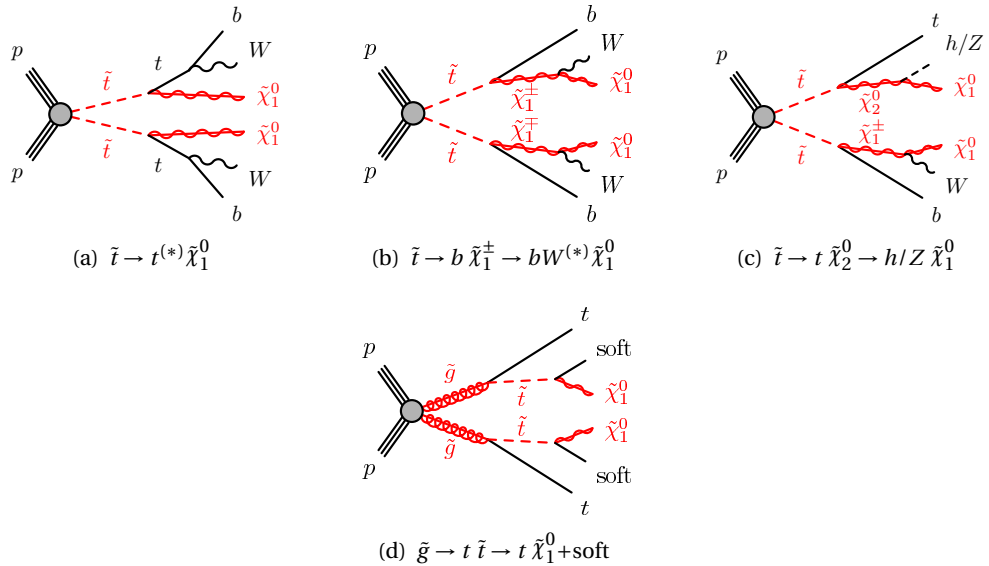


Figure 1.8: Diagrams of the decay topologies of the signal models considered in this work. The term “soft” refers to decay products that have transverse momenta below the detector thresholds.

⁵ The symbol (*) indicates the off-shell production

Third-generation SUSY analyses, e. g. stop pair-production ($\tilde{t}\tilde{t}$) or sbottom pair-production ($\tilde{b}\tilde{b}$) are very challenging, due to the cross-section being around a factor of six smaller than $t\bar{t}$ production (when $m_{\tilde{t}_1} \sim m_t$), which usually is one of the main backgrounds. Furthermore, the cross-section of such processes dramatically decreases with increasing $m_{\tilde{q}}$. Nonetheless, for example, searches for direct \tilde{t}_1 production with $\tilde{t}_1 \rightarrow t + \tilde{\chi}_1^0$ are sensitive in a scenario where $m_{\tilde{t}_1} \gg m_t + m_{\tilde{\chi}_1^0}$ as the large E_T^{miss} , from the neutralinos, provides discriminating power for $t\bar{t}$ rejection. Further details will be discussed in Chapter 5.

THE ATLAS EXPERIMENT AT THE LHC

2

We are rather like children, who must take a watch to pieces to see how it works.

Sir Ernest Rutherford

ATLAS (A Toroidal LHC ApparatuS) is one of the four main experiments¹ taking data at a centre-of-mass energy of 13 TeV using beams delivered by the LHC. In this chapter an overview of the LHC will be given in Section 2.1, then the ATLAS detector will be described in Section 2.2, and finally the Trigger system, used to cleverly select the data, will be described in Section 2.3. A more in-depth description of the Trigger algorithms the author has been involved in will be given in Chapter 3.

2.1 The LHC

As of today, the LHC [31] is the world's largest and most powerful particle accelerator. It was designed to help answer some of the fundamental open questions in particle physics by colliding protons at an unprecedented energy and luminosity. It is located at CERN, in the Geneva area, at a depth ranging from 50 to 175 metres underground. It consists of a 27-kilometre ring made of superconducting magnets, and inside it two high-energy particle beams travel in opposite directions and in separate beam pipes.

The beams are guided around the ring by a strong magnetic field generated by coils - made of special electric cables - that can operate in a superconducting regime. A total of 1232 superconducting dipole and 392 quadrupole magnets, with an average magnetic field of 8.3 T, are employed and kept at a temperature below 1.7 K, in order to preserve their superconducting properties. The former are used to bend the beams and the latter to keep them focused while they get accelerated.

¹ ATLAS, Compact Muon Solenoid (CMS), A Large Ion Collider Experiment (ALICE), Large Hadron Collider beauty (LHCb)

The collider first went live on September 2008 even though, due to a magnet quench incident that damaged over 50 superconducting magnets, it has been fully operational since November 2009 when low-energy beams circulated in the tunnel for the first time since the incident. This also marked the start of the main research programme and the beginning of the so-called Run 1: first operational run (2009 - 2013).

Performance of the LHC

In June 2015 the LHC restarted delivering physics data, after a two-year upgrade programme, the so-called Long Shut down 1 (LS1), during which the magnets were upgraded to handle the current required to circulate 7-TeV beams. It was the beginning of the so-called Run 2 - second operational run (2015-2018) - during which the LHC has collided up to 10^{11} bunches of protons every 25 ns at the design luminosity² of $2 \cdot 10^{34} \text{ cm}^{-2} \text{ s}^{-1}$. The definition of the luminosity is:

$$\mathcal{L} = f \frac{n_b N_1 N_2}{4\pi \sigma_x \sigma_y} \quad (2.1)$$

where N_1 and N_2 are the number of protons per bunch in each of the colliding beams, f is the revolution frequency of the bunch collisions, n_b the number of proton per bunch, and σ_x and σ_y are the horizontal and vertical dimensions of the beam. The luminosity is strictly related to the number of collisions occurring during a certain experiment via the following:

$$\mathcal{N}_{\text{event}} = \mathcal{L} \sigma_{\text{event}} \quad (2.2)$$

where σ_{event} is the cross section of the process under investigation. It has not only collided protons but also heavy ions, in particular lead nuclei at $\sqrt{s_{NN}} = 5.02 \text{ TeV}$, at a luminosity of $10^{27} \text{ cm}^{-2} \text{ s}^{-1}$ [32].

Acceleration stages

Before reaching the maximum energy, the proton beams are accelerated by smaller accelerators through various stages. Figure 2.1 shows a sketch of the CERN's accelerator complex. It all begins with the Linear Accelerator 2 (LINAC2). Here protons are accelerated up to 50 MeV, and then injected in the Proton Synchrotron Booster (PSB) where they reach 1.4 GeV. The next stage is the Proton Synchrotron, which boosts the beams up to 25 GeV and then Super Proton Synchrotron (SPS) makes them reach energies up to 450 GeV. Eventually, the beams are injected in bunches with a 25 ns spacing into the LHC, where they travel in opposite directions, while they are accelerated to up to a centre-of-mass energy of 13 TeV. Once the bunches reach the maximum energy, they are made collide at four different points, inside four experiments around the ring [31].

² the highest luminosity the detector was designed to cope with

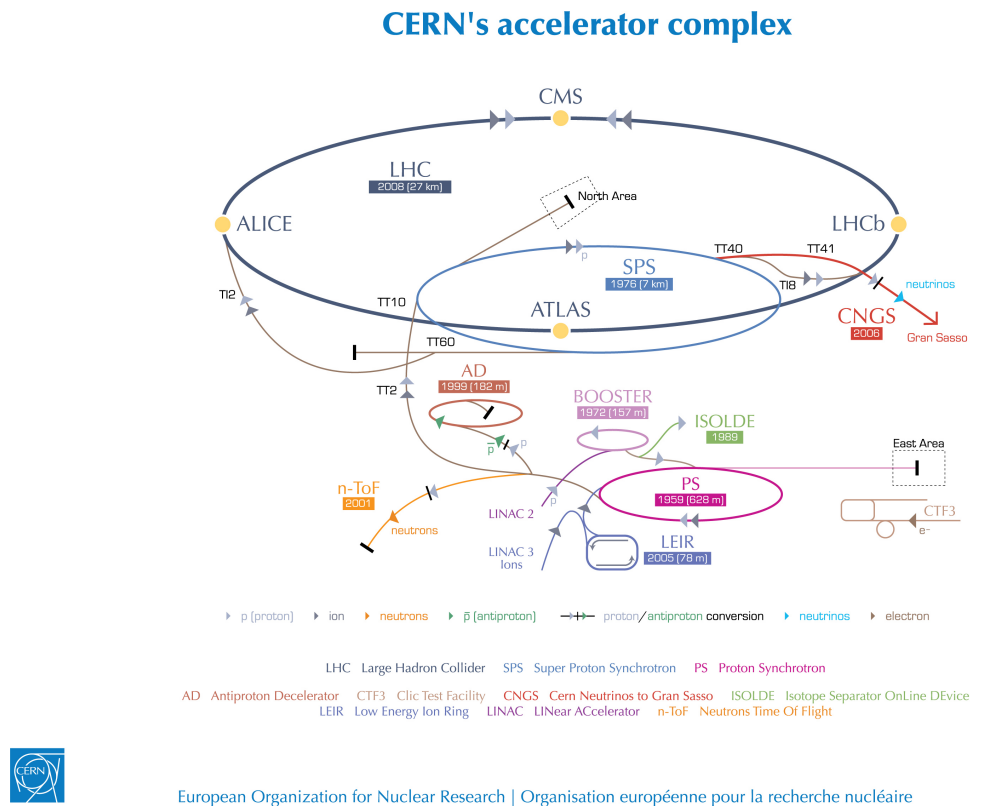


Figure 2.1: CERN Accelerator complex. The LHC is the last ring (dark grey line). Smaller machines are used for early-stage acceleration and also to provide beams for other experiments [33].

The heavy ion beams acceleration procedure is slightly different. Their journey starts at Linear Accelerator 3 (LINAC3), and the Low Energy Ion Ring (LEIR) then, before they make their way into the Proton Synchrotron where they follow the same path as the protons.

The four large detectors on the collision points are; the multi-purpose detectors ATLAS [34], and CMS [35], LHCb [36], which focuses on flavour physics, and ALICE [37] which specialises in heavy ion physics. The *big four* are not the only experiments at the CERN's accelerator complex. There also are smaller experiments based at the the four caverns about the collision points e.g. TOTal cross section, Elastic scattering and diffraction dissociation Measurement at the LHC (TOTEM) [38], Large Hadron Collider forward (LHCf) [39] and Monopole & Exotics Detector At the LHC (MoEDAL) [40], but these will not be discussed any further.

2.2 The ATLAS Detector

ATLAS is a general-purpose detector designed to collect data with the highest luminosity provided by the LHC. It is located at CERN's Point 1 cavern and it measures about 45 m in length and 25 m in diameter. It has a forward-backward symmetric cylindrical geometry with respect to the interaction point and it is designed to reconstruct and measure physics objects such as electrons, muons, photons and hadronic jets. Its design was optimised to be as sensitive as possible to the discovery of the Higgs boson and Beyond Standard Model (BSM) physics. In fact, thanks

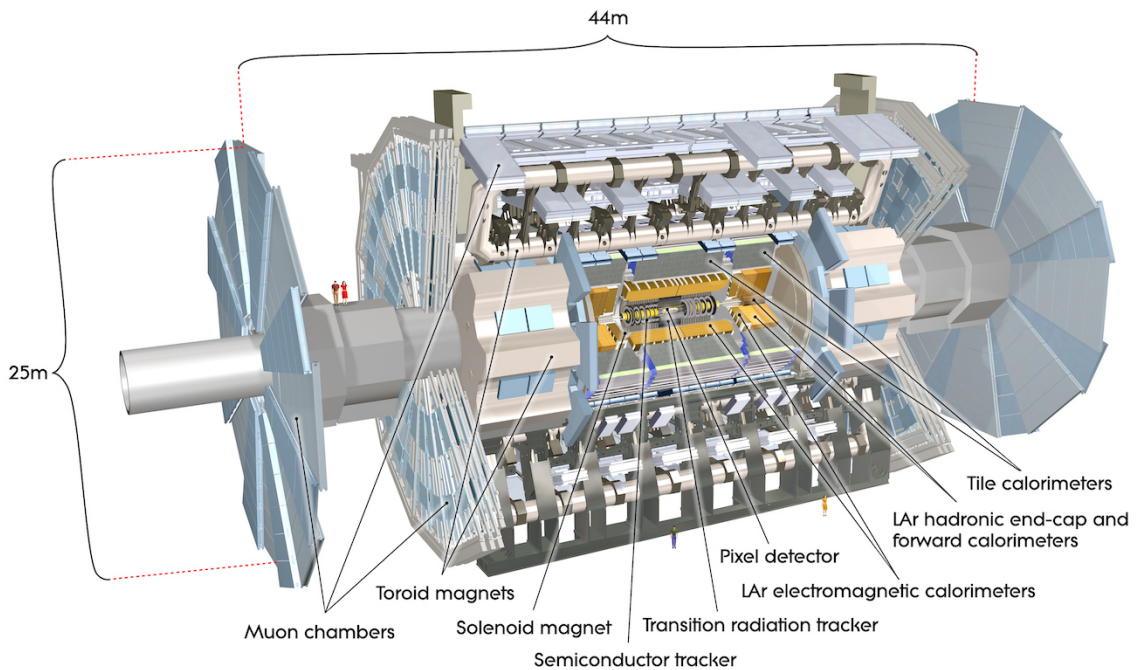


Figure 2.2: Cut-away view of the ATLAS detector. The dimensions of the detector are 25 m in height and 44 m in length. The overall weight of the detector is approximately 7000 tonnes [33].

to its various sub-systems, ATLAS is able to observe all possible decay products by covering nearly 4π steradians of solid angle.

In Figure 2.2 a cut-away view of ATLAS with all its components is shown. The innermost layer is the Inner Detector (ID) which is the core of the tracking system and consists of a Pixel, a SemiConductor Tracker (SCT), and a Transition Radiation Tracker (TRT). It is submerged in a 2 T magnetic field, generated by a thin superconducting solenoid, which bends all the charged particles' trajectories allowing transverse momentum measurement. The electromagnetic and hadronic calorimeters form the next layer and they are both used to perform precise energy measurements of photons, electrons, and hadronic jets. Finally, the outermost layer corresponds to the Muon Spectrometer (MS), enclosed in a toroidal magnetic field, which, together with the ID, allows precise measurement of momentum and position of muons. These sub-detectors will be discussed in more detail in the following sections.

The ATLAS coordinate system

A coordinate system is taken on for the spatial definition of the sub-systems and kinematic measurement of physics processes. Such system is defined starting from the interaction point, defined as the origin. The z -axis is defined by the beam direction and the $x - y$ plane, as transverse to the beam direction.

A quantity, known as pseudo-rapidity, (η), is defined to describe the angle of a particle coming out of the collision, with respect to the beam axis:

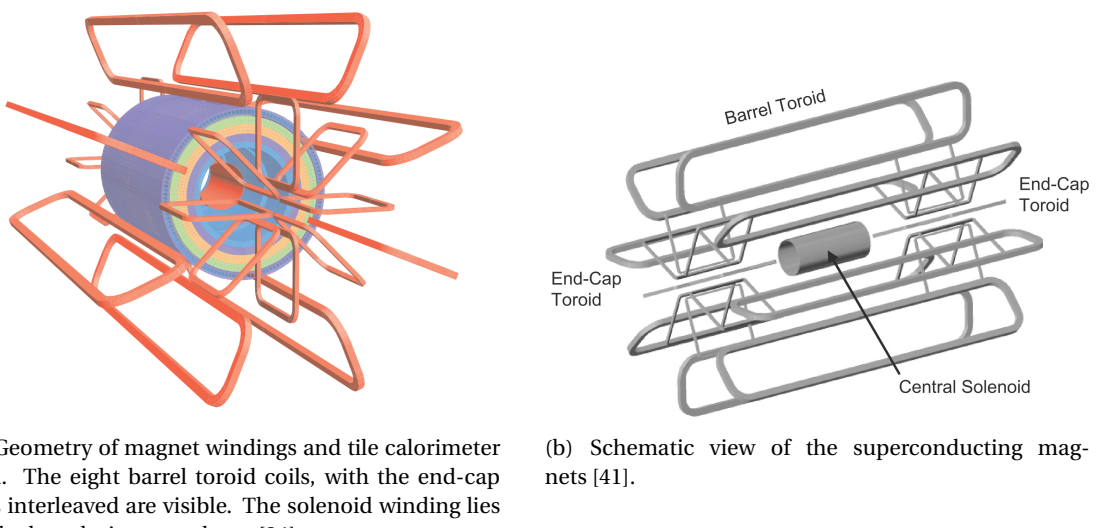
$$\eta \equiv -\ln(\tan(\theta/2))$$

Here θ is the polar angle. The azimuthal angle, ϕ , is defined around the beam axis and the polar angle. In the (η, ϕ) space a distance ΔR can be therefore defined as

$$\Delta R = \sqrt{\Delta\eta^2 + \Delta\phi^2}$$

where $\Delta\eta$ and $\Delta\phi$ are the differences in pseudo-rapidity and azimuthal angle between any two considered objects. A central and a forward region of pseudo-rapidity are also defined such that the detector components are described as part of the *barrel* if they belong to the former or as part of the *end-caps* if they belong to the latter.

2.2.1 The Magnet System



(a) Geometry of magnet windings and tile calorimeter steel. The eight barrel toroid coils, with the end-cap coils interleaved are visible. The solenoid winding lies inside the calorimeter volume [34].

(b) Schematic view of the superconducting magnets [41].

Figure 2.3: The ATLAS magnet system.

The ATLAS magnet system, 26 m long with a 22 m diameter, generates the magnetic field needed to bend the trajectories of charged particles in order to perform momentum measurement. Figure 2.3(a) and 2.3(b) show the geometry of the system and its components, which are made of NbTi - superconducting material - and will be described in the following paragraphs.

The Central Solenoid

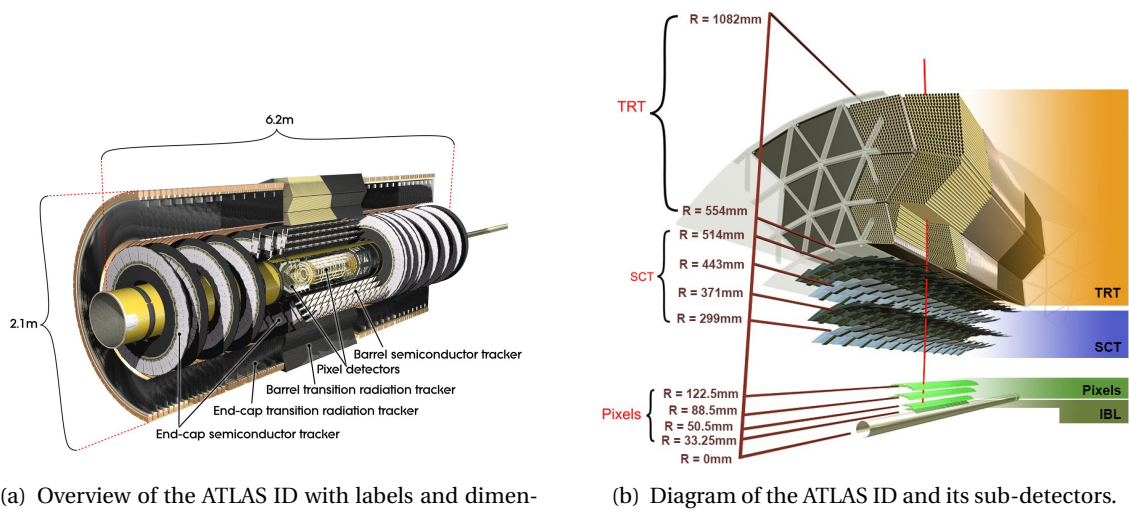
With an axial length of 5.8 m, an inner radius of 2.46 m, and an outer radius of 2.56 m, the central solenoid magnet is located between the ID and the Electromagnetic Calorimeter (ECAL). Its function is to bend the charged particles that go through the ID and it is aligned on the beam axis providing a 2 T axial magnetic field that allows accurate momentum measurement up to 100 GeV [41].

The Barrel and the End-cap Toroids

Figure 2.3(b) displays the toroid magnetic system that surrounds the calorimeters. With its cylindrical shape this component consists of a barrel and two end-caps toroids. The barrel toroid is comprised of eight coils and produces an approximately 0.5 T toroidal magnetic field for the central muon detectors. The end-cap toroids, also comprised of eight coils each, produce an approximately 1 T toroidal magnetic field, which is required to provide bending power for the end-cap regions of the muon spectrometer.

2.2.2 The Inner Detector

The ID [42] is the innermost component of the ATLAS detector i. e. the nearest sub-detector to the interaction region and it is used to reconstruct charged particle tracks used in the selection of physics objects. In fact, it allows robust track reconstruction, with accurate impact parameter resolution ($\sim 20\mu m$) and precise primary and Secondary Vertex (SV) reconstruction for charged particles (tracks) above 500 MeV and within $|\eta| < 2.5$.



(a) Overview of the ATLAS ID with labels and dimensions.

(b) Diagram of the ATLAS ID and its sub-detectors.

Figure 2.4: The ATLAS Inner Detector

The ID is comprised of independent and concentric sub-systems, which are all shown in Figure 2.4:

Insertable B-Layer (IBL):

innermost Pixel Detector layer added during ATLAS Run 2 upgrade (2013/2014) to improve vertexing, by a factor ~ 1.4 , and impact parameter reconstruction, by a factor 2;

Silicon Pixel Tracker (Pixel):

made of silicon pixel layers and used mainly for reconstructing both the primary and secondary vertices in an event;

SCT:

comprised of silicon micro-strip layers; thanks to its resolution ($17 \times 580 \mu\text{m}$) it can accurately measure particle momenta;

TRT:

final layer comprised of various layers of gaseous straw tube elements surrounded by transition radiation material.

These sub-detectors will be discussed in the following sections.

IBL

The IBL [43] is the innermost Pixel Detector layer as shown in Figure 2.4(b). It is comprised of 6M channels and each pixel measures $50 \times 250 \mu\text{m}$. Its resolution is $8 \times 40 \mu\text{m}$. The addition of this new layer produced an improvement on the quality of the impact parameter reconstruction of tracks almost by a factor 2, and almost by a factor 1.4 on the resolution of the reconstructed Primary Vertex (PV), highly important e.g. for the tagging of bottom-quark-initiated jets (b -jets).

Pixel

The Pixel detector is comprised of 1750 identical sensorchip-hybrid modules, each covering an active area of $16.4 \times 60.8 \text{ mm}$. The total number of modules correspond to roughly 80 million semiconductor silicon pixels. The nominal pixel size is $50 \mu\text{m}$ in the ϕ direction and $400 \mu\text{m}$ in the barrel region, along the z -axis (beam axis) [44]. The reason why such a large amount of pixels is employed is justified by the need to cope with the high luminosity in ATLAS. The silicon pixel detector measures 48.4 cm in diameter and 6.2 m in length providing a pseudo-rapidity coverage of $|\eta| < 2.5$. Figure 2.4(b) shows the three concentric barrel layers placed at 50.5 mm, 88.5 mm and 122.5 mm respectively. Furthermore, the Pixel detector is made of six disk layers, three for each forward region, such that when a charged particle crosses the layers it will generate a signal at least in three space points. The fine granularity of such detector allows accurate measurement and precise vertex reconstruction, as it provides a more accurate position measurement as a large detection area is available. In particular, it has a resolution of $10 \times 115 \mu\text{m}$.

SCT

The SCT is made of 4088 modules of silicon micro-strip detectors arranged in four concentric barrel layers. It is mainly used for precise momentum reconstruction over a range $|\eta| < 2.5$ and it was designed for precision measurement of the position using four points (corresponding to eight silicon layers), obtained as track hits when crossing the layers. Figure 2.4(b) shows the structure of the SCT with its four concentric barrel layers with radii ranging from 299 mm

to 514 mm and two end-cap layers. Each module has an intrinsic resolution of 17 μm in the $R - \phi$ direction and 580 μm in the z direction. As the SCT is further away from the beam-pipe than the Pixel detector, it has to cope with reduced particle density. This allows for reduced granularity maintaining the same level of performance of the Pixel detector: SCT can use ~ 6.3 million read-out channels.

TRT

The last and outermost of the sub-systems in the ID is the TRT. It is a gaseous detector which consists of 4 mm diameter straw tubes wound from a multilayer film reinforced with carbon fibres and containing a 30 μm gold plated tungsten wire in the centre. The straw is filled with a gas mixture of 70% Xe, 27% CO₂ and 3% O₂ [45]. As shown in Figure 2.4(b), its section consists of three concentric layers with radii ranging from 554 mm to 1082 mm, each of which has 32 modules containing approximately 50,000 straws, 1.44 m in length, aligned parallel to the beam direction with independent read-out at both ends. The gas is ionised when a charged particle passes through it and electrons (ions) are collected at the anode (cathode). A current in the wire will be created and as the electric field in the tube is known, the distance from the wire can be calculated using the time that electrons take to drift to the wire. Furthermore, the TRT is capable of performing particle identification on the particles that pass through it by utilising the detection of transition radiation photons that are emitted when a highly relativistic charged particle crosses a boundary between two media with different dielectric constants. The separation between, e. g. electrons and charged pions is achieved by observing the amount of transition radiation produced, since this is dependent on how relativistic the charged particle is.

The TRT has an intrinsic resolution of 130 μm and, on average, 35 hits are observed within such sub-system when a charged particle passes through.

Performance of the ID

As previously mentioned, the tracking performed by the ID is indispensable to measure the properties of objects such as leptons and jets, as well as interaction vertices in a certain event and secondary vertices, which are used e. g. to identify bottom-quark-initiated jets(b -jets). Both jets and b -jets are expected in the final states that are being searched for in this thesis.

The overall performance of the ID depends on the three sub-systems and it can be shown in terms of momentum resolution:

$$\frac{\sigma_{p_T}}{p_T} = 1.6 \pm 0.1\% \oplus \frac{(53 \pm 2) \cdot 10^{-5}}{\text{GeV}} \times p_T \quad (2.3)$$

measured in [46] using cosmic muons before the addition of the IBL. Eq. 2.3 shows that the ID has a momentum resolution of $\sim 1.6\%$ at low momenta (~ 1 GeV) and of $\sim 50\%$ at 1 TeV.

2.2.3 The Calorimeters

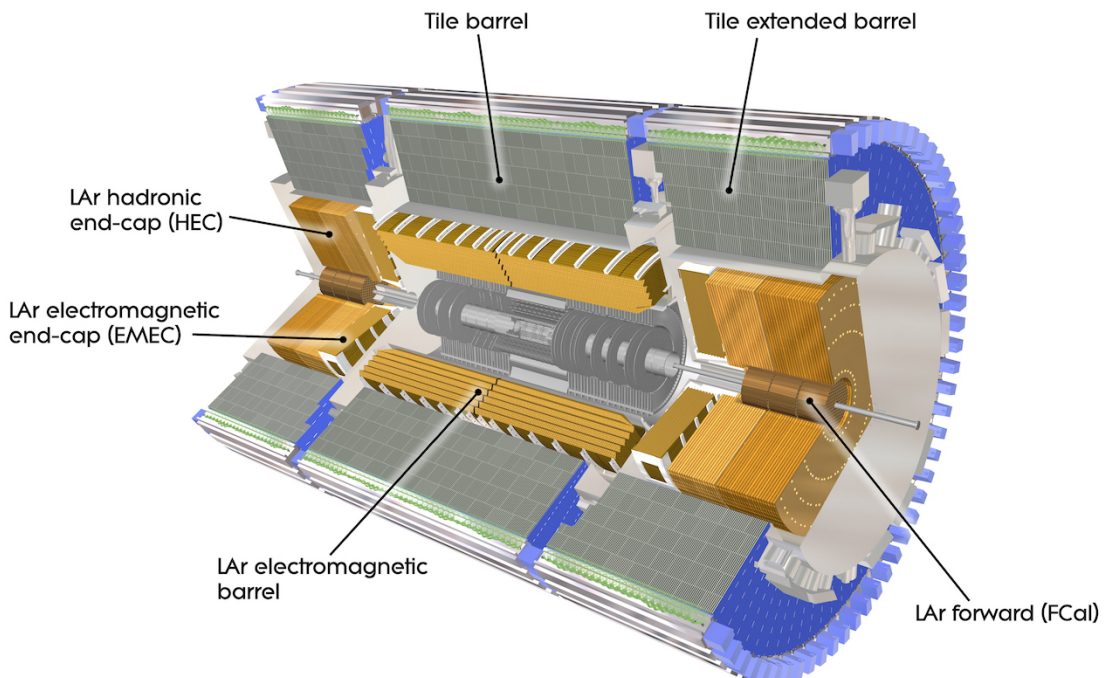


Figure 2.5: A computer generated image of the full calorimeter.

The ATLAS Calorimeter system, shown in Figure 2.5, is comprised of two main sub-systems; the ECAL and Hadronic Calorimeter (HCAL), which are designed to stop and measure the energy of electromagnetic-interacting and hadronic particles respectively. The combination of the two provides full coverage in ϕ and $|\eta| < 4.95$. Particles slow down and lose energy generating showers when crossing different layers. The ECAL is comprised of one barrel and two end-cap sectors employing Liquid Argon (LAr). The showers hereby develop as electrons pairs which are then collected. The HCAL is also comprised of one barrel and two end-cap sectors. The sensors in the barrel of the HCAL are tiles of scintillating plastic whereas LAr is employed for the end-cap. A forward region, the closest possible to the beam, is covered by a LAr forward calorimeter (FCal). The LAr and Tile Calorimeter will be briefly discussed in the following paragraphs.

The Liquid Argon Calorimeter

The ECAL is comprised of multiple layers of LAr sampler and lead absorber. The choice of its accordion-geometry design brought two main advantages; full ϕ coverage with no non-interactive regions (no cracks); fast extraction of signals coming from both front or rear end of the electrodes. It is made of two half-barrel wheels, both placed in the barrel cryostat, that provide a pseudo-rapidity coverage up to $|\eta| < 1.475$ and two end-cap detectors providing $1.375 \leq |\eta| \leq 3.20$ coverage in two end-cap cryostats. The junction between the barrel and

end cap components defines the crack region and any signal coming from the crack region is therefore discarded.

In the $|\eta| < 1.8$ region there is an additional layer, placed at the front of the calorimeter, that is made of a thin (0.5 cm in the end-cap and 1.1 cm in the barrel) LAr layer with no absorber [47]. This additional layer was designed to correct for the energy lost, as particles enter the calorimeter, by taking a measurement just before the majority of the electromagnetic shower is developed.

The Tile calorimeter

The main purpose of the hadronic calorimeter is to measure the energy of hadronic showers. It is built employing steel and scintillating tiles coupled to optical fibres which are read out by photo-multipliers. As shown in Figure 2.5, the HCAL is made up of three cylinders; a central barrel, 5.64 m long covering a region $|\eta| < 1.0$, and two extended barrel, 2.91 m long covering a region $0.8 < |\eta| < 1.7$. Each cylinder is made up of 64 modules and each module is in turn made up of three layers. Ultimately, the smallest section of the calorimeter module is a cell with a $\Delta\phi \times \Delta\eta = 0.1 \times 0.1$ granularity for the two innermost layers and $\Delta\phi \times \Delta\eta = 0.2 \times 0.1$ for the outermost one.

Performance of the Calorimeter

The performance of the calorimeter is important to measure the properties of the jets used in the analyses presented in this thesis. This has been assessed using test beam data and, once the noise has been subtracted from the experimental measurements these are fit using Eq. 2.4

$$\frac{\sigma(E)}{E} = \frac{a}{\sqrt{E[\text{GeV}]}} \oplus b \quad (2.4)$$

Here, a is the stochastic term and b is a constant that includes local non-uniformities in the calorimeter response.

The ECAL performance in the barrel was assessed firing an electron beam at a module that is identical to those in ATLAS and the fitted energy resolution is $\sigma(E)/E = (10 \pm 0.4)\%/\sqrt{E} \oplus (0.4 \pm 0.1)\%$ with a variation of no more than 0.7% for the entire coverage of the calorimeter.

The HCAL performance in the barrel was assessed firing a pion beam at a prototype detectors of the LAr electromagnetic and tile calorimeters. The fitted energy resolution (with an added term to account for electronic noise) is $\sigma(E)/E = (52 \pm 1.0)\%/\sqrt{E} \oplus (3.0 \pm 0.1)\% \oplus (1.6 \pm 0.1)/E$.

2.2.4 The Muon Spectrometer

The MS [48], shown in Figure 2.6, is the outermost sub-system of the whole ATLAS detector. As such, it surrounds the calorimeters and its main function is to perform precision measurement of muons momenta. The deflection of muon tracks employing large superconducting air-core

toroid magnets and high-precision tracking chambers is at the heart of such high precision measurement.

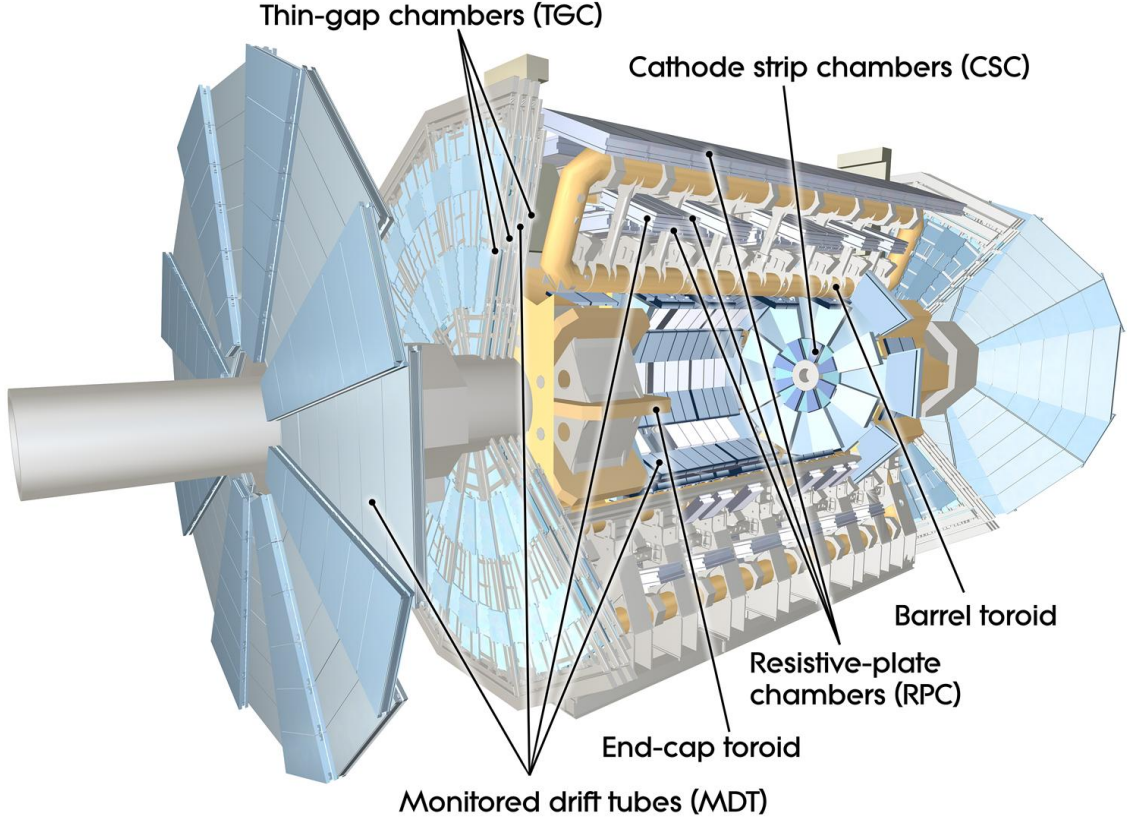


Figure 2.6: Cut-away view of the ATLAS muon system [34].

The MS is comprised of one large barrel toroid, covering the region $|\eta| \leq 1.4$, and two end-cap toroids, covering $1.6 < |\eta| \leq 2.7$ which are employed together to achieve the track-bending effect wanted. The magnitude of the magnetic field in the barrel, generated by eight large superconducting coils, ranges from 0.5 to 2 T.

Around the beam axis, three cylindrical layers make way for the chambers, placed in planes perpendicular to the beam, used to measure tracks.

Monitored Drift Tubes (MDTs) are employed over most of the pseudo-rapidity range to provide precision measurement of track coordinates in the bending direction. An MDT is essentially a set of 30-mm-diameter Aluminium tubes containing a *W-Re* (Tungsten-Rhenium) wire, surrounded by a non-flammable Ar-CH₄-N₂ mixture at a pressure of 3 bar. The resolution a single wire can give on the particle position is 80 μm enhanced by having multiple layers of tubes for each module.

Cathode Strip Chambers (CSCs) are instead employed at large pseudo-rapidity ($2 < |\eta| < 2.7$). They work similarly to the MDT but instead of tubes there are cathode strips above and below the anode wires. In particular, one set is orthogonal to the wires for precision measurement and the other one parallel to the wires providing a measurement of the transverse coordinate. The gas employed between the strips and wires is a non-flammable mixture of Ar-CO₂-CF₂.

Thin-Gap Chambers (TGCs) are employed in the end-cap region and Resistive-Plate Chambers (RPCs) in the barrel. The TGCs are very similar to the CSCs. They provide large signals and in a very narrow time window making them ideal for triggering purposes.

The RPCs are also gas-based detectors. They are comprised of two parallel resistive plates held apart by insulating spacers, and a uniform electric field is employed to generate a limited avalanche multiplication centred around the primary ionisation electron. This will then be detected by *Al* strips separated from the plates by an insulating film.

2.3 The ATLAS Trigger System

The ATLAS Trigger System is at the heart of data taking. It is an essential component of any nuclear or particle physics experiment as it is responsible for deciding whether or not to store an event for later study. Its main function to reduce the event rate from ~ 40 MHz bunch-crossing³ to ~ 1 kHz.

The Trigger system employs a two-level system: a first hardware-based trigger, Level-1 (L1) Trigger, and a software-based, High Level Trigger (HLT). L1 processes low-granularity information from the calorimeter and the muon spectrometer and identifies the so-called Regions of Interest (RoIs)⁴ before making a decision. Event data from other sub-system are temporarily stored in memories whilst L1 decision is taken.

Further investigations are left to HLT which is made of software running on a cluster of computers (HLT farm). Additionally, a Fast TracKer (FTK) system [49] (to be installed before the end of Run 2) will process events that are accepted by L1 trigger, and seed the HLT algorithms. It will provide global ID track reconstruction at the L1 trigger rate using lookup tables stored in custom associative memory chips for the pattern recognition.

The ATLAS trigger system will be further discussed in Chapter 3, however the Run-1-to-Run-2 upgrade of the ATLAS trigger will not be discussed any further.

³ The term bunch-crossing, $\langle\mu\rangle$, is hereby used when referring to a collision between two bunches of protons.

⁴ $\eta - \phi$ regions where event features have been found by the L1 selection process.

THE ATLAS TRIGGER SYSTEM

3

*Software is a great combination
between artistry and engineering.*

Bill Gates

The ATLAS trigger system together with its performance will be presented in this chapter. A brief introduction of the reason behind the need of a trigger system, together with its implementation in ATLAS, will be discussed in Section 3.1. The L1 trigger and HLT will be discussed in Sections 3.2 and 3.3, respectively. Finally, Section 3.3.2 will be dedicated to the performance of HLT for low- p_T single-lepton, missing transverse energy, E_T^{miss} - as the most relevant trigger for the analysis discussed in Chapter 5 -, and medium- and high- p_T b -jet triggers. This has been part of the *qualification task*¹ of the author and the results were published in a paper in the European Physics Journal [50].

3.1 Overview

More than 80 fb^{-1} of pp collisions were delivered in 2016 and 2017 by the LHC and, due to storage space limitations, it is not feasible to save all the information about the collision after every bunch crossing. The ATLAS Trigger System is indispensable to reduce the read-out rate to a sensible value without affecting the physics programme of ATLAS, e. g. discarding potentially interesting events. A multiple-level architecture is employed to allow the trigger enough time to identify interesting events, using both software- and hardware-based real-time algorithms.

Figure 3.1 shows the Trigger and Data Acquisition (TDAQ) system. This is comprised of both a hardware-based first-level trigger (L1) and a software-based HLT, as already mentioned in Section 2.3. The L1 trigger decision is formed by the Central Trigger Processor (CTP), which receives inputs from the L1 Calorimeter (L1Calo) and L1 Muon (L1Muon) triggers. Once the events pass the L1 selection, they are buffered in the Read-Out System (ROS) and processed by the HLT, which receives information on the Region of Interest (RoI) from L1 to be used for

¹ In order to become an ATLAS author every active ATLAS researcher should spend 50% of their time (in their first year), moving to 30% the year after.

track reconstruction in the trigger algorithms. An ROI is an extended wedge-shaped spatial region in the detector, consisting of a direction in $\eta - \phi$ originating from a z -position along the beam-line, extended along the beam-line by independent directions with respect to this z position, and extended about the ϕ direction with independent directions in pseudo-rapidity, at the maximum and minimum z positions along the beam-line.

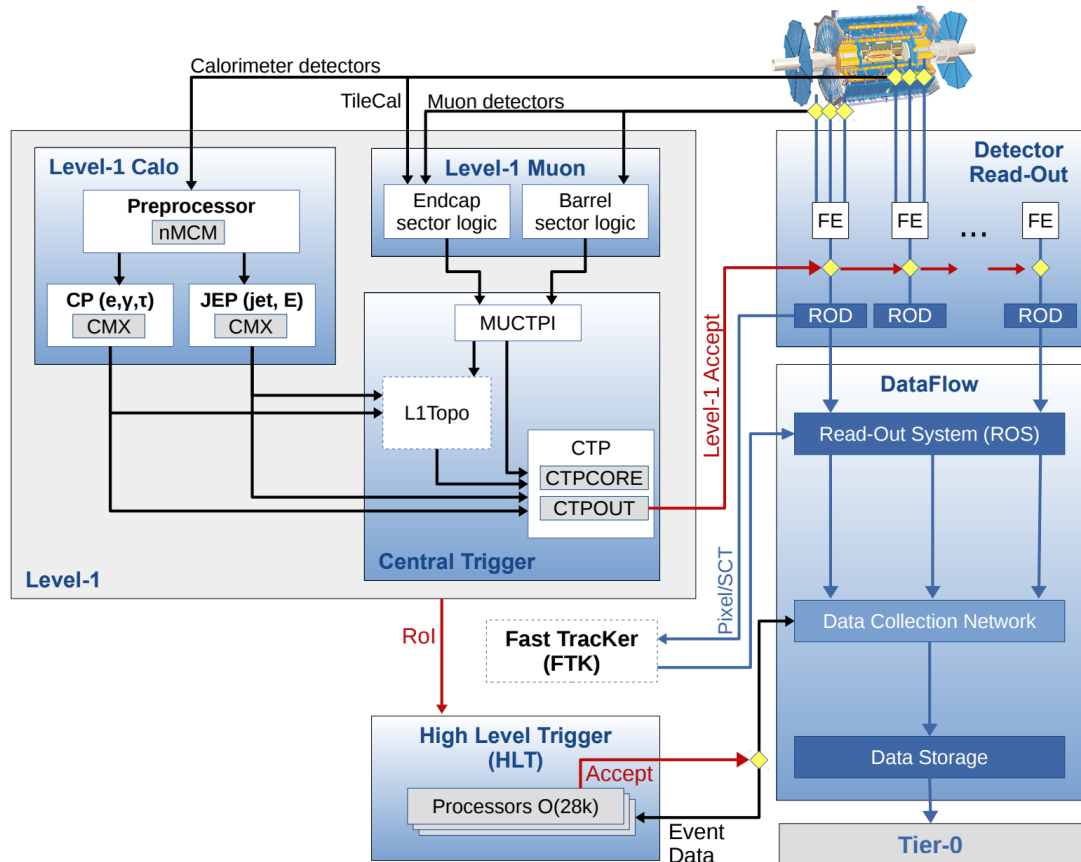


Figure 3.1: The ATLAS TDAQ system. L1Topo and FTK [50] have not been used for the results shown in this thesis.

The trigger system is configured via the so-called trigger *menu*, which contains the multiplicity requirement (number of tracks) and the pre-scale factors² for the selected events. Additionally, the menu is meant to define the trigger *chains* - usually referred to just as trigger - that start from a L1 trigger and specify a sequence of reconstruction and selection steps for the specific trigger signatures required in the trigger chain. This is named after the following convention:

TriggerLevel_TypeAndThreshold_Identification_Isolation

Here, “TriggerLevel” refers to either L1 or HLT, “TypeAndThreshold” refers to the type of object to trigger on (electron, muon, E_T^{miss} , etc.) and its energy threshold. If any identification and/or isolation criteria are included, these are appended at the end of the name, e.g.:

² A factor associated with a trigger at each level that indicates what fraction of events, that could pass this trigger selection, is actually accepted.

HLT_e24_1hmedium is an electron trigger with a 24 GeV threshold, using “medium” identification criteria, which will be further discussed in Chapter 4.

3.2 Level-1 Trigger

The L1 trigger decision is essentially taken by the CTP, based on the information the L1 calorimeter and L1 muon trigger systems. Additionally, a Level-1 Topological (L1Topo) trigger³, fed with energy and direction information about the objects found by the L1Calo and L1Muon triggers, is employed [34, 50, 51].

The L1 trigger system is implemented in fast custom electronics to keep the decision time around $2.5 \mu\text{s}$ and its decision is used as a *seed* for HLT.

The L1 Calorimeter Trigger

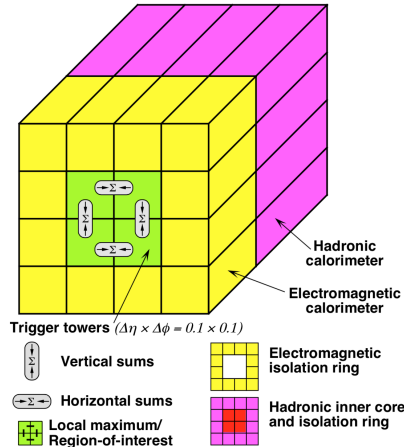


Figure 3.2: Illustration of the electron/photon and tau algorithms with the sums to be compared to programmable thresholds (from [52]).

The L1Calo trigger [34, 53] is based on inputs from the electromagnetic and hadronic calorimeters within the region $|\eta| < 4.9$. It provides triggers for objects such as electrons/photons, taus, jets, and global transverse energy. Dedicated analogue trigger signals, provided by the ATLAS calorimeters independently from the signals read out and used at the HLT and offline, make the L1Calo trigger decision, which is based on the information from analogue sums of calorimeter elements, called *trigger towers*, instead of using the full granularity of the calorimeter. The trigger towers have a size of approximately $\Delta\eta \times \Delta\phi = 0.1$ in the central part of the calorimeter, $|\eta| < 2.5$, and they get larger and less regular in the forward region. Separate trigger towers are employed for electromagnetic and hadronic calorimeters. Furthermore, two processor systems run the trigger algorithms, once the signals have been digitised: the first, called *cluster processor*, uses the full L1 trigger granularity information in the central region to look for small and localised clusters, which are typical a energy deposit left by an electron, photon or tau; the second, the *jet and energy-sum processor*, uses 2×2 sums of trigger towers (jet elements), to identify jet candidates and form missing transverse energy, $E_{\text{T}}^{\text{miss}}$, and total transverse energy, E_{T} . As an example, Figure 3.2 shows a sketch of the electron/photon and tau triggers. The trigger algorithm identifies a Region of Interest as a 2×2 trigger tower cluster in the electromagnetic calorimeter for which

larger and less regular in the forward region. Separate trigger towers are employed for electromagnetic and hadronic calorimeters. Furthermore, two processor systems run the trigger algorithms, once the signals have been digitised: the first, called *cluster processor*, uses the full L1 trigger granularity information in the central region to look for small and localised clusters, which are typical a energy deposit left by an electron, photon or tau; the second, the *jet and energy-sum processor*, uses 2×2 sums of trigger towers (jet elements), to identify jet candidates and form missing transverse energy, $E_{\text{T}}^{\text{miss}}$, and total transverse energy, E_{T} . As an example, Figure 3.2 shows a sketch of the electron/photon and tau triggers. The trigger algorithm identifies a Region of Interest as a 2×2 trigger tower cluster in the electromagnetic calorimeter for which

³ Two FPGA-based (Field-Programmable Gate Arrays) processor modules

the transverse-energy sum, released in at least one of the four possible pairs of nearest neighbour towers (1×2 or 2×1), exceeds a pre-defined threshold. Additionally, jets RoIs are defined as 4×4 , 6×6 or 8×8 trigger-tower windows for which the summed electromagnetic and hadronic transverse energy exceeds pre-defined thresholds and which surround a 2×2 trigger tower core that is a local maximum that will be also used to define the coordinates of the jet RoI.

The L1 Muon Trigger

The L1Muon trigger system [54] processes input data from fast muon trigger sub-detectors and its main task is to select muon candidates with a p_T threshold of 6 GeV and identify the bunch crossing in which they were produced.

Figure 3.3 shows how muons are triggered at L1. The RPC system in the barrel region ($|\eta| < 1.05$) and the TGC system in the end-cap regions ($1.05 < |\eta| < 2.4$) are employed. They provide a rough measurements of muon-candidate p_T , η , and ϕ . Three planes in the barrel and three in each endcap form the trigger chambers. Each plane is comprised of two to four layers and muon candidates are identified by forming coincidences between the muon planes. Coincidences are formed requiring hits that lie within parametrised geometrical muon *roads*. A road, as the example shown in Figure 3.3, essentially contains the trajectories, from the interaction point, of either positively or negatively charged muons with a p_T above a given threshold. In particular six programmable p_T thresholds are employed at L1, divided into two sets: three low- p_T thresholds meant to cover values up to 10 GeV, and three high- p_T thresholds meant to cover $p_T > 10$ GeV.

The CTP

The CTP [34] applies the multiplicity requirements and pre-scale factors specified in the trigger menu to the inputs from the L1 trigger systems and forms the L1 trigger decision. Timing and control signals⁴ are employed to distribute the L1 trigger decision to all ATLAS sub-detector readout systems. The CTP is responsible for applying the so-called *preventive dead-time*, meant to limit the minimum time between two consecutive L1 accepts (*simple dead-time*), $\mathcal{O}(100\text{ns})$, in order to both avoid overlapping readout windows, and restrict the number of L1 accepts allowed in a given number of bunch-crossings (*complex dead-time*) to avoid buffers from overflowing. In addition, a *busy dead-time*, can be introduced by ATLAS sub-detectors to temporarily throttle the trigger rate. These dead-times are used to monitor the total L1 trigger rate, and individual trigger rates that need to be monitored before and after any pre-scales and/or any vetoes that have been applied. Furthermore, such information is also used to provide a measure of the L1 dead-time, which has to be accounted for when determining the luminosity [52].

⁴ The timing signals are defined with respect to the LHC bunch crossings: a 25 ns time window centred on the instant at which a proton bunch might cross the ATLAS interaction point.

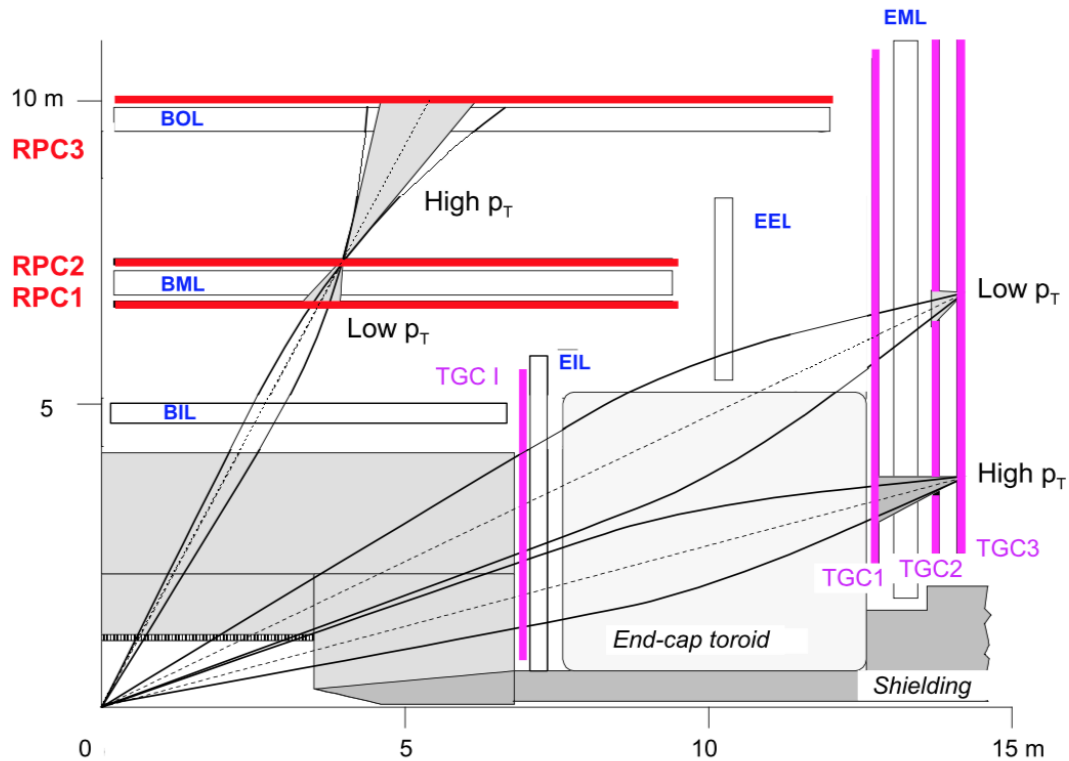


Figure 3.3: A schematic view of the L1Muon trigger chambers (from [52]).

3.3 High-Level Trigger

The events that are accepted by L1 are then buffered in the ROS and processed by the *High-Level Trigger* using information that is not available at L1, such as finer-granularity calorimeter inputs, precision measurements from the MS and tracking information from the ID. HLT receives RoI from L1 and performs the reconstruction within them. As needed, the reconstruction performed by the HLT software can either be run within RoIs or performing a so-called *full scan* of the detector. In order to reduce the processing time, a two-stage approach is employed for most HLT triggers: a first reconstruction (fast) to reject the majority of events; a second precision reconstruction for the remaining events (slower). Events that are accepted by the HLT get transferred to local storage at the experimental site and exported to the CERN’s computing centre for offline reconstruction [50].

3.3.1 Inner detector tracking

The track reconstruction in the Inner Detector is a vital component of the trigger decision in the HLT. A robust reconstruction of particle trajectories is an essential prerequisite for triggering on electrons, muons, taus, and b -jets. Furthermore, it is also used for triggering on inclusive pp interactions and for the on-line determination of the beam spot⁵ where the reconstructed

⁵ The luminous region produced by the collisions of proton beams.

tracks provide the input for vertex reconstruction.

The ID tracking in the trigger also includes information from the IBL, which significantly improves the tracking performance and in particular the impact parameter resolution [43]. The tracking algorithms are called *Fast Tracking* and *Precision Tracking*. The former is comprised of trigger-specific pattern recognition algorithms, unlike the latter which is heavily based on offline-tracking algorithms. As already mentioned, once an ROI has been identified by L1, the algorithms are typically configured to run within it. Furthermore, in order to reduce Central Processing Unit (CPU) usage, the offline track-finding is seeded with tracks and space-points identified by fast tracking stage seeds. The running of the full HLT reconstruction for each event on an individual node allows for the two stages of the trigger, e. g. b -jet triggers, which will be discussed in Section 3.3.2, to share the data preparation so detector information only needs to be read out once.

In order to reduce the detector volume of ROI, an advanced multi-stage approach, in particular for tau and b -jet tracking, is employed. The first stage is to identify leading tracks within an ROI, long in z but narrow in η and ϕ , by running the Fast Track Finder (FTF) algorithm. The leading tracks are used to construct a second-stage ROI, constrained in both η and ϕ , but very tightly constrained in polar angle and with a small z position width. The FTF is then run again within the wider second-stage ROI, followed by the Precision Tracking [50, 55]. The second stage, the Precision Tracking, is heavily based on an optimised subset of the tracking algorithms used offline, which is slower than the first but, in return, it identifies objects constructed starting from the inner detector tracks.

3.3.2 Performance of HLT

The performance of the tracking was estimated using 13-TeV pp collision events collected in July 2015 by the ATLAS detector (unless otherwise stated). In order to be as unbiased as possible, specific monitoring triggers that do not require a track to be present for the event to be accepted are used to estimate the efficiency of the tracking algorithms. All the quantities used to estimate the performance of the tracking, i. e. efficiencies, residuals and resolutions, are calculated with respect to the tracks found by the offline reconstruction software. In particular, the efficiency is defined as the fraction of offline reference tracks that are matched to a trigger track

$$\mathcal{E} = \frac{N_{\text{trigger}}}{N_{\text{offline}}} \quad (3.1)$$

The tracking efficiency has been estimated for electrons and muons for the single-stage tracking, and for b -jets for the multi-stage approach, as part of the author's qualification task. The reconstructed tracks are required to have at least two (six) Pixel (SCT) clusters and lie within the region $|\eta| < 2.5$. The closest trigger track within a cone of size $\Delta R = \Delta\eta^2 + \Delta\phi^2 = 0.05$ of the offline reconstructed track is selected as the matching trigger track.

Electrons

Figure 3.4 shows the tracking efficiency for the 24 GeV electron trigger as a function of η and p_T of the offline track. The tracking efficiency is measured with respect to offline tracks with $p_T > 20$ GeV for tight offline electron candidates from the 24 GeV electron support trigger, which does not use the trigger tracks in the selection, despite being identical to the physics trigger. The FTF and Precision Tracking efficiencies are all above 99% within the whole pseudo-rapidity range. The small efficiency drop at low p_T is due to bremsstrahlung energy loss by electrons [50].

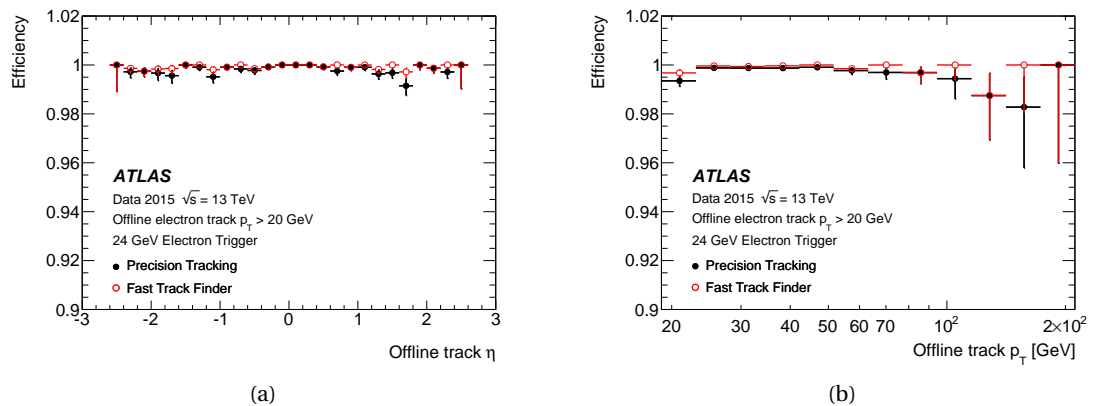


Figure 3.4: The ID tracking efficiency for the 24 GeV electron trigger is shown as a function of the (a) η and (b) p_T of the track of the offline electron candidate. Uncertainties based on Bayesian statistics are shown (from [50]).

Muons

Figure 3.5(a) shows the muon tracking performance with respect to offline muon candidates with $p_T > 6$ GeV selected by the 6 GeV muon support trigger as a function of the offline muon p_T . The efficiency is well above 99% in the entire p_T range for both FTF and Precision Tracking. Figure 3.5(b) shows the resolution of the transverse track impact parameter with respect to offline as a function of the offline muon p_T . FTF and Precision Tracking resolutions are better than 17 and 15 μm , respectively, for muon candidates with offline $p_T > 20$ GeV. The difference ($\sim 10\%$) between the two algorithms is driven by the fact that Precision Tracking (black solid points) uses the space points found by the FTF (red open points), but refits them using the offline algorithm. In other words, Precision Tracking runs a faster version of the full offline track fit and it performs better.

b-jets

As previously mentioned, the b -jet triggers tracking algorithms are run in a larger RoI than for electrons or muons and in order to limit CPU usage, multiple stage track reconstruction was implemented and deployed during Run-2.

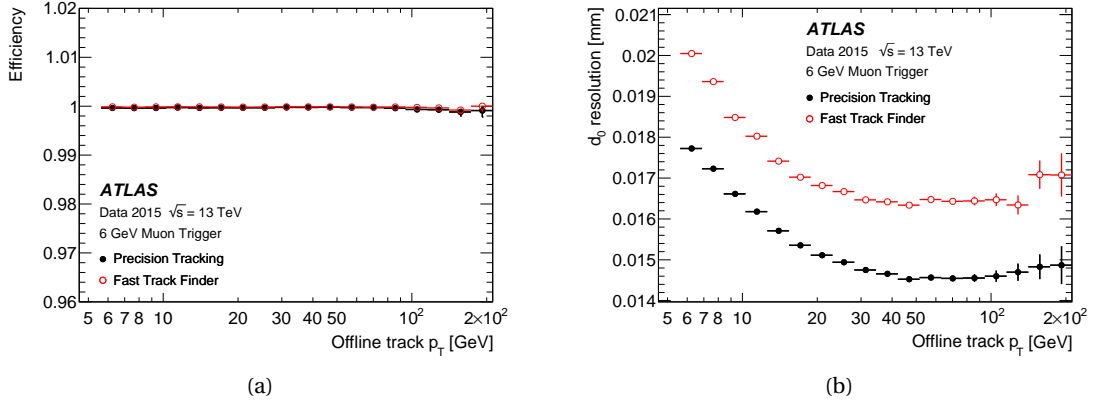


Figure 3.5: The ID tracking performance for the 6 GeV muon trigger; (a) efficiency as a function of the offline reconstructed muon p_T , (b) the resolution of the transverse impact parameter, d_0 as a function of the offline reconstructed muon p_T . Uncertainties based on Bayesian statistics are shown (from [50]).

First, the leading track and its position along the beam-line are determined by executing fast tracking in an ROI that is fully extended along the beam-line, in the $|z| < 225$ mm region, but narrow (0.1) in both η and ϕ , as shown in the blue-shaded region in Figure 3.6. The second stage is then run, using this position along the beam-line, to reconstruct all tracks in an ROI that is larger (0.4) in both η and ϕ but limited to $|\Delta z| < 10$ mm with respect to the leading track, as shown by the green-shaded region in Figure 3.6.

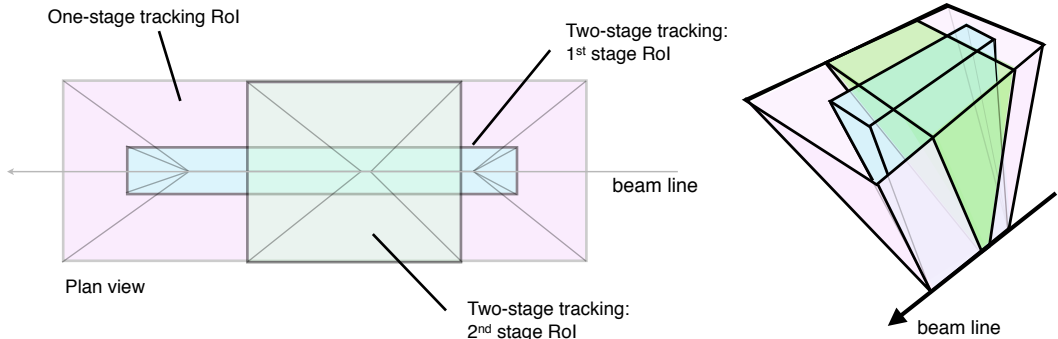


Figure 3.6: An illustration of the ROIs from the single-stage and two-stage tau lepton trigger tracking, shown in plan view (x-z plane) along the transverse direction and in perspective view. The z-axis is along the beam line. The combined tracking volume of the 1st and 2nd stage ROI in the two-stage tracking approach is significantly smaller than the ROI in the one-stage tracking scheme (from [50]).

The first-stage vertex tracking takes all jets identified by the jet trigger with $\eta > 30$ GeV and reconstructs tracks with the FTF in a narrow region in η and ϕ around the jet axis for each jet, but with $|z| < 225$ mm along the beam line.

Following this step, the primary vertex reconstruction [56] is performed using the tracks from the fast tracking stage. This vertex is used to define wider ROIs around the jet axes, with $|\Delta\eta| < 0.4$ and $|\Delta\phi| < 0.4$ but with $|\Delta z| < 20$ mm relative to the primary vertex z position. These ROIs are then used for the second-stage reconstruction that runs the fast track finder in the wider η and ϕ regions followed by the Precision Tracking, secondary vertexing and b -tagging

algorithms, which will not be discussed in this work.

The performance of the primary vertexing in the b -jet vertex tracking can be seen in Figure 3.7(a), which shows the vertex finding efficiency with respect to offline vertices in jet events with at least one jet with transverse energy above 55, 110, or 260 GeV and with no additional b -tagging requirement. The efficiency is shown as a function of the number of offline tracks with $p_T > 1$ GeV that lie within the boundary of the wider RoI (defined above) from the selected jets. The efficiency rises sharply and is above 90% for vertices with three or more tracks, and rises to more than 99.5% for vertices with five or more tracks. The resolution in z with respect to the offline z position as shown in Figure 3.7(b) is better than 100 μm for vertices with two or more offline tracks and improves to 60 μm for vertices with ten or more offline tracks.

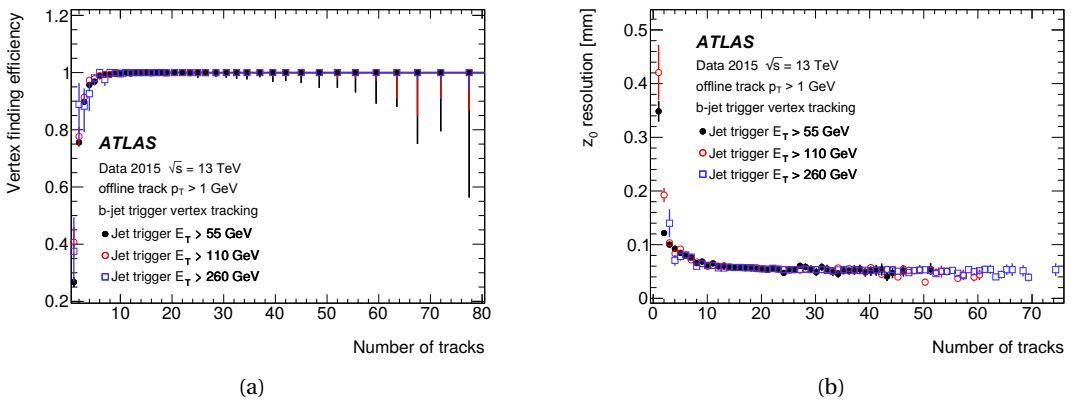


Figure 3.7: The trigger performance for primary vertices in the b -jet signatures for 55, 110 and 260 GeV jet triggers; (a) the vertexing efficiency as a function of the number of offline tracks within the jets used for the vertex tracking, (b) the resolution in z of the vertex with respect to the offline vertex position as a function of the number of offline tracks from the offline vertex (from [50]).

Missing Transverse Energy, E_T^{miss}

There exists several algorithms to reconstruct the E_T^{miss} at the HLT. The *missing H_T* ⁶ (MHT) algorithm calculates E_T^{miss} as the negative sum of transverse energy of calibrated jets, constructed from calibrated topological clusters of calorimeter cells. This algorithm is the most relevant to the analysis presented in Chapter 5. The *cell algorithm* is based on the negative sum of transverse energy deposited in calorimeter cells above a certain noise threshold. Unlike the cell algorithm, which calculates E_T^{miss} on the electromagnetic scale, the MHT algorithm looks at jets calibrated using jet energy scale, so that numerical threshold values for similar signal efficiencies differ. *Pufit*, a third algorithm, was employed to disentangle calorimeter deposits from the hard-scatter, from those originating from pile-up interactions by grouping towers made out of topological clusters into a pile-up and a hard-scatter category. This grouping is based on their energy, where the threshold itself is dependent on the overall event activity measured by the total energy deposited in the calorimeter. The assumption is that the contribution to E_T^{miss} due

⁶ H_T is the scalar sum of the various p_{T} s in the event, $H_T = \sum_i p_T^i$.

to pile-up interactions is zero. Nevertheless a minimisation, which takes into account resolution terms, determines an effective energy density from pile-up interaction which allows a vanishing contribution to E_T^{miss} by the pile-up calorimeter towers. This correction is then subtracted from the hard-scatter towers. The negative sum of transverse energy of those pile-up corrected hard-scatter towers will provide the final E_T^{miss} value [57].

Figure 3.8 shows the turn-on curves for various E_T^{miss} triggers: Figure 3.8(a) shows the efficiency as a function of *modified*⁷ offline E_T^{miss} for three different E_T^{miss} trigger algorithms, using early 2016 pp collision data. The events have been selected using single lepton (electron or muon) triggers. The x-axis shows the offline E_T^{miss} calculated from the sum of electrons, photons and jets, without the contributions from the muons. Three different E_T^{miss} high-level trigger algorithms are shown: HLT_xe80_tc_1cw_L1XE50 calculates E_T^{miss} based on calibrated clusters of calorimeter cells, and has a threshold of 80 GeV. HLT_xe90_mht_L1XE50 calculates E_T^{miss} based on reconstructed jets, and it has a threshold of 90 GeV. HLT_xe100_L1XE50 calculates E_T^{miss} based on calorimeter cells calibrated at the electromagnetic scale, and has a threshold of 100 GeV. All three algorithms are seeded by a Level-1 trigger with a threshold of 50 GeV which is also shown; Figure 3.8(b) shows the combined L1 and HLT efficiency of the missing transverse energy triggers HLT_xe110_pufit_L1XE50 and HLT_xe110_mht_L1XE50 as well as the efficiency of the corresponding L1 trigger (L1_XE50) are shown as a function of the reconstructed E_T^{miss} (modified to count muons as invisible) using pp collision data collected in 2017. The events shown are taken from data with a $W \rightarrow \ell\nu$ selection to provide a sample enriched in real E_T^{miss} . The HLT E_T^{miss} of the *pufit* algorithm is calculated as the negative of the transverse momentum vector sum of all calorimeter topological clusters corrected for pile-up. The pile-up correction is done by grouping the clusters into coarser “towers” which are then marked as pile-up if their E_T falls below a pile-up-dependent threshold.

⁷ To calculate the E_T^{miss} efficiency, e.g. in events with muons, a muon trigger must be employed, therefore muon contributions are removed.

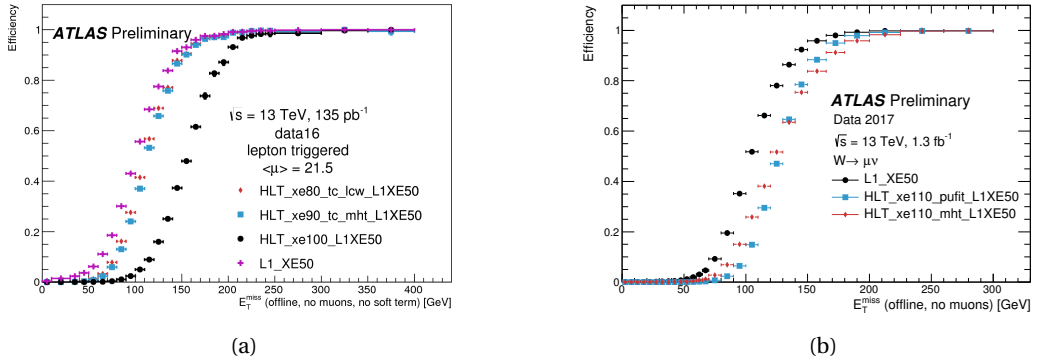


Figure 3.8: Turn-on curves of various E_T^{miss} triggers: Figure 3.8(a) shows the efficiency as a function of offline E_T^{miss} for three different E_T^{miss} high-level trigger algorithms. Three different E_T^{miss} trigger algorithms are shown: HLT_xe80_tc_lcw_L1XE50 calculates E_T^{miss} based on calibrated clusters of calorimeter cells, and has a nominal threshold of 80 GeV. HLT_xe90_mht_L1XE50 calculates E_T^{miss} based on reconstructed jets, and has a nominal threshold of 90 GeV. HLT_xe100_L1XE50 calculates E_T^{miss} based on calorimeter cells calibrated at the electromagnetic scale, and has a nominal threshold (at the electromagnetic scale) of 100 GeV. All three algorithms are seeded by a Level-1 trigger algorithm with a nominal threshold of 50 GeV which is also shown; Figure 3.8(b) shows missing transverse energy trigger efficiencies for HLT_xe110_pufit_L1XE50 and HLT_xe110_mht_L1XE50 and for the corresponding L1 seed (L1_XE50). (from [58]).

EVENT SIMULATION AND OBJECT RECONSTRUCTION

4

Nature isn't classical, dammit, and if you want to make a simulation of nature, you'd better make it quantum mechanical, and by golly it's a wonderful problem, because it doesn't look so easy.

Richard P. Feynman

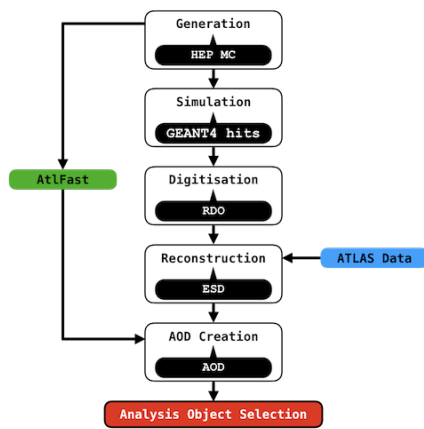


Figure 4.1: The different stages of the work flow needed to produce analysable simulated and real data outputs. The white boxes represent the processes, and their outputs are shown in black balloons: RD0, ESD, and the final product, AOD. The green ‘AltFast’ box represents the alternative simulation method ATLFAST [59], discussed in Section 4.1. Finally, the blue box shows the stage at which the actual ATLAS data events begin processing.

generation will be discussed in Section 4.1; the reconstruction of physics object, such as “electrons”, “photons”, “muons”, “jets”, in both real data and simulated MC events will be presented

The ATLAS software framework Athena [60], which is based on the Gaudi [61] framework developed by the LHCb collaboration [36], is used to reconstruct physics objects to be used by analysers, as the data collected and recorded by the ATLAS detector requires processing. The Athena framework is capable of dealing with various aspects of the experiment software, e. g. triggering or the processing of simulated data. Custom software, in particular Monte Carlo (MC) simulations, is used to simulate physics events used to model background and signal processes. These are produced through different stages, as shown in Figure 4.1, the last of which produces an analyser-friendly output.

In this chapter the stages will be briefly explained as it follows: event gen-

in Section 4.2.

4.1 Generation of Monte Carlo-simulated events

MC event generators [62] are extensively used in particle physics to simulate physics processes. A combination of perturbative and phenomenological calculations is employed, to produce randomly distributed physics events of a given type, with stable final state particles. As already mentioned in Chapter 2, the ATLAS detector collects pp - and heavy-ion-collision data. When two protons collide at such high energy in the centre of mass, the collision essentially occurs between the constituent partons¹. Three valence quarks (uud), the gluons mediating the strong interactions between the valence quarks, and the sea quarks produced in virtual $q\bar{q}$ pairs due to interacting gluons, are included as partons. Figure 4.2 shows one of these interactions which are known as Deep Inelastic Scattering (DIS) processes: the substructure of the proton is probed (therefore *deep*), by an incoming particle, in this case a proton, and the particles in the final states are in general different from the initial ones (therefore *inelastic*).

An important, yet simplifying, dimensionless physical quantity is the Bjorken scaling [65], which represents the fraction (x) of the proton momentum carried by an interacting parton. The measure of momentum transfer Q^2 in such events, is related to the momentum transferred by the exchanged boson q by $Q^2 = -q^2$. Parton Distribution Functions (PDFs) are used to describe mathematically the parton content of the colliding protons in order to model their interaction.

The pp scattering at the LHC can be categorised in processes such as *hard*, which can be described with perturbation theory, or *soft*, which involve non-perturbative QCD effects. Typically, a pp collision involves a hard scattering process between two partons, one for each proton, and a certain number of soft processes, such as Initial State Radiation (ISR), Final State Radiation (FSR), and Underlying Event (UE). The ISR involves particles, that are radiated by partons, which will interact in the hard process prior to their scattering. Partons which are not involved in the hard scattering process, the so-called *spectators*, form the UE. The FSR refers to particles that are radiated from the final state products of

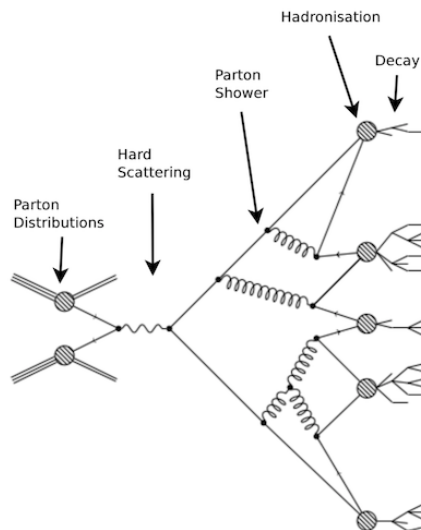


Figure 4.2: Example of a pp DIS event.

¹ “Feynman [63] interpreted the Bjorken scaling as the point-like nature of the nucleon’s constituents when they were incoherently scattered by the incident electron. Feynman named the point-like constituents partons. This is the parton model.”(taken from [64])

the hard scattering. Furthermore, *parton showering* is a process in which particles in the event that have colour can radiate gluons and/or produce $q\bar{q}$ pairs. Products of these showers will undergo the process of *hadronisation* during which colourless hadron states are produced if Q^2 is of the order of 1 GeV. Such a process occurs due to confinement.

In order to allow analysers to select samples with relevant processes, MC samples are divided in categories depending upon the hard-process specified before generation. For specific analyses, it is also possible to filter events to only produce a given final state, e. g. asking for zero leptons. This is done in order not to waste computational resources on events which would not pass analysis-specific selection criteria, therefore improving the available statistics. The effect of the selection is taken into account by applying filter efficiencies when the analysis is carried out. The HEPMC format is used to store the output of simulated data outputs [66].

Parton Distribution Function

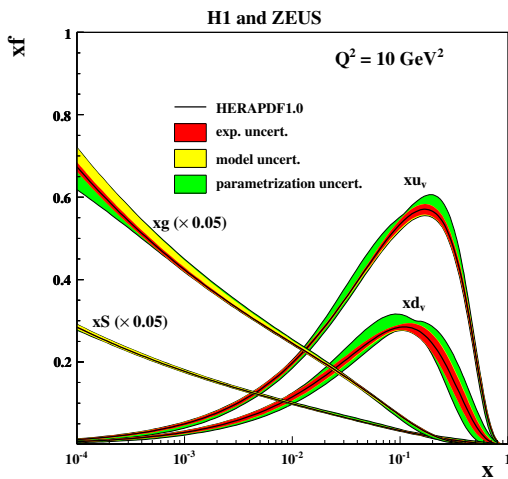


Figure 4.3: PDF from HERAPDF1.0, for up and down valence quarks xu_v and xd_v , gluons xg , and sea quarks $xS = 2x(\bar{U} + \bar{D})$, using a momentum transfer of $Q^2 = 10 \text{ GeV}^2$ (from [67]).

CTEQ [71] at $Q^2 = 10 \text{ GeV}^2$ for up and down valence quarks, gluons, and sea-quarks.

PDFs [68] describe mathematically the probability density of constituent partons of the interacting protons to have a given fraction (x) of the nucleon momentum. They depend upon the parton type, such as valence quark, gluon, or sea quark, and the momentum transfer Q^2 . Although perturbative calculations of the PDFs are not feasible, the DGLAP [69, 70] evolution equations, using a range of hard scattering data from both fixed target and collider experiments, can be used to estimate the dependence of the PDFs as a function of Q^2 for a given parton. In other words, PDFs describe the evolution of the structure functions of quarks and gluons as a function of the running² strong coupling constant α_s . Figure 4.3 shows the PDFs, calculated with input from HERA [67] and

Matrix Element

The hard part of the interaction process, Q^2 ($> \mathcal{O}(1 \text{ GeV})$), is simulated using the Matrix Element (ME) simulation. This involves standard perturbative QFT calculations which are still not simple to perform, and are usually carried out only to Leading Order (LO) or Next-to-Leading Order (NLO) in an expansion in α_s . The hard emission, namely the production of high mo-

² “Running” refers to a dependence on Q^2

mentum quarks and gluons in the event, can be added to the ME calculation, and in particular a number of process, such as gluon splitting into two gluons ($g \rightarrow gg$), a gluon decaying to a quark-antiquark pair ($g \rightarrow q\bar{q}$), and a quark radiating a gluon ($q \rightarrow gq$). Such processes can repeat and, as long as they occur at high Q^2 , they will be included in the ME calculation.

Parton Showers

Due to its non-perturbative nature, the emission of extra soft objects cannot be modelled with the ME. Parton Shower (PS) generators are instead used to include processes such as the emission of a gluon by a quark ($q \rightarrow qg$), or the emission of $q\bar{q}$ pairs $g \rightarrow qq$ or a gluon pair by a gluon $g \rightarrow gg$. HERWIG [72], PYTHIA [73], and SHERPA [74] collaborations have developed the most used PS models across the High-Energy Physics (HEP) community. Markov chains [75] are the heart of the algorithms used to simulate PS. These use probabilities that a gluon is radiated or a $q\bar{q}$ pair is produced.

At intermediate Q^2 , gluon/quark radiation may be treated as a hard emission or part of the PS, meaning that, in a given event double-counting might occur. To overcome such issue, the Catani-Krauss-Kuhn-Webber (CKKW) [76] and the Michelangelo L. Mangano (MLM) [77] schemes are employed to determine whether the emissions are part of the ME or PS. As the energy of the partons decrease below 1 GeV they will undergo hadronisation.

Hadronisation

As previously mentioned in Section 1.1, once the quarks and gluons in the final state reach a Q^2 of the order of $\Lambda_{\text{QCD}} \sim 200$ MeV, the recombination into colourless objects must occur. The modelling of the production of such bound state, the hadronisation, involves non-perturbative QCD and many more parameters than the parton showering. Phenomenological models, tuned using data, are then needed. The cluster model [78], used by HERWIG, and the Lund string model [79], used by PYTHIA, are the most employed.

Underlying Event

Partons not involved in the hard process of the event, referred to as the UE [80], can lead to a certain number of soft interactions at a lower energy scale, therefore producing additional hadronic activity in the event. Once again, phenomenological models are used to account for such effect which is modelled within SHERPA and PYTHIA where a whole lot of additional free tuned-to-data parameters are included. More details can be found in [80].

Detector simulation

Although at this stage the output of the MC generators contains all the kinematic features of the event, it is not yet possible to compare simulated events to the ATLAS collected data, as the

interactions of the particles passing through the detectors are not yet included. The GEANT4 software [81], included within the ATLAS offline software, namely all the software made available for analysers to be used after the data have been collected, is used to simulate the energy deposited within the detector. In a first stage, the interactions of the particles with the various sub-systems is simulated; following this, a second stage converts energy deposits into detector-output-like signals (voltage, times, etc.). This is the so-called *digitisation*. The output is now produced with a format that is identical to the one produced by the ATLAS Trigger and Data Acquisition system, therefore MC and collected ATLAS data can now be consistently processed by the same trigger and reconstruction software. In addition, to fully simulate the data the ATLAS Collaboration also uses fast simulation software such as ATLFast-II (AF2) [59], where, in order to reduce the usage of the available computational resources, a parametrised description of the showers in the calorimeters is implemented.

4.2 Object Reconstruction

Once MC samples are digitised, the signals have to be turned into tracks and calorimeter deposits which, in turn, have to be processed to be reconstructed into physics object: electrons, photons, muons, jets, taus, and missing energy, E_T^{miss} . Initially, a set of loose definitions is employed in order for various analyses to use such objects. Later, a set of tighter cuts can be applied depending on what a particular analysis needs to focus on. This approach increases the purity of the selected objects at the expense of selection efficiency. The criteria used to define the physics objects, relevant to the analysis presented in this thesis, will be presented in the following paragraphs.

Tracks and vertices

When a charged particle passes through the detector, all the ID sub-systems (pixel, SCT and TRT components), register “hits” and then, tracing the particle’s trajectory, the hits are reconstructed into a “track”. The most used algorithm is the so-called *inside-out* method: it works outwards from the centre of the ID to produce a track once it has initially grouped together hits in the pixel and SCT sub-systems. If this track is then compatible with hits in the TRT detector, then these hits are also included and the track is accepted. On the contrary, the *back-tracking* algorithm tries to reconstruct a track starting from the TRT to the SCT and Pixel detectors. Tracks can also be reconstructed using only the hits in the TRT. A number of selection cuts are applied to the tracks in order to achieve the required quality. Signals produced in other parts of the detector are then used to match ID tracks up with charged-particle candidates, e.g. ECAL cluster for an electron track. The η and ϕ values are then assigned to tracks using their direction with respect to the origin³ in the co-ordinate system described in Section 2.2. The relation that links the p_T of a track to its bending radius and the magnetic field is $p_T = 0.3 \times B \times R$,

³ This is assumed to be the position of the primary interaction

where the p_T is given in GeV, the magnetic field B in Tesla, and the radius R in meters. Moreover a set of variable is defined:

- d_0 : the distance of closest approach between the track and the origin
- z_0 : the z -plane component of d_0 ;
- $z_0 \sin \theta$: the projection of d_0 onto the z -axis

For every bunch crossing, the average number of interactions $\langle \mu \rangle$, often referred to as *pile-up*, can be computed. In particular, this was computed in both Run 1 and 2 and it was found to be $\langle \mu \rangle \sim 21$ and $\langle \mu \rangle \sim 32$, respectively. Vertex reconstruction is needed for various purposes e. g. to differentiate objects produced in the hard scattering from other pile-up interactions. As the bunch length is finite, pp interactions are spread out along the z coordinate. In order to reconstruct the PV, i. e. the vertex associated to the hard scattering interaction, tracks are back-tracked to the beam line. Table 4.1 shows a set of cuts applied to the reconstructed ID tracks to be used for vertex reconstruction.

Table 4.1: Cuts applied to the tracks. In particular the # of shared modules refers to 1 shared Pixel hit or 2 shared SCT hits; # of Pixel holes refers to holes that exist when a hit is expected in a layer of sensors given the fitted trajectory of the track but none is found; # Si hits refers to hits in the IBL, Pixel and SCT.

Variable	Cut
p_T	> 400 MeV
$ \eta $	< 2.5
# IBL hits + B Layer hits	≥ 1
# shared modules	≤ 1
# Pixel holes	$= 0$
# SCT holes	≤ 1
# Si hits	≥ 9 if $ \eta \leq 1.65$
	≥ 11 if $ \eta > 1.65$

A global maximum in the z coordinate of reconstructed tracks is searched for first, to find a vertex seed. The vertex position is then fitted using an algorithm called the *Adaptive Vertex Fitting* algorithm [82, 83]. The vertex position is determined by fitting to ID tracks with the least squares fitting method. Outlier tracks, defined as tracks that are far from the vertex centre, are assigned lower weights in the fit than tracks close to the vertex centre. Outlier tracks are likely to be noise tracks that do not actually originate from the vertex the algorithm tries to reconstruct. By weighting these tracks less in the fit, the adaptive fitting algorithm is able to decrease sensitivity to these noise tracks. As the true position of the vertex centre, and which tracks are outliers, is not known a priori, the algorithm iteratively tries to fit the vertex: all tracks weights are initialised with high values and after each fit iteration the weight of the outlier tracks is decreased. The algorithm then determines both the vertex centre and which tracks are outliers

with increasing accuracy after each iteration. Finally, the algorithm will stop once the fitted vertex centre does not change any more. Once a vertex is found, tracks which are incompatible with the found vertex will form a new vertex seed. The vertex reconstruction process will terminate once all the tracks have been clustered into vertices or no additional vertices can be found. Among all the vertices found by the algorithm, the PV will be the one with the highest sum of the squared momenta of the associated tracks ($\sum p_T^2$). The remaining primary vertices found by the algorithm, if any, are referred to as pile-up vertices. Further detail about the algorithm can be found in references [82, 83].

Secondary vertices (SVs) can also be reconstructed by looking at the displacement, with respect to the PV position, due to the distance travelled by a decaying particle whose lifetime is sufficiently long for the decay length e.g. b -quarks, which travel a few millimetres.

Electrons and Photons

The reconstruction of electrons and photons employs a *sliding-window algorithm* [84, 85] that looks for clusters of energy deposits in the ECAL, performing a scan over blocks of 3×5 cells, each measuring $\Delta\eta \times \Delta\phi = 0.025 \times 0.025$. Electron candidates are reconstructed as clusters matched to a track in the ID, and after the matching the calorimeter cluster is rebuilt using blocks of 3×7 cells in the barrel and 5×5 in the end-caps. Photon candidates are clusters with no ID tracks matched, however it is also possible to reconstruct converted photons which produce an $e^+ e^-$ pair before reaching the ECAL. In particular, once the identified clusters are matched to reconstructed ID tracks (required to have a minimum number of pixel and silicon hits) a cluster is either considered as an electron or a photon candidate, if it satisfies one of the following criteria:

electron: one single reconstructed ID track with an associated vertex;

unconverted photon: no ID tracks;

converted photon: two opposite-signed collinear tracks (consistent with electrons) are associated with a secondary vertex;

converted photon: single track is present but there are missing hits in the IBL

In order to achieve better cancellation of systematics when using electrons to measure the photon response, the same window size is employed for electrons and photons [84]. Monte-Carlo-based algorithms and data-driven corrections, derived from $Z \rightarrow ee$ events, are employed to carry out energy calibration [84]. Figure 4.4 shows an illustration of the electron reconstruction algorithm.

Once electrons and photons have been reconstructed an additional set of criteria is employed to rule out any potential misidentification. In particular, the identification is based on a Likelihood (LH) algorithm that depends on variables such as shower shape, radiation deposited in the TRT, and associated-track properties. Identification Working Points (WPs), i. e.

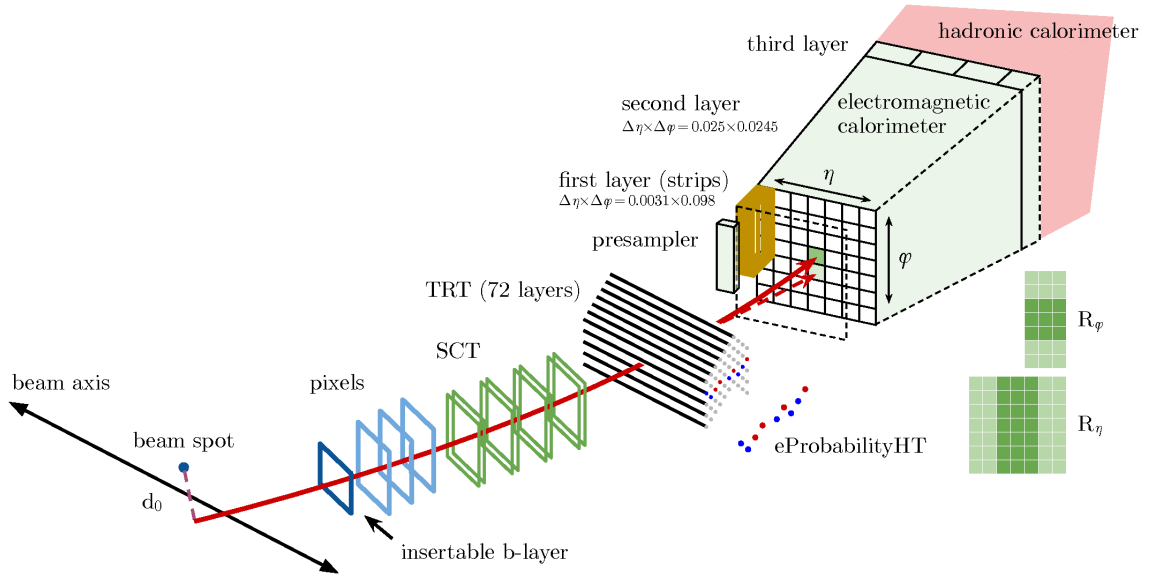


Figure 4.4: Schematic view of the electron reconstruction and identification (taken from [86]).

Loose, Medium and Tight, are employed to identify electrons using different selections, which will reflect in different efficiencies and purities:⁴ the tighter the identification is, the purer the selected object will be. Figure 4.5 shows the reconstruction and identification efficiencies using 2016 data for electrons, and 2015 + 2016 for unconverted photons. Here, the data-MC discrepancy in the electron identification performance is due to a mis-modelling of the TRT conditions in addition to known mis-modelling of calorimeter shower shapes in the GEANT4 detector simulation [87]. Nonetheless, scale factors were derived from data and applied to the Monte Carlo, to match the performance observed in the data.

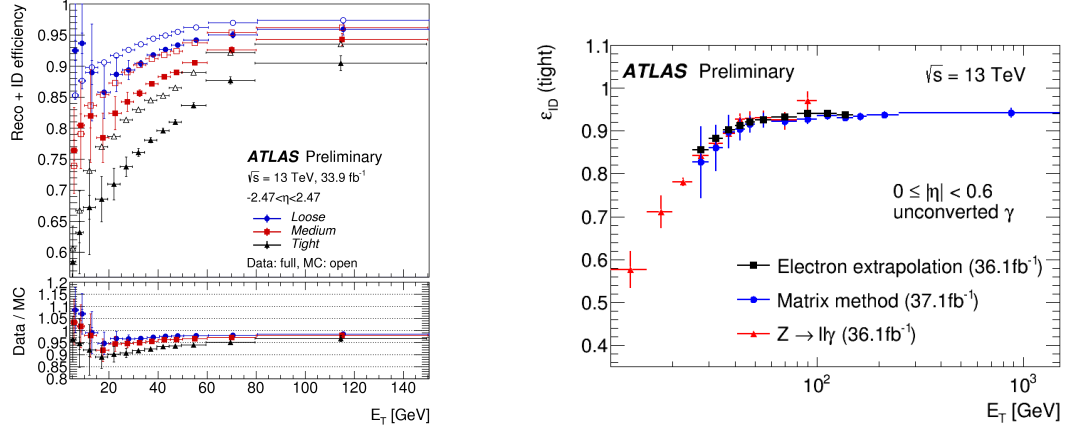
The shower shape and the amount of hadronic activity behind the electromagnetic (EM) cluster are at the heart of photon identification. The EM showers originating from photons and those originating from neutral mesons e. g. π_0 can be distinguished by looking at the energy deposited in the cells within the first and second layer of the ECAL [89]. Two categories of photons are reconstructed employing two identification WPs: Loose and Tight. The former are typically used for triggering, the latter for physics analysis, such as the one presented in Chapter 5, where, the top-quark pair production in association with a photon, $t\bar{t}+\gamma$ was studied.

Muons

The muon selection procedure employs with two independent track fits in the ID and MS and these are combined using different algorithms. A set of categories of muons can be reconstructed with the ATLAS detector [90] and they can be listed as it follows:

Combined: a global refit on ID and MS tracks is run to obtain a combined muon track that describes the trajectory of the particle through the whole detector, in order to take into

⁴ Defined as number of actual electrons (photons) among the selected candidates.



(a) Electron reconstruction and identification efficiencies in $Z \rightarrow ee$ events as a function of E_T , integrated over the full pseudo-rapidity range. The data efficiencies are obtained by applying data/MC efficiency ratios that were measured in $J/\psi \rightarrow e^+e^-$ and $Z \rightarrow ee$ events to MC simulation. The total statistical and systematic uncertainty is shown.

(b) Photon identification efficiencies using the full 2015 + 2016 dataset. Comparison of the data-driven measurements (radiative Z decay, electron extrapolation and matrix method [88]) of the identification efficiency for unconverted photons as a function of E_T in the region $10 \text{ GeV} < E_T < 1500 \text{ GeV}$ for the pseudo-rapidity interval $|\eta| < 0.6$. The error bars represent the sum in quadrature of the statistical and systematic uncertainties estimated in each method.

Figure 4.5: Electron and photon reconstruction and identification efficiencies (taken from [87]).

account the energy loss in the calorimeter, when muon candidates are found to match tracks in both ID and MS;

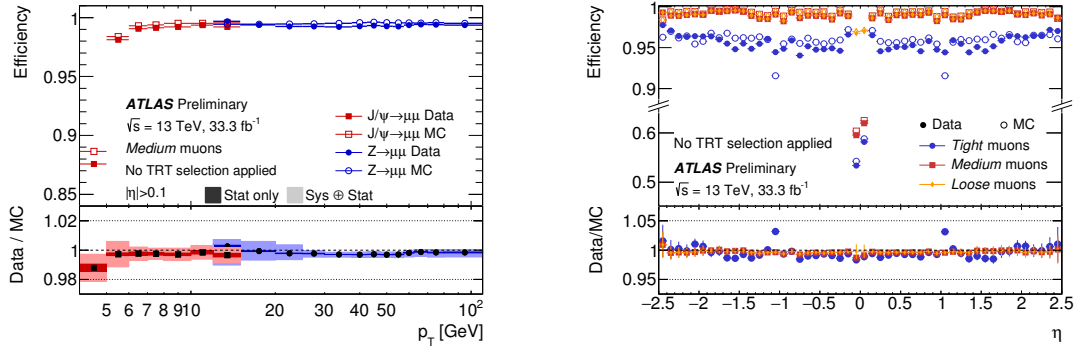
Extrapolated: candidates in the forward region ($2.5 < |\eta| < 2.7$) that produced a track in the MS but fell outside the ID acceptance, therefore their trajectory is reconstructed using the MS track, loosening its compatibility requirement with the interaction point;

Segment tagged: candidates whose tracks in the ID are found to have a corresponding hit in the inner layer of the MS. These are generally muons with low p_T or which fell into the cracks in the MS;

Calorimeter tagged: candidates whose ID tracks can be matched with an energy deposit in the calorimeter compatible with the signature of a Minimum Ionising Particle (MIP), with no associated MS tracks. These are mainly muons in the central pseudo-rapidity region ($|\eta| < 0.1$) which fell into a crack in the barrel of the MS;

In order to separate prompt muons from those coming from pion and kaon decays, further identification requirements are employed, e. g. track quality requirements in the ID and the MS, normalised χ^2 of the combined ID-MS track fit, etc.

Figure 4.6 shows reconstruction and identification efficiencies as a function of p_T and η . For electrons and photons, in order to meet all the different requirements of the various ATLAS



(a) Muon reconstruction efficiencies for the Medium identification algorithm measured in $J/\psi \rightarrow \mu\mu$ and $Z \rightarrow \mu\mu$ events as a function of the muon p_T . The prediction by the detector simulation is depicted as empty circles (squares), while the full circles (squares) indicate the observation in collision data for $J/\psi \rightarrow \mu\mu$ ($Z \rightarrow \mu\mu$) events. Only statistical errors are shown in the top panel. The bottom panel reports the efficiency scale factors. The darker error bands indicate the statistical uncertainty, while the lighter bands indicate the quadratic sum of statistical and systematic uncertainties.

(b) Muon reconstruction efficiencies for the Loose/Medium/Tight identification algorithms measured in $Z \rightarrow \mu\mu$ events as a function of the muon η for muons with $p_T > 10$ GeV. The prediction by the detector simulation is depicted as open circles, while filled dots indicate the observation in collision data with statistical errors. The bottom panel shows the ratio between expected and observed efficiencies, the efficiency scale factor. The errors in the bottom panel show the quadratic sum of statistical and systematic uncertainty.

Figure 4.6: Muon reconstruction and identification efficiencies (taken from [91]).

analyses, a set of WPs is defined. The performance is calibrated using the so-called tag-and-probe method⁵ in $Z \rightarrow \mu\mu$ or $J/\psi \rightarrow \mu\mu$ events. Further details can be found at [90].

Jets

As already mentioned in Sections 1.1 and 4.1, due to QCD confinement when a pp collision occurs, a spray of hadronic matter, or *jet*, is produced. A jet in the ATLAS detector is an object that released its energy in both ECAL and HCAL via EM and hadronic showers and, as it is generally comprised of a certain number of charged particles, it also has ID tracks associated with the showers. The identification and the reconstruction of jets is important for the analysis discussed in Chapter 5, which targets the $pp \rightarrow t\bar{t} \rightarrow bqq\tilde{\chi}_1^0 + \bar{b}\bar{q}\tilde{\chi}_1^0$ channel where all the visible decay products are quarks, therefore jets. A brief description of jet reconstruction and calibration is presented here.

Jets are reconstructed clustering energy deposits in the calorimeter. First, calorimeter cells are clustered into topological clusters (topo-clusters)[93, 94] which essentially starts as a single calorimeter cell that passes a 4σ signal-above-noise threshold called a seed cell, then cells neighbouring the cluster are added to the cluster if they pass a 2σ signal-over-noise threshold. Each time a cell is added to the cluster, cells neighbouring the newly added cell are also considered to be neighbours of the cluster, and so the cluster grows until no new neighboring cells

⁵ Method used to select, from known resonances such as $Z \rightarrow ee$ unbiased samples of electrons (probes) by using strict selection requirements on the second object produced from the particle's decay (tags) [92].

are added due to not passing the signal-over-noise threshold. The last round of neighbouring cells is added regardless of the signal-to-noise threshold in those cells [95]. Jet-finding algorithms, which treat jets as massless objects with four-vectors of energy $E = \sum_i E_i^{\text{cell}}$, are then fed with energy and position information of such clusters. The standard algorithm within the ATLAS Collaboration is the anti- k_t one which forms a collection of jets as output by iteratively recombining the input clusters. The algorithm essentially groups two object into a single one according to a distance d_{ij} , defined as:

$$d_{ij} = \min \left(k_{t_i}^{2p}, k_{t_j}^{2p} \right) \frac{\Delta_{ij}^2}{R^2} \quad (4.1)$$

where i and j are topological cluster indices, k_t is the transverse momentum of each topological cluster, $\Delta_{ij}^2 = \Delta\phi_{ij}^2 + \Delta\eta_{ij}^2$ is the distance between the two topological clusters, and R is an input parameter into the algorithm which, in the analysis presented in this work, is set to $R = 0.4$. The topological clusters i and j which minimise d_{ij} are then combined to form larger individual clusters. The next iteration takes into account the larger individual clusters as well as the remaining initial topological clusters and combines them according to the same procedure, which is repeated until all remaining topological-cluster pairs satisfy $\Delta_{ij} > R$. Additional information can be found at [96].

The calorimeters response can be described in terms of the EM/Hadronic ratio, as this is a measure of how the calorimeter responds to EM and hadronic radiation: an ideal calorimeter would have EM/Hadronic ~ 1 . Due to this effect, called *compensation condition*, the hadronic component of the shower produced by jets is underestimated and for such reason a calibration procedure is employed. In particular, the so-called Electromagnetic + Jet Energy Scale scheme is employed [97] where a set of corrections is applied to match the energy of the initial partons. It is possible to define the Jet Energy Scale (JES) by employing the following corrections:

vertex correction: once the anti- k_t algorithm has reconstructed the jets, its four-vectors, initially pointing at the centre of the detector, are adjusted to point to the primary vertex;

pile-up correction: pile-up effect on the jets energy is reduced by using an area-based subtraction procedure [98];

jet energy and η correction: additional calibration based on energy and pseudo-rapidity corrections where the kinematical properties of the reconstructed jet (p_T and η) are compared to the ones derived from MC simulations;

global sequential correction: individual jet property-based correction for properties such as the fraction of energy deposited in different calorimeter layers or the number and type of associated tracks [99];

in-situ corrections: then measured p_T of the jet is corrected using multi-jet and $\gamma/Z+jets$ events, where the momentum of a *probe* jet is balanced against a well-measured reference object [100].

Finally, the Jet vertex Tagger (JVT) variable [101], related to the fraction of charged tracks within the jets that point to the primary vertex, is employed. This observable tests the compatibility between the reconstructed jet and the hard-scatter charged particles within the jet [102].

b-tagged jets

The identification and the reconstruction of jets originated from b -quarks is also important, as they also are part of the final state of the analysis presented in this work. The standard jet-reconstruction procedure discussed above applies to b -jets too, with the addition of dedicated algorithms (b -tagging [104]) employed to spot a b -hadron within their cone. A diagram, showing the difference between light jets and b -jets is shown in Figure 4.7. Due to their lifetime ($\sim 10^{-12}$ s), b -hadrons can travel a measurable distance in the detector before decaying (~ 1 mm for a 20-GeV b -jet), therefore producing a SV which, together with a requirement on the impact parameter d_0 , already provides a useful discrimination tool for jet flavour. Unfortunately, c -jets also leave a similar signature within the ATLAS detector. Although on average they travel a shorter distance due to their shorter lifetime [105], their presence introduces a source of background for b -tagging.

Algorithms for b -tagging, such as, *I2PD* and *I3PD* [106]⁶, *Secondary Vertex Finding* [107], and *Decay Chain Multi-Vertex Algorithm (JetFitter)* [108], are widely employed within the ATLAS Collaboration. Their outputs are combined to feed a single multivariate tagger, Multivariate algorithm (MV2), which is used by many analyses as it is, as of today, the algorithm with the highest discriminating power for jet flavour tagging. In particular, MV2 is a Boosted Decisions Tree (BDT) algorithm [109] implemented within the ROOT TMVA [110, 111] and is provided in three different versions: MV2c00, MV2c10, and MV2c20. MV2c00 denotes the MV2 algorithm where no c -jet contribution was present in the training. MV2c10 (MV2c20) denotes the MV2 outputs where a 7% (15%) c -jet fractions was present in the background sample [104] and it was used for the analyses presented in this thesis.

Figure 4.8 shows the performances of different configuration of such tagger. In particular, the b -tagging efficiency is compared to the c -jets and light-jet rejection which can be defined as the inverse of the mis-tag rates. Furthermore, the more c -jet there are in the background

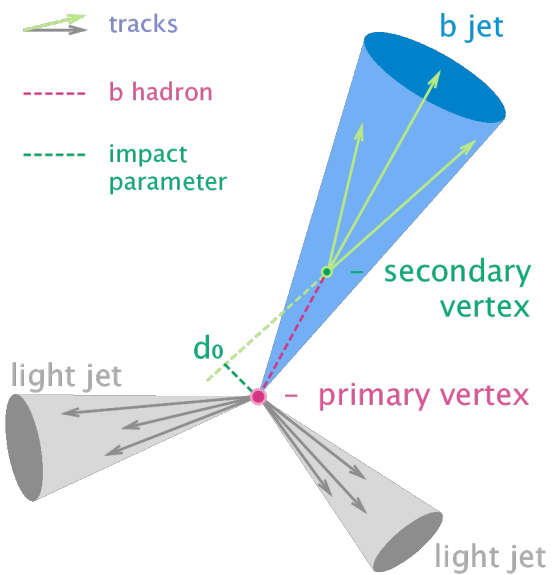


Figure 4.7: Diagram showing the common principle of identification of jets initiated by b -quark decays [103].

⁶ The significance of the transverse impact parameter (IP) of the tracks, d_0/σ_{d_0} is used by both algorithms

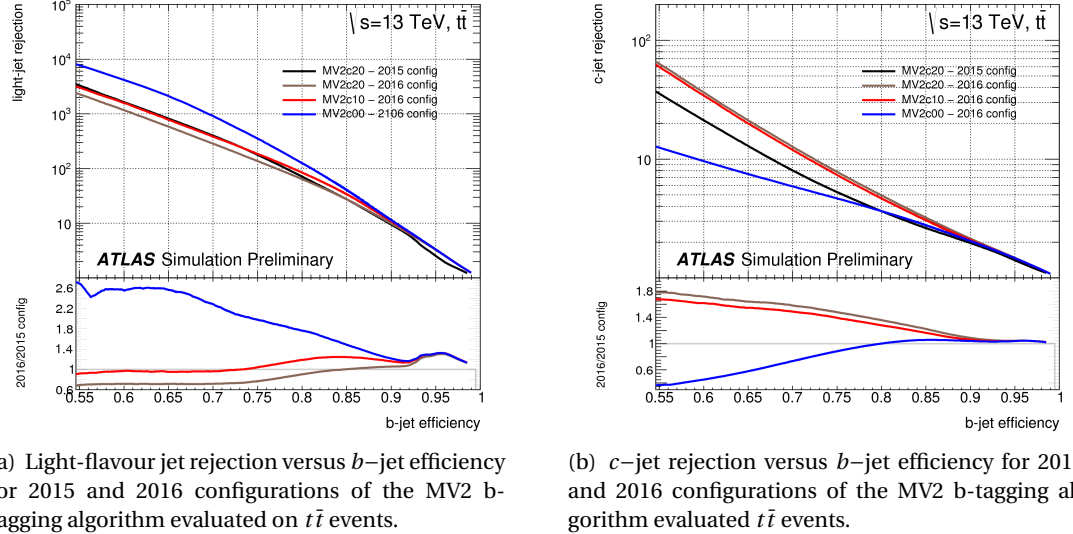


Figure 4.8: Performance of the MV2 tagger in $t\bar{t}$ events. Various fractions of c -jets in the background training sample were considered (taken from [112]).

training sample the better the rejection will be, as opposite to the case where no c -jets are included.

Missing Transverse Energy, E_T^{miss}

As previously mentioned, particles like neutrinos or potential DM candidates escape the ATLAS detector. When these particles are produced a momentum imbalance in the transverse plane will characterise the event, as shown in Figure 4.9 where a simulated event with two jets and E_T^{miss} is displayed. The missing transverse momentum ($\mathbf{p}_T^{\text{miss}}$) can be estimated using the four-momenta of all the visible detected objects in the event, and it is called missing transverse momentum, $\mathbf{p}_T^{\text{miss}}$ [114]. It provides an estimate of the total momentum of the particles that escaped the ATLAS detector and it is defined as it follows:

$$\mathbf{p}_T^{\text{miss}} = - \sum_i \mathbf{p}_T^{i,\text{obj}} \quad (4.2)$$

Here, $\mathbf{p}_T^{i,\text{obj}_i}$ represents the transverse momentum of the i -th visible object in the event. The Missing Transverse Energy E_T^{miss} , is therefore defined as the magnitude of $\mathbf{p}_T^{\text{miss}}$.

The E_T^{miss} is reconstructed by selecting calibrated hard objects to measure the missing transverse momentum in the event. In particular the $(x - y)$ components of the E_T^{miss} are calculated as it follows:

$$E_{x(y)}^{\text{miss}} = E_{x(y)}^{\text{miss},e} + E_{x(y)}^{\text{miss},\mu} + E_{x(y)}^{\text{miss},\tau} + E_{x(y)}^{\text{miss,jets}} + E_{x(y)}^{\text{miss},\gamma} + E_{x(y)}^{\text{miss,soft}} \quad (4.3)$$

where each object term is given by the negative vectorial sum of the momenta of the respective calibrated objects. In the analyses presented in this work, terms containing τ leptons

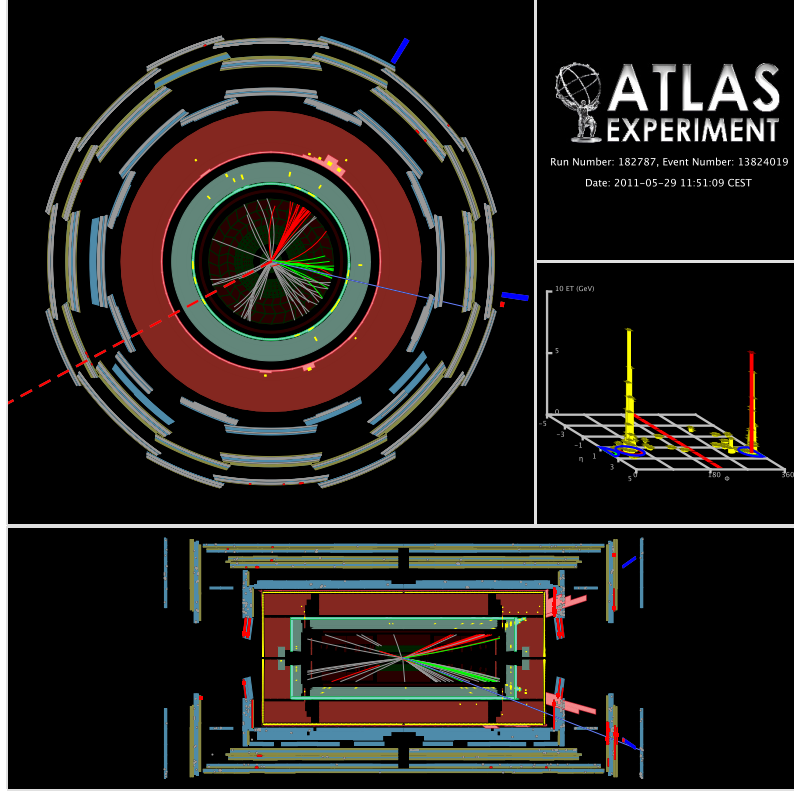


Figure 4.9: ATLAS Event display for an event that has jets (blue solid lines) and E_T^{miss} (red dashed line) (taken from [113]).

were not considered as τ reconstruction was never explicitly performed. The *soft term* is reconstructed from detector signal objects not associated with any object passing the selection cuts, e. g. ID tracks (track-based soft term) or calorimeter signals (calorimeter-based soft term). From the components in Equation 4.3 the magnitude of E_T^{miss} and the azimuthal angle ϕ^{miss} are calculated as it follows:

$$E_T^{\text{miss}} = \sqrt{\left(E_x^{\text{miss}}\right)^2 + \left(E_y^{\text{miss}}\right)^2} \quad ; \quad \phi^{\text{miss}} = \arctan\left(\frac{E_y^{\text{miss}}}{E_x^{\text{miss}}}\right) \quad (4.4)$$

The E_T^{miss} performance is studied in two complementary topologies, with and without genuine E_T^{miss} , such as $W \rightarrow ev$ and $Z \rightarrow \mu\mu$, in both data and MC in order to test the reconstruction algorithms and correct for any potential biases.

ANALYSIS STRATEGY AND OPTIMISATION

5

However beautiful the strategy, you should occasionally look at the results.

Winston Churchill

In this chapter one of the author’s main contribution will be presented, namely the analysis strategy, together with the optimisation of the search for the direct pair-production of the supersymmetric partner of the top quark in all-hadronic final states using a dataset of 36.1 fb^{-1} pp collisions at a centre-of-mass energy $\sqrt{s} = 13\text{ TeV}$. In particular, an excursus on the simplified SUSY models considered will be presented in Section 5.1; the objects used in both data and MC will be discussed in Section 5.2; the selection of the events will be discussed in Section 5.4; an overview of the SM backgrounds, and the samples used, will be presented in Section 5.5; finally, the signal region optimisation strategy will be extensively discussed, as one of the main contribution of the author to the analysis, in Section 5.6.

5.1 SUSY signals

As already introduced in Section 1.2.2, the signals considered in this work are generated using simplified models, meaning that only the \tilde{t} , the $\tilde{\chi}_1^0$, the $\tilde{\chi}_2^0$, and the $\tilde{\chi}_1^\pm$, are the SUSY particles considered. In particular, in such models, either $\tilde{\chi}_2^0$ or $\tilde{\chi}_1^\pm$ is assumed to be the NLSP and, the chargino-neutralino mass splitting $\Delta m(\tilde{\chi}_1^\pm, \tilde{\chi}_1^0)$ is assumed to be 1 GeV, in accordance with the naturalness argument. This implies that the $\tilde{\chi}_1^\pm$ will promptly decay to $W^* \tilde{\chi}_1^0$, with the W emitted as a virtual particle. The decay products of the so-created virtual W will therefore be low p_T objects which will not be reconstructed by the ATLAS detector.

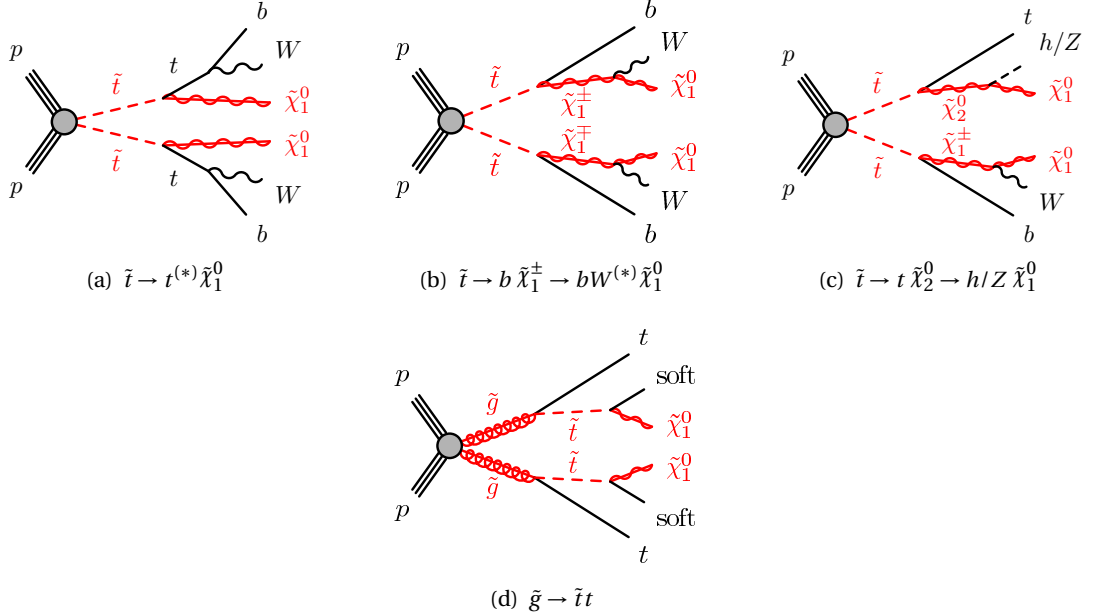


Figure 5.1: Diagrams of the decay topologies of the signal models considered in this work.

5.1.1 Benchmark processes

Figure 5.1(a)–(c) shows the diagrams corresponding to the decay scenarios considered in this work. In particular, (a) where both top squarks decay¹ via $\tilde{t} \rightarrow t^{(*)} \tilde{\chi}_1^0$ (one-step decay); (b) where at least one of the stops decays via $\tilde{t} \rightarrow b \tilde{\chi}_1^\pm \rightarrow b W^{(*)} \tilde{\chi}_1^0$ (two-step decay); (c) where $m_{\tilde{\chi}_2^0}$ is small enough to allow one stop to decay via $\tilde{t} \rightarrow t \tilde{\chi}_2^0 \rightarrow h/Z \tilde{\chi}_1^0$ where h is the SM Higgs boson. Essentially, the experimental signatures searched for in this analysis are characterised by the presence of four or more jets and missing transverse momentum.

The results of the analysis presented in this and the following chapters were interpreted in the simplified models where only one- and two-step decays scenarios are allowed and, as already mentioned, the latter will be referred to as a natural SUSY-inspired mixed grid, i.e. $\Delta m(\tilde{\chi}_1^\pm, \tilde{\chi}_1^0) = 1 \text{ GeV}$ [115, 116, 117]. Furthermore, in both scenarios the LSP is considered to be a pure bino state. The results will also be interpreted in two slices of the pMSSM models: wino-NLSP and well-tempered neutralino pMSSM [118, 119]. A fourth scenario, in addition to direct pair production, was considered: top squarks can also be indirectly produced via gluino decays, as illustrated in Figure 5.1 (d). In such model, the mass difference between the top squark and the neutralino is considered to be relatively small, $\Delta m(\tilde{t}_1, \tilde{\chi}_1^0) = 5 \text{ GeV}$, allowing the jets originating from \tilde{t}_1 decay to have a p_T below the reconstruction threshold of the ATLAS detector resulting in an experimental signature nearly equivalent to the one in Figure 5.1(a).

¹ The symbol (*) indicates off-shell production

5.1.2 MC samples

A grid of points across the $(m_{\tilde{t}_1} - m_{\tilde{\chi}_1^0})$ plane with a 50-GeV spacing is generated to simulate the above-mentioned simplified models. The signal models were generated using MG5_aMC@NLO 2.2-2.4 [120] interfaced to PYTHIA8 [121] for the PS and hadronisation. EvtGen 1.2.0 [122] was employed for the decays of the b - and c -hadrons. The tree-level ME calculation includes the emission of up to two additional partons for all signal samples. The NNPDF2.3LO PDF [123] set was used to generate the signal samples with the A14 [124] tune for the UE and shower parameters. Additionally, the CKKW prescription [125] was used for the ME-PS matching.

The various signal cross sections were all calculated to next-to-leading order in the strong coupling constant, with the addition of soft-gluon emission re-summation at next-to-leading-logarithm accuracy (NLO+NLL) [126, 127, 128]. The sparticle mass spectra for pMSSM models were calculated using Softsusy 3.7.3 [129, 130] while the decays of each sparticle were performed by HDECAY 3.4 [131] and SDECAY 1.5/1.5a [132]. Finally, various PDF sets, factorisation, and re-normalisation scales were used to generate an envelope of cross-section predictions, within which a nominal value and uncertainty were chosen. Further details can be found in [30].

5.2 Objects definition

The physics objects used in this analysis are obtained using the algorithms discussed in Section 4.2. They are required to pass a first loose selection to be categorised as *baseline* objects. An additional procedure is employed to remove potentially overlapping objects, e. g. a lepton that is identified as a jet, or a lepton that falls within the same jet cone. A so-called Overlap Removal (OR) procedure, whose inputs are two baseline objects, is employed to resolve such ambiguities by discarding one of the two objects by looking at their distance (ΔR) and applying some selection criteria, as shown in Table 5.1.

Table 5.1: List of the possible ambiguities with relative criteria and decisions.

Ambiguity	Criterion	Object kept	Object removed
electron/jet	$\Delta R(e, \text{jet}) < 0.2$	electron	jet
	$0.2 \leq \Delta R(e, \text{jet}) < 0.4$	jet	electron
electron/ b -jet	$\Delta R(e, b\text{-jet}) < 0.2$	b -jet	electron
muon/jet	$\Delta R(\mu, \text{jet}) < 0.4$ and $N_{\text{tracks}} < 3, p_T^{\text{track}} > 500 \text{ MeV}$	muon	jet
photon/electron	$\Delta R(e, \gamma) < 0.4$	electron	photon
photon/muon	$\Delta R(\mu, \gamma) < 0.4$	muon	photon
photon/jet	$\Delta R(\text{jet}, \gamma) < 0.4$	jet	photon

The data-driven estimation of $t\bar{t}+Z$ events using $t\bar{t}+\gamma$ (discussed in Section 6.2) is the only part of the analysis that used reconstructed photons. In particular, the OR is modified accordingly to avoid that an object will appear in multiple collections (double-counting). The various baseline and signal objects are defined as:

Electrons baseline electrons are required to have $|\eta| < 2.47$, $p_T > 7$ GeV and have to pass a VeryLoose likelihood-based selection (further details in [133, 134]). Electron candidates which pass the OR, have a $p_T > 20$ GeV ($p_T > 28$ GeV) in events selected with a E_T^{miss} (lepton) trigger, satisfy $d_0/\sigma_{d_0} < 5$, $z_0 \sin \theta < 0.5$, and pass a Tight likelihood-based selection isolation, are identified as “signal” electrons;

Muons baseline muons have to pass a Loose selection [135], satisfy $|\eta| < 2.7$ and $p_T > 6$ GeV. Further requirements are imposed on muon candidates to tag them as signal. In particular, they have to pass the OR, a Medium quality selection [135], and satisfy $|d_0| < 3\sigma_{d_0}$ and $|z_0 \times \sin \theta| < 0.5$. Additionally, the p_T requirement is tightened up to 20 GeV (28 GeV) in regions with a E_T^{miss} (lepton) trigger;

Photons baseline photons have to pass a Tight [88] selection, and have $p_T > 25$ GeV and $|\eta| < 2.37$. Additionally, baseline photon candidates are required to have $p_T > 130$ GeV and satisfy a tighter isolation selection, in order to be tagged as signal;

Jets as already mentioned in Chapter 4.2, jets are reconstructed using the anti- k_t algorithm with $R = 0.4$. Baseline jets are required to have $p_T > 20$ GeV and $|\eta| < 4.8$. Signal jets have to pass the OR, satisfy the JVT requirement, and have $|\eta| < 2.8$ and $p_T > 20$ GeV.

b-tagged jets baseline jets in the event are identified as originating from the decay of a b -quark is based on the MV2c10 jet tagger which uses the a 77% fixed-cut WP. The p_T threshold applied to signal jets is also applied to b -jet and the requirement on the pseudorapidity is relaxed down to $|\eta| < 2.5$.

Missing transverse energy The E_T^{miss} is reconstructed as described in Section 4.2. Baseline muons, electrons, and jets after overlap removal are used in the E_T^{miss} recalculation.

Additionally, in the analysis carried out during Run-1 [136] another E_T^{miss} -related quantity was introduced. The track-based E_T^{miss} , derived from the sum of the p_T of the tracks associated with the objects in the event was found to have discriminating power to reject fake E_T^{miss} . The $\mathbf{p}_T^{\text{miss,track}}$, whose magnitude is $E_T^{\text{miss,track}}$, from the tracking system is computed using the vector sum of the reconstructed inner detector tracks, $\mathbf{p}_T^{\text{miss,track}} = \sum_i^{\text{tracks}} \mathbf{p}_T^i$, with $p_T > 500$ MeV and $|\eta| < 2.5$, that are associated with the PV in the event.

Ultimately, leptons are also required to satisfy p_T -dependent track- and calorimeter-based isolation criteria. The calorimeter-based isolation is determined by taking the ratio of the sum of energy deposits in a cone of $R = 0.2$ around the electron or muon candidate and the energy deposits associated with the electron and muon. The track-based isolation is estimated in a similar way but using a variable cone size with a maximum value of $R = 0.2$ for electrons and

$R = 0.3$ for muons. An isolation requirement is made that is 95% efficient for electron or muon candidates with $p_T = 25$ GeV and 99% for candidates with $p_T = 60$ GeV.

5.3 Triggers used

As previously discussed in Chapter 2 and 3, physics events are recorded once they passed a certain trigger. In particular, a E_T^{miss} trigger is used to select events that fall in signal-enriched regions, SR, where no leptons, but jets and missing E_T are required; a single-lepton (or photon) trigger is used to select events in background-enriched regions, where 1-lepton (or photon) is required. A breakdown of all the lowest unprescaled online triggers used will be presented below.

Once the E_T^{miss} is reconstructed from an input jet collection, events are selected with a missing E_T trigger by selecting a 70-GeV threshold in the 2015 dataset whereas, due to the increase in instantaneous luminosity (impact on the trigger rate), in 2016 the threshold was gradually raised to 90, 100, and 110 GeV. It can be seen (Figure 3.8) that for analysis purposes a cut of at least 200 GeV is required to stay in a region where the trigger is fully efficient (*plateau*);

Events are selected with a single-electron trigger by using a logic OR of three electron-trigger chains: the first consists of a 24-GeV threshold (26-GeV in 2016 data); the second chain uses a 60-GeV threshold without additional isolation requirement; the third uses a 120-GeV threshold to be efficient at high E_T . A $p_T^e > 27$ GeV cut is applied to both 2015 and 2016 datasets to stay in the plateau region;

Events are selected with a single-muon trigger by using a logic OR of two chains: a first chain with a 20-GeV threshold is used in data 2015 and 26-GeV threshold, together with an isolation requirement, in 2016; a second chain with a 50-GeV threshold is employed for both 2015 and 2016 data. A $p_T^\mu > 27$ GeV is applied to both 2015 and 2016 datasets to stay in the plateau region;

Events are selected with a single-photon trigger by using only one chain: a 120 GeV (140 GeV) threshold is employed in 2015 (2016). Additionally, in order to ensure full trigger efficiency a $p_T^\gamma > 150$ GeV cut is applied.

5.4 Event selection

A cut-and-count strategy is at the heart of the analysis presented here. Dedicated sets of discriminating variables are employed to isolate, where possible, the targeted signals from the main SM backgrounds. Equally, background-enriched regions are defined to *control* the modelling of such backgrounds. The number of events passing such selections is used as the main observable, to predict both signal and background processes either by means of MC samples, or using data-driven techniques. In general, a combination of the two is employed.

The ATLAS detector did not operate with the same conditions during 2015 and 2016: different triggers, and calibration parameters were used. In order for MC parameters to be modified

consistently with what is done in data, MC events are assigned a random number, which identifies an ATLAS run. This procedure provides consistency between the collected data and the simulated MC events.

5.4.1 Event cleaning

In order to remove events where a detector fault might have occurred, a set of offline cuts is applied to clean the used event sample. The first requirement for an event to be a good physics event is the existence of a primary vertex with a minimum of two tracks, with $p_T > 400$ MeV, associated with it. In addition, the status of both ECAL and HCAL for that event is checked: if any of the calorimeters returned an error state, the event is discarded. Furthermore, to reduce and suppress the fake-jet contamination a *bad jet* requirement is defined by introducing quality requirements on a variety of jet parameters, e. g. the fraction of energy deposited in the different layers of the calorimeters, and the fraction of jet p_T measured by the tracks in the Inner Detector. Events containing bad jets that passed the OR are discarded. Similarly, events containing baseline muon candidates, whose relative uncertainty on e/p is larger than 20%, and which were found before the OR, are discarded. This also applies to events containing those potentially cosmic muons which were not removed by the OR.

5.5 Standard Model backgrounds

As already anticipated in Section 1.1.2, there exists a wide variety of SM processes whose cross sections are significantly larger than SUSY signal ones. In order for the analysis to robustly target the desired signal, the accurate modelling of such backgrounds is a fundamental part. The signal region definitions, whose modelling is strictly related to the sensitivity reached by the analysis, need an accurate knowledge of the kinematical properties of both targeted signals and backgrounds. The backgrounds which contribute to the search of direct stop-pair production in final states with jets and E_T^{miss} , with their relative MC samples employed, will be discussed below.

Top pair production: $t\bar{t}$ production is a major background for many third-generation SUSY analyses at the LHC. The dominant top-quark decay is $t \rightarrow bW$ with a Branching Ratio (BR) of $\sim 99.8\%$, which in turn yields two oppositely charged b -jets and W bosons. These will then yield 0-lepton, 1-lepton, and 2-lepton final states, with 45.7%, 43.8%, and 10.5% BRs respectively, giving the name to the fully hadronic, semi-leptonic, and di-leptonic $t\bar{t}$ decays, respectively;

Single top production: the production of one single top is also possible at the LHC. The different decays are usually referred to as *s*-channel, *t*-channel, and *W t* channel, the last one being the most relevant for this analysis since it yields a W ;

Z boson production in association with jets: the production of a Z boson in association with jets is a major background in both 0-lepton plus E_T^{miss} and 2-lepton final states because of the $Z \rightarrow vv$ and the $Z \rightarrow \ell\ell$ decays², with a BR of $\sim 20\%$ and $\sim 10\%$, respectively. Although the hadronic decay of the Z boson ($Z \rightarrow qq$) has the largest BR ($\sim 70\%$), this is not relevant for third-generation SUSY searches, as the multi-jet background dominates. The $Z + \text{jets}$ MC samples are generated categorising³ the events depending on the flavours of the hadrons produced in association with the Z boson:

- b -filtered: containing at least one b -hadron;
- c -filtered: containing at least one c -hadron (no b -hadrons);
- light-filtered: no b - or c -hadrons included;

In this analysis the major contribution to such background comes from the b -filtered sub-sample as the selected events contain b -jets;

W boson production in association with jets: the production of W bosons in association with jets is a relevant background in 1-lepton final states, due to the $W \rightarrow \ell\nu$ decay which has a BR of $\sim 32\%$. The dominant hadronic decay of the W , $W \rightarrow qq'$, produces a multi-jet final state which, again, is irrelevant for this analysis. The $W + \text{jets}$ samples are equally categorised depending on the flavour of the hadrons produced in association with the W boson;

Di-bosons production: albeit the production of pairs of bosons, WW , WZ , and ZZ , can also be a source of background in channels with leptons or jets, depending on the decay mode of each boson;

Top pairs production in association with a vector boson: the cross section of the production of top pairs in association with a vector boson or a Higgs boson is smaller than the other processes considered so far. Nevertheless, such background can be a prominent background for third-generation SUSY analyses. In particular, the top-pair production in association with a Z boson, with the Z boson decaying to neutrinos, $t\bar{t} + Z \rightarrow vv$, does represent an irreducible background for this analysis: it yields a final state with jets and E_T^{miss} which looks identical to the signal searched for. For such reason a data-driven technique is employed, where essentially the top-pair production in association with a photon $t\bar{t}+\gamma$ is used instead. Further details on the method for its estimation will be given in Section 6.2;

Multi-jet: the multi-jet production is the process with the highest cross section among the ones mentioned so far, and even though such events do not contain neither leptons nor E_T^{miss} they could resemble the signal due to either isolated but mis-reconstructed leptons or large measured E_T^{miss} due to detector resolution. Despite the low probability of such

² $\ell = e, \mu, \tau$

³ Using the information at truth level

occurrence, the high rate of such background might generate a non-negligible contribution;

For most of the listed backgrounds, a set of additional sub-samples is generated in order to estimate the theoretical uncertainties associated with the generation of the process. The variations of, re-normalisation, factorisation, CKKW matching scales, different PDF sets or hadronisation models, are included.

5.5.1 MC samples

SM background samples are generated using different MC event generators: the production of $Z + \text{jets}$ and $W + \text{jets}$ events are generated with SHERPA [74] using the NNPDF3.0NNLO [123] PDF set and the UE tune provided by SHERPA itself [74]; $t\bar{t}$ and single-top production are simulated with POWHEG-BOX 2 [137] and interfaced to PYTHIA [73] for PS and hadronisation, with the CT10 [124] PDF set. MG5_AMC@NLO interfaced to PYTHIA for PS and hadronisation is used to generate the $t\bar{t}+V$ and $t\bar{t}+\gamma$ samples at NLO with the NNPDF3.0NLO PDF set. The underlying-event tune used is A14 with the NNPDF2.3L0 PDF set. For the estimation of $t\bar{t}+Z$ via $t\bar{t}+\gamma$, $W/Z + \gamma$ processes are generated with SHERPA [74] using the CT10 PDF set, and finally, the same procedure is used for the generation of di-boson production events.

5.6 Signal Regions optimisation

The experimental signature for all signal topologies described in Section 5.1 is essentially characterised by the presence of multiple jets, two of which are required to have passed the b -tagging selection, a significant amount of missing transverse momentum, and no leptons (electrons or muons).

An initial overview of the five different sets of SRs, Signal Region A (SRA) to Signal Region E (SRE), employed to target each topology and kinematic regime, is given below:

SRA is sensitive to the production of high-mass \tilde{t} pairs with a large $\tilde{t}-\tilde{\chi}_1^0$ mass splitting $\Delta m(\tilde{t}_1, \tilde{\chi}_1^0)$. It is optimised using a signal point defined by: $(m_{\tilde{t}_1}, m_{\tilde{\chi}_1^0}) = (1000, 1)$ GeV signal point;

SRB targets decays involving top squarks with high stop mass but with smaller $\Delta m(\tilde{t}_1, \tilde{\chi}_1^0)$. It is optimised using signal points defined by: $(m_{\tilde{t}_1}, m_{\tilde{\chi}_1^0}) = (700, 400)$ GeV, and $(m_{\tilde{t}_1}, m_{\tilde{\chi}_1^0}) = (600, 300)$ GeV;

SRC is designed for the so-called highly compressed region where, $\Delta m(\tilde{t}_1, \tilde{\chi}_1^0) \sim m_t$ and it employs an ISR to improve sensitivity to such decays. It targets various signal points e.g. $(m_{\tilde{t}_1}, m_{\tilde{\chi}_1^0}) = (500, 327)$, and $(m_{\tilde{t}_1}, m_{\tilde{\chi}_1^0}) = (300, 127)$ GeV;

SRD targets the $\tilde{t}_1 \rightarrow b\tilde{\chi}_1^\pm$ decay, with $m_{\tilde{\chi}_1^\pm} = 2m_{\tilde{\chi}_1^0}$, where no top-quark candidates are reconstructed. It is optimised using signal points defined by: $(m_{\tilde{t}_1}, m_{\tilde{\chi}_1^0}) = (400, 50)$ GeV and $(m_{\tilde{t}_1}, m_{\tilde{\chi}_1^0}) = (700, 100)$ GeV;

SRE is sensitive to highly boosted scenarios that can occur in gluino-mediated stop production and it is optimised using signal points defined by: $(m_{\tilde{g}}, m_{\tilde{t}_1}, m_{\tilde{\chi}_1^0}) = (1700, 400, 395)$ GeV;

5.6.1 Preliminary selection and discriminating key variables

A *pre-selection*, essentially a basic selection of candidate events common to all the SRs, is performed by applying trigger and event-cleaning cuts together with the requirement of a relevant set of physics objects according to the targeted experimental signature. The physics objects, reconstructed as discussed in Section 4.2, are used to build the various variables used to discriminate the SUSY signal from the SM background. The event selection is based on such variables some of which will be described below:

H_T : the scalar sum of the p_T of all signal anti- k_t $R = 0.4$ jets;

$|\Delta\phi(\text{jet}^{0,1}, \mathbf{p}_T^{\text{miss}})|$: the difference in ϕ between the two leading jets (ordered in p_T) and $\mathbf{p}_T^{\text{miss}}$. This variable provides a good rejection of events containing fake E_T^{miss} originating from QCD, hadronic $t\bar{t}$, and detector resolution effects;

m_T^i : the transverse mass (m_T) between the i^{th} jet and the E_T^{miss} in the event

$$m_T^i = \sqrt{2p_T^{\text{jet},i} E_T^{\text{miss}} \left[1 - \cos \Delta\phi(\mathbf{p}_T^{\text{jet},i}, \mathbf{p}_T^{\text{miss}}) \right]},$$

where $p_T^{\text{jet},i}$ is the transverse momentum of the i^{th} jet;

$m_T^{b,\text{min}}$: transverse mass between closest b -jet to E_T^{miss} and E_T^{miss} . This variable provides very good discrimination between signal and semi-leptonic $t\bar{t}$ background;

$m_T^{b,\text{max}}$: transverse mass between farthest b -jet to E_T^{miss} and E_T^{miss} . This variable provides very good discrimination between signal and semi-leptonic $t\bar{t}$ background;

$\Delta R(\mathbf{b}, \mathbf{b})$: the angular separation between the two jets with the highest MV2c10 weight. This variable provides additional discrimination against background where the two jets with highest b -tagging weights originate from a gluon splitting;

$m_{T_2}^{\chi^2}$: the stransverse mass. This is built using direction and magnitude of the $\mathbf{p}_T^{\text{miss}}$ in the transverse plan and the direction of two top-quark candidates reconstructed using a χ^2 method. The minimisation is done in terms of a so-called χ^2 -like penalty function

$$\chi^2 = (m_{\text{cand}} - m_{\text{true}})^2 / m_{\text{true}},$$

where m_{cand} is the candidate mass and m_{true} is set to 80.4 GeV and 173.2 GeV for W candidates and top candidates, respectively. First, W boson candidates are formed by using single or pairs of anti- k_t $R = 0.4$ jets, and then combined with additional b -jets in the

event to construct the top candidates. These, selected by the χ^2 method, are only used for the momenta in $m_{\text{T}2}^{\chi^2}$. The mass hypotheses are set to 173.2 GeV and 0 GeV for the top quarks and the invisible particles, respectively. Further details on $m_{\text{T}2}^{\chi^2}$ can be found at [138, 139].

A summary of the pre-selection cuts is shown in Table 5.2, where three groups of cuts are listed: the first, a $E_{\text{T}}^{\text{miss}}$ cut of 250 GeV, to stay in a region where the trigger is fully efficient, as already mentioned in Section 5.4. The second, a lepton veto⁴, together with a cut on the number of jets (at least four, ordered in $p_{\text{T}} > 80, 80, 40, 40$ GeV), at least one of which must be *b*-tagged, as signal events tend to have more energetic jets than the background, to select hadronic $t\bar{t}$ events. The third, an angular separation between the azimuthal angle of the two highest- p_{T} jets and the $\mathbf{p}_{\text{T}}^{\text{miss}}$, to reject events with mis-measured $E_{\text{T}}^{\text{miss}}$ originating from SM-background decays. In addition, in order to further reject these events, a requirement on $\mathbf{p}_{\text{T}}^{\text{miss,track}}$ to be aligned in ϕ with respect to the $\mathbf{p}_{\text{T}}^{\text{miss}}$ calculated from the calorimeter system, is employed.

Table 5.2: Selection criteria common to all SRs in addition to the event cleaning.

Object	Selection
Trigger	$E_{\text{T}}^{\text{miss}}$
$E_{\text{T}}^{\text{miss}}$	> 250 GeV
N_{lep}	0
anti- k_t $R = 0.4$ jets	≥ 4 , $p_{\text{T}} > 80, 80, 40, 40$ GeV
<i>b</i> -tagged jets	≥ 1
$\left \Delta\phi \left(\text{jet}^{0,1}, \mathbf{p}_{\text{T}}^{\text{miss}} \right) \right $	> 0.4
$E_{\text{T}}^{\text{miss,track}}$	> 30 GeV
$\left \Delta\phi \left(\mathbf{p}_{\text{T}}^{\text{miss}}, \mathbf{p}_{\text{T}}^{\text{miss,track}} \right) \right $	$< \pi/3$

Top quark mass reconstruction In addition to the above-mentioned variables, another set of variables is needed to select SRs targeting the pair production of $\tilde{t}_1 \rightarrow t + \tilde{\chi}_1^0$: the reconstruction of two hadronically decaying top quarks in the event using the jet *re-clustering* algorithm, performed using the anti- k_t algorithm (with a larger distance parameter $R = 1.2$), fed with the calibrated anti- k_t $R = 0.4$ jet collection (further details can be found in [96]). The highest- (second-highest) p_{T} re-clustered jet is chosen to be the first (second) top candidate. The best signal sensitivity is reached by using $R = 1.2$ and $R = 0.8$, for top and W candidates, respectively [4, 140]. The variables used are the masses of the $R = 1.2$ and $R = 0.8$ leading and

⁴ The event must contain exactly 0 baseline electron candidates and 0 baseline muon candidates

sub-leading jets, indicated by $m_{\text{jet},R=1.2}^0$, $m_{\text{jet},R=1.2}^1$, $m_{\text{jet},R=0.8}^0$, $m_{\text{jet},R=0.8}^1$, respectively. Such variables help reduce the SM backgrounds. The $E_{\text{T}}^{\text{miss}}$ value provides the highest discriminating power against SM $t\bar{t}$ production, as it results from the undetected $\tilde{\chi}_1^0$ neutralinos in the signal. In order to further reject $t\bar{t}$ events in which one W boson decays via a charged lepton plus a neutrino two additional requirements are employed. The first is on the transverse mass (m_{T}) calculated from the $E_{\text{T}}^{\text{miss}}$ and the b -tagged jet closest in ϕ to the $\mathbf{p}_{\text{T}}^{\text{miss}}$ direction:

$$m_{\text{T}}^{b,\text{min}} = \sqrt{2 p_{\text{T}}^b E_{\text{T}}^{\text{miss}} \left[1 - \cos \Delta\phi(\mathbf{p}_{\text{T}}^b, \mathbf{p}_{\text{T}}^{\text{miss}}) \right]} > 200 \text{ GeV},$$

which ideally⁵ has an end-point at the top mass value for the $t\bar{t}$ background, as it can be seen in Figure 5.2(b).

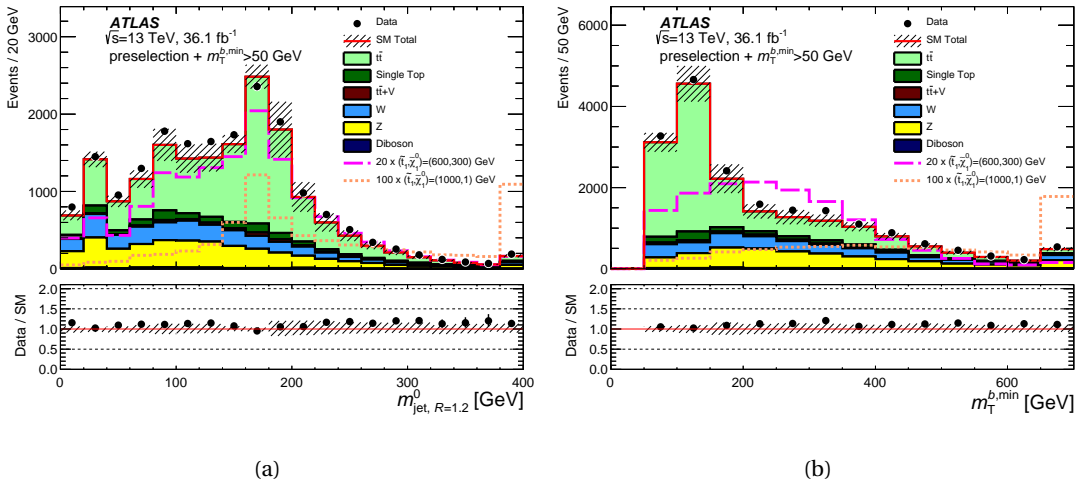


Figure 5.2: Distributions of the discriminating variables discussed in the text: (a) $m_{\text{jet},R=1.2}^0$ and (b) $m_{\text{T}}^{b,\text{min}}$ after the pre-selection and an additional $m_{\text{T}}^{b,\text{min}} > 50$ GeV requirement. The Data/SM plots display the ratio of data events to the total SM prediction. The band around the SM prediction and in the ratio plots illustrates the combination of both statistical and detector-related uncertainties [4].

τ veto An additional requirement is applied to reject those events with semi hadronically decaying τ -lepton candidates that are likely to have been yielded from a $W \rightarrow \tau\nu$ decay. In particular, events are rejected when they contain a non- b -tagged jet, within $|\eta| < 2.5$, with fewer than 4 tracks associated with it ($p_{\text{T}} > 500$ MeV), and when the angular difference, in ϕ , between the jet and $\mathbf{p}_{\text{T}}^{\text{miss}}$ is less than $\pi/5$. The systematic uncertainties associated to the τ veto were studied in a paper - to which the author did not contribute - , produced during a previous version of the analysis carried out during Run-1, and were found to be negligible [136].

⁵ without considering of resolution effects

5.6.2 Optimisation strategy

The optimisation of SRs is a fundamental part of every cut-and-count analysis. The goal is to find the best combination of cuts to remove as many background events as possible while retaining the largest possible fraction of signal events. A set of dedicated discriminating variables is therefore employed in each SR.

In order to represent the discovery significance of the signal model targeted, a Figure of Merit (FoM) is employed. In counting experiments the significance gives an estimate of the probability that an observed event count in a signal region, could have been produced by the sole fluctuations of the backgrounds in that region. In particular the optimisation of the cuts, of which each SR selection is comprised of, is performed by maximising the value of the so-called Z_N formula [141], even though alternative significance definitions can be found on the market [142]. The Z_N formula, implemented in the `RooStats` [143] package within the `ROOT` framework [110], is widely employed in various SUSY searches, and it can be written in a simplistic way as it follows:

$$Z_N = \frac{N_{\text{sig}}}{\sqrt{N_{\text{bkg}} + (N_{\text{bkg}}\sigma_{\text{bkg}})^2}} \quad (5.1)$$

Here, N_{sig} , N_{bkg} , and σ_{bkg} are the signal yields, background yields, and the relative systematic uncertainty on the background, whose value is generally assumed - in a conservative way - a priori. Equation 5.1 essentially gives a general idea of what the discovery significance would be, given a certain number of events in a SR, the Poisson error on the background $\sqrt{N_{\text{bkg}}}$ and the systematic uncertainty $\sigma_{\text{bkg}}N_{\text{bkg}}$ on the background. Furthermore, there are additional criteria, such as the compatibility with more signal models or a more solid background estimation, that must be followed when *freezing*⁶ a SR. The various SR selections will then be defined taking into account the above-mentioned criteria combined with the highest value of Z_N .

A so-called *blinding* procedure is employed to avoid any potential biases that may affect the analysers during the optimisation of the SRs. In particular, the number of events - in the collected data - that fall into a signal-enriched region is hidden until the modelling of the backgrounds falling into a SR has been solidly tested using background-enriched control (Control Regions (CRs)) and validation regions (Validation Regions (VRs)).

Signal Regions A and B

As already anticipated, SRA and SRB are optimised to target $\tilde{t}_1 \rightarrow t + \tilde{\chi}_1^0$ decays, where the stop-neutralino mass splitting is above the top-quark mass. The fully hadronic $t\bar{t}$ decay yields six distinct jets and typically they can be reconstructed as six $R = 0.4$ anti- k_t jets whose transverse shape is circular with a radius equal to the anti- k_t R parameter. Unfortunately though when the two top quarks are produced with enough boost, precisely when their mutual distance is

⁶ Once all the possible combinations have been investigated and a selection has been agreed upon, the SRs cuts are fixed in order to move onto performing extensive background studies

smaller than $2R^7$, the top-quark daughter-jet one-to-one correspondence might no longer be true. For this reason the two top candidates are reconstructed by feeding the anti- k_t clustering algorithm [96] with $R = 0.4$ jets, using re-clustered radius parameters of $R = 0.8$ and $R = 1.2$. Two $R = 1.2$ re-clustered jets are required and the distribution of the leading $R = 1.2$ re-clustered jet mass, for the main backgrounds and the signal, is shown in Figure 5.2(a).

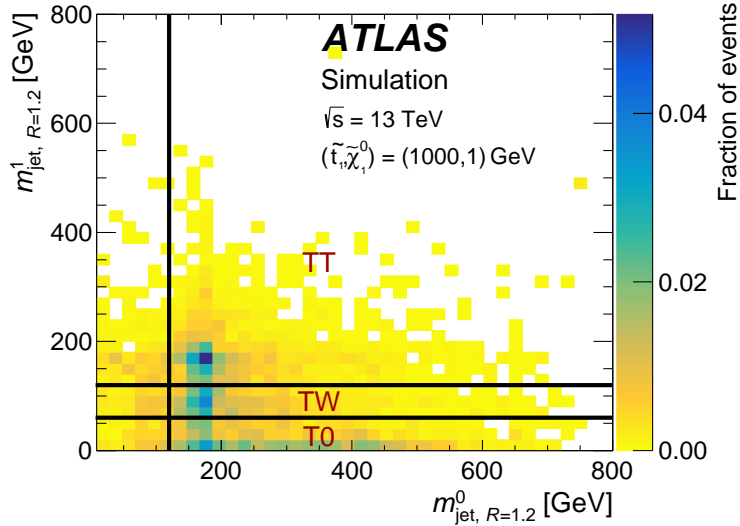


Figure 5.3: 2D distribution of $m_{\text{jet}, R=1.2}^0$ and $m_{\text{jet}, R=1.2}^1$ top candidate masses to illustrate the signal-region categories (TT, TW, and T0) in simulated direct stop-pair production samples with $(m_{\tilde{t}}, m_{\tilde{\chi}_1^0}) = (1000, 1)$ GeV after the pre-selection requirement. The black lines represent the requirements on the re-clustered jet masses [4].

The main discriminating variables are the re-clustered top masses, with $R = 1.2$ and $R = 0.8$, $m_T^{b,\min}$, $\Delta R(b, b)$, and E_T^{miss} . Events are grouped into three categories, as shown in Figure 5.3. The definition of each category is based on the number reconstructed top candidate, as it follows:

TT includes events with two reconstructed top candidates, namely with masses $m_{\text{jet}, R=1.2}^0 > 120$ GeV and $m_{\text{jet}, R=1.2}^1 > 120$ GeV;

TW contains events with one reconstructed leading- p_T top candidate and one reconstructed sub-leading W candidate from the sub-leading $R = 1.2$ re-clustered mass i. e. $m_{\text{jet}, R=1.2}^0 > 120$ GeV and $60 < m_{\text{jet}, R=1.2}^1 < 120$ GeV;

T0 represents events with only a leading top candidate, i. e. where $m_{\text{jet}, R=1.2}^0 > 120$ GeV and $m_{\text{jet}, R=1.2}^1 < 60$ GeV;

For the benchmark point $(m_{\tilde{t}}, m_{\tilde{\chi}_1^0}) = (1000, 1)$ GeV, after the pre-selection requirements, almost the totality of the events (~ 91%) fall into the three categories: TT=38%, TW=22%, and T0=31%. Additionally, a dedicated optimisation on each of such categories, due to differences

⁷ in the η - ϕ space

in kinematics, is performed resulting in the three SRs, SRA-TT, SRA-TW, SRA-T0, defined in Table 5.3.

Table 5.3: Selection criteria for SRA and SRB, in addition to the cuts listed in Table 5.2. SRA and SRB are separated into topological categories based on the number of reconstructed top quarks.

Signal Region	top Categories		
	TT	TW	T0
A	$m_{\text{jet},R=0.8}^0$		$> 60 \text{ GeV}$
	$\Delta R(b,b)$	> 1	-
	$m_{\text{T}2}^{\chi^2}$	$> 400 \text{ GeV}$	$> 400 \text{ GeV}$
	$E_{\text{T}}^{\text{miss}}$	$> 400 \text{ GeV}$	$> 500 \text{ GeV}$
B	$m_{\text{T}}^{b,\text{max}}$		$> 200 \text{ GeV}$
	$\Delta R(b,b)$		> 1.2
A and B	$m_{\text{jet},R=1.2}^0$		$> 120 \text{ GeV}$
	$m_{\text{jet},R=1.2}^1$	$> 120 \text{ GeV}$	$[60, 120] \text{ GeV}$
	$m_{\text{T}}^{b,\text{min}}$		$< 60 \text{ GeV}$
	$N_{b-\text{jet}}$		$> 200 \text{ GeV}$
	$\tau\text{-veto}$		≥ 2
	$ \Delta\phi(\text{jet}^{0,1,2}, \mathbf{p}_{\text{T}}^{\text{miss}}) $		yes
			> 0.4

An additional requirement in SRA is on the stransverse mass ($m_{\text{T}2}^{\chi^2}$), especially powerful in the T0 category, as it assumes high values for signals with high top squark and low neutralino masses. $m_{\text{T}2}^{\chi^2}$ is particularly useful to reconstruct top candidate with lower momenta where the re-clustering was not optimal. Furthermore, in order to maximise the sensitivity to the signal, the top categories are then statistically combined - a logic OR of the three of them is taken - within SRA and SRB.

Figure 5.4 shows the background composition in each of the SRA categories. The main backgrounds are $Z + \text{jets}$ and $t\bar{t}+V$, followed by $t\bar{t}$, $W + \text{jets}$, and single top production. As it will be shown in Section 6.1, dedicated CRs are used for the TT, TW, and T0 categories, in the regions where enough statistic is present. In particular, for the $Z + \text{jets}$ background a set of three 2-lepton CR is used, while to control the $t\bar{t}$ and $W + \text{jets}$ backgrounds two orthogonal sets of 1-lepton control regions are used. As the $t\bar{t} + Z(\rightarrow \nu\nu)$ is an irreducible background, i. e. it utterly resembles the signal searched for, its normalisation is instead obtained by using a 1-lepton-1-photon $t\bar{t}+\gamma$ CR, as it will be shown in 6.2.

For the optimisation of SRB, a similar strategy was adopted. In addition to the $E_{\text{T}}^{\text{miss}}$ and the re-clustered jet masses, the discriminating variables $m_{\text{T}}^{b,\text{min}}$, $m_{\text{T}}^{b,\text{max}}$, and $\Delta R(b,b)$ are em-

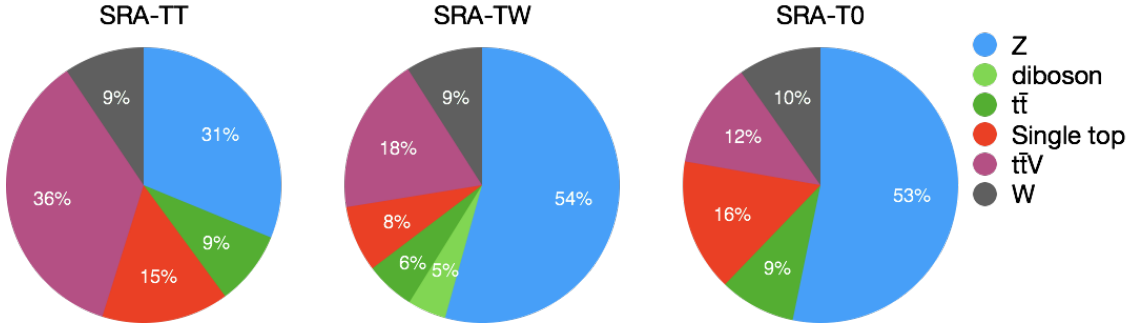


Figure 5.4: Background composition in Signal Region A.

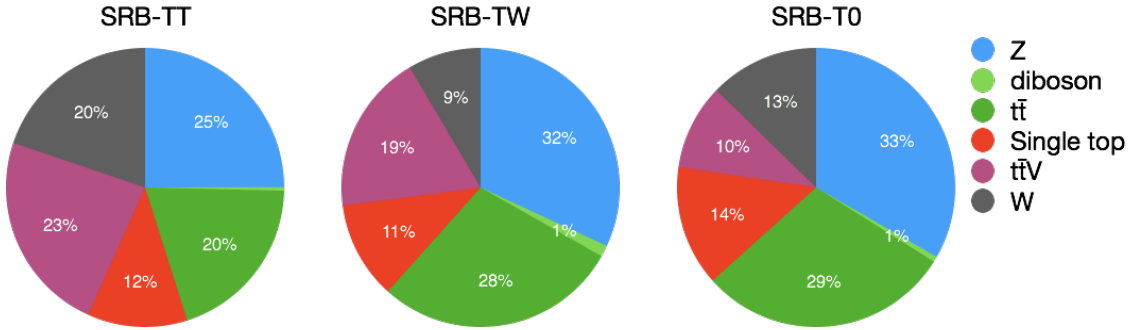


Figure 5.5: Background composition in Signal Region B.

ployed for the optimisation. After the pre-selection requirement, tightened up by the addition of the requirements of at least two b -jets, $m_T^{b,\min} > 200$ GeV, and the tau veto, the fraction of events that fall into the top categories is: TT=14%, TW=20%, T0=35%. The optimal cuts for SRB are also listed in Table 5.3.

Similarly to SRA, Figure 5.5 shows the background composition in each of the SRB categories. The dominant backgrounds in SRB are $Z + \text{jets}$ and $t\bar{t}$, with about equal contributions. As already discussed for SRA, the same CRs are employed to control such dominant backgrounds. The di-boson contributes for less than 1% of the total background therefore no effort will be put in the design of a CR. Furthermore, due to the large E_T^{miss} requirement, contributions from multi-jet background, are expected to be negligible in both SRA and SRB, nonetheless it will be estimated using the so-called *jet smearing* method [144].

Signal Region C

Signal Region C targets a kinematic regime of direct top-squark pair production where the stop-neutralino mass splitting is around the top quark mass. The signature of such decays, when $(m_{\tilde{t}_1}, m_{\tilde{\chi}_1^0}) \sim m_t$, essentially consists of considerably softer jets and low E_T^{miss} . As it can be seen by looking at the background composition of such SR in Figure 5.6, this topology is very similar to a non-resonant $t\bar{t}$ production which makes signal-background separation challenging. Nonetheless the presence of ISR can help exploit kinematical differences between stop decays

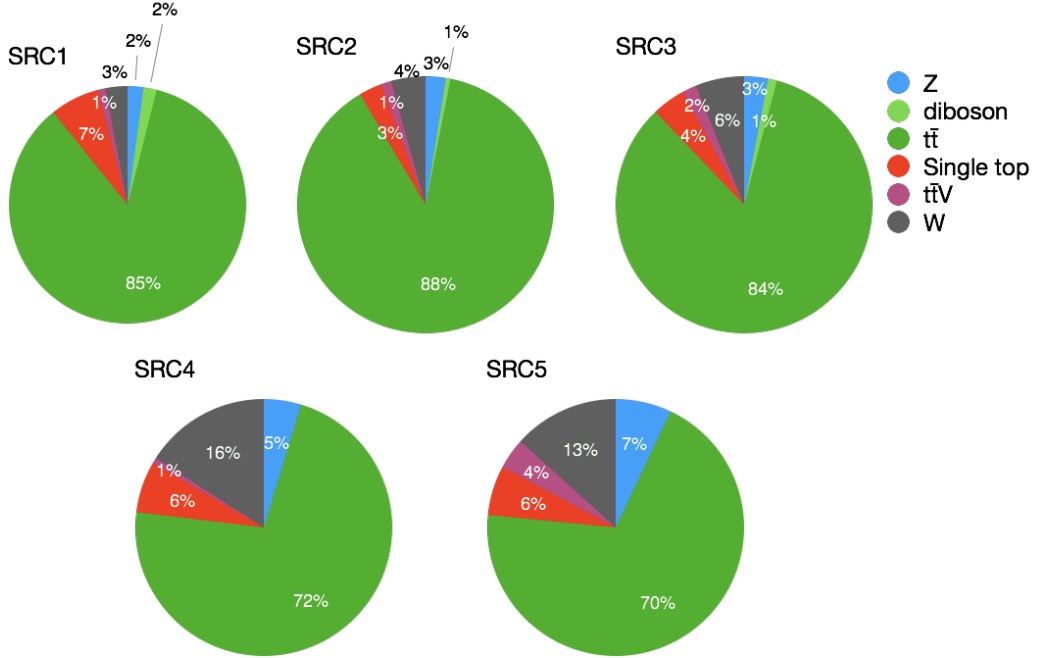


Figure 5.6: Background composition in Signal Region C.

and $t\bar{t}$ production. In particular, when the event is characterised by the presence of a high-momentum ISR - reconstructed as an ISR system formed by multiple jets - the system comprised of the two top-squarks is produced with a boost in the transverse plane.

A new dedicated set of variables can be defined employing the so-called *Recursive Jigsaw Technique (RJR)* of which a brief overview is given. Such technique is used to divide each event into hemispheres: an ISR and a sparticle hemisphere. The latter is comprised of a pair of top-squark candidates both decaying via $t + \tilde{\chi}_1^0$. Objects are grouped together based on their proximity in the lab frame's transverse plane by minimizing the reconstructed transverse masses of the ISR system and sparticle system simultaneously over all choices of object assignment. A dedicated set of kinematic variables is then defined, based on this assignment of objects to either the ISR system or the sparticle system. This method is equivalent to grouping the event objects according to the axis of maximum back-to-back p_T in the event's centre-of-mass (CM) frame where the vectorial sum of all the p_T of the accepted objects is zero. In events with a high- p_T ISR gluon, the axis of maximum back-to-back p_T approximates the direction of the ISR and sparticles' back-to-back recoil. Additional details on such technique can be found in Ref. [145].

The ratio of the E_T^{miss} to the p_T of the ISR system in the CM frame of the entire (ISR plus di-top-squark) system (p_T^{ISR}), defined as R_{ISR} , is proportional to the ratio of the $\tilde{\chi}_1^0$ and \tilde{t} masses and it is defined as it follows [146, 147]:

$$R_{\text{ISR}} \equiv \frac{E_T^{\text{miss}}}{p_T^{\text{ISR}}} \sim \frac{m_{\tilde{\chi}_1^0}}{m_{\tilde{t}}}.$$

Table 5.4: Selection criteria for SRC, in addition to the pre-selection listed in Table 5.2. The SRs are separated into R_{ISR} -based windows.

Selection	SRC1	SRC2	SRC3	SRC4	SRC5
R_{ISR}	0.30–0.40	0.40–0.50	0.50–0.60	0.60–0.70	0.70–0.80
$N_{b\text{-jet}}$				≥ 1	
$N_{b\text{-jet}}^S$				≥ 1	
N_{jet}^S				≥ 5	
$p_{T,b}^{0,S}$				$> 40 \text{ GeV}$	
m_S				$> 300 \text{ GeV}$	
$\Delta\phi(\text{ISR}, \mathbf{p}_T^{\text{miss}})$				> 3.0	
p_T^{ISR}				$> 400 \text{ GeV}$	
$p_T^{4,S}$				$> 50 \text{ GeV}$	

Additionally, the following discriminating key variables are used in the optimisation of SRC:

$N_{b\text{-jet}}^S$: number of b -jets associated with the sparticle hemisphere;

N_{jet}^S : number of jets associated with the sparticle hemisphere;

$p_{T,b}^{0,S}$: p_T of the leading b -jet in the sparticle hemisphere;

$p_T^{4,S}$: p_T of the fourth-leading jet in the sparticle hemisphere;

$\Delta\phi(\text{ISR}, \mathbf{p}_T^{\text{miss}})$: angular separation in ϕ of the ISR and the E_T^{miss} in the CM frame;

p_T^{ISR} : p_T of the ISR system, evaluated in the CM frame;

m_S : transverse mass between the whole sparticle system and E_T^{miss} ;

m_V/m_S : ratio of the transverse mass of the only the visible part of the sparticle system without E_T^{miss} and the whole sparticle system including E_T^{miss} ;

Table 5.4 lists the selection criteria for SRC. Five different non-overlapping R_{ISR} -based sub regions (windows) are employed, each of which targets different signal points, e.g. SRC2 is optimised for $(m_{\tilde{t}}, m_{\tilde{\chi}_1^0}) = (300, 127) \text{ GeV}$; SRC4 is optimised for $(m_{\tilde{t}}, m_{\tilde{\chi}_1^0}) = (500, 327)$. Additionally, a minimum of five jets are required to be assigned to the sparticle hemisphere of the event (N_{jet}^S), and at least one of them ($N_{b\text{-jet}}^S$) must be b -tagged. Requirements on p_T^{ISR} , the highest- p_T b -jet in the sparticle hemisphere ($p_{T,b}^{0,S}$), and the fourth-leading jet in the sparticle hemisphere ($p_T^{4,S}$), are also applied. Furthermore, the transverse mass built from the sparticle system and the E_T^{miss} (m_S), is required to be above 300 GeV. Finally, the angular distance in ϕ between the ISR system and the $\mathbf{p}_T^{\text{miss}}$ in the CM frame is required to be above 3. As with SRA and SRB, the five R_{ISR} windows are statistically combined to improve signal sensitivity.

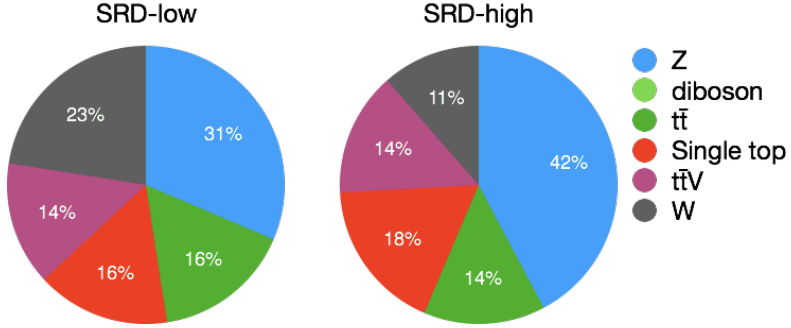


Figure 5.7: Background composition in Signal Region D.

Signal Region D

Signal Region D targets direct top-squark pair production where both top squarks decay via $\tilde{t} \rightarrow b\tilde{\chi}_1^\pm$ and the chargino mass is set to be $m_{\tilde{\chi}_1^\pm} = 2m_{\tilde{\chi}^0}$, therefore a nominal signature of six jets, two of which b -tagged. In this SR no top-quark reconstruction is needed.

SRD is divided into two sub-regions, SRD-low and SRD-high, which are optimised for $m_{\tilde{t}} = 400$ GeV with $m_{\tilde{\chi}^0} = 50$ GeV, and $m_{\tilde{t}} = 700$ GeV with $m_{\tilde{\chi}^0} = 100$ GeV, respectively. As it can be seen in Figure 5.7 the main backgrounds in SRD are $Z + \text{jets}$ and $W + \text{jets}$. The production of $t\bar{t}$, together with single top, and $t\bar{t}+V$ yield around the same number of events.

In this SR, at least five jets are required, two of which must be b -tagged. As previously anticipated, a cut on the distance between the two jets with the highest MV2c10 weights is required to reject event with two b -jets originated from gluon splitting. On top of the discriminating variables already discussed for the other SR, the scalar sum of the transverse momenta of the two jets with the highest MV2c10 weights ($p_T^{0,b} + p_T^{1,b}$) together with the second (p_T^1), fourth (p_T^3), and fifth (p_T^4) jet transverse momenta, are used as discriminating variables to provide further background rejection. Finally, tighter requirements on the leading and sub-leading jet p_T are made for SRD-high. Table 5.5 shows a summary of SRE selection.

Table 5.5: Selection criteria for SRD, in addition to the common pre-selection shown in Table 5.2.

Selection	SRD-low	SRD-high
$ \Delta\phi(\text{jet}^{0,1,2}, \mathbf{p}_T^{\text{miss}}) $		> 0.4
$N_{b-\text{jet}}$		≥ 2
$\Delta R(b, b)$		> 0.8
$p_T^{0,b} + p_T^{1,b}$	> 300 GeV	> 400 GeV
$\tau\text{-veto}$		yes
p_T^1		> 150 GeV
p_T^3	> 100 GeV	> 80 GeV
p_T^4		> 60 GeV
$m_T^{b,\text{min}}$	> 250 GeV	> 350 GeV
$m_T^{b,\text{max}}$	> 300 GeV	> 450 GeV

Signal Region E

Unlike the previous SRs, as mentioned in Section 5.1, SRE is designed for signal models in which top quarks are produced highly boosted. The scenarios targeted by this SR can arise from either direct pair production of high-mass stop quarks, or from the gluino-mediated compressed stop production with a large gluino-stop mass splitting. In this regime, re-clustered jets with $R = 0.8$ are employed for the optimisation of the experimental sensitivity to such highly boosted top quarks. In particular, the signal point used for the optimisation is $m_{\tilde{g}} = 1700$ GeV, $m_{\tilde{t}} = 400$ GeV, and $m_{\tilde{\chi}^0} = 395$ GeV

Figure 5.8 shows the background composition in SRE. The main backgrounds are $Z + \text{jets}$ and $t\bar{t}+V$ followed by single top, $W + \text{jets}$, and $t\bar{t}$ production. A dedicated 2-lepton $Z + \text{jets}$ CR is employed for the normalisation of such background. In this SR, at least two jets out of the four or more required jets must be b -tagged. Additional discrimination is provided by the E_T^{miss} significance: $E_T^{\text{miss}}/\sqrt{H_T}$, where H_T is the scalar sum of the p_T of all the reconstructed $R = 0.4$ jets in the event. The selection criteria for SRE, optimised for $m_{\tilde{g}} = 1700$ GeV, $m_{\tilde{t}} = 400$ GeV, and $m_{\tilde{\chi}^0} = 395$ GeV, are listed in Table 5.6.

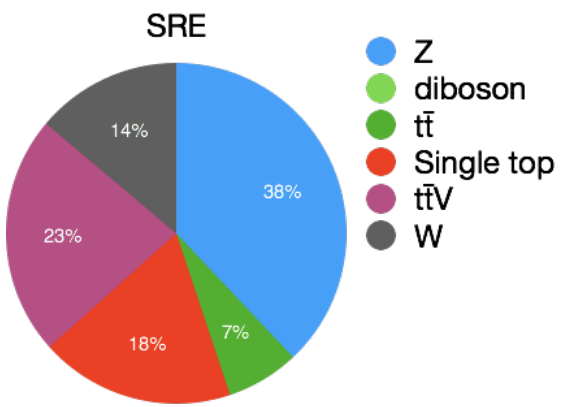


Figure 5.8: Background composition in Signal Region E.

Table 5.6: Selection criteria for SRE in addition to the common pre-selection cuts listed in Table 5.2

Selection	SRE
$ \Delta\phi(\text{jet}^{0,1,2}, \mathbf{p}_T^{\text{miss}}) $	> 0.4
$N_{b\text{-jet}}$	≥ 2
$m_{\text{jet}, R=0.8}^0$	> 120 GeV
$m_{\text{jet}, R=0.8}^1$	> 80 GeV
$m_T^{b,\text{min}}$	> 200 GeV
E_T^{miss}	> 550 GeV
H_T	> 800 GeV
$E_T^{\text{miss}}/\sqrt{H_T}$	> $18\sqrt{\text{GeV}}$

BACKGROUND ESTIMATION

6

The discipline of desire is the background of character.

John Locke

This chapter will describe the background-estimation strategy for the main backgrounds of this analysis, already introduced in Section 5.5, and will give an overview of the systematic uncertainties - both experimental and theoretical - relevant for the analysis carried out. In particular, Section 6.1 provides an overview of the main reducible backgrounds and how to model them; in Section 6.2 the estimation of the irreducible background $t\bar{t}+Z$ will be extensively discussed, as it represents one of the major author's contribution to the presented analysis; finally, the systematic uncertainties will be presented in Section 6.3. The author also contributed to another analysis - the search for Dark Matter produced in association with third-generation quarks - through the estimation of the irreducible background $t\bar{t}+Z$, which, again, was an irreducible background, and this will be presented in Appendix A.

6.1 Nominal background estimation

The implementation of CRs is needed in order to estimate the various background yields in the SRs, without relying solely on the yields that one would obtain simply by applying the SR selection to the MC simulations of a background process. The CRs selections are designed to be orthogonal selections to the SRs. For example, one would ideally design a CR, such that it is fully dominated by the targeted background process, therefore suppressing the signal contamination. This allows to derive a normalisation factor for each relevant background by rescaling the expected MC yield to the observed number of data events in the corresponding CR. The prediction of the yield of a targeted background in SR is then rescaled accordingly. For example, consider the case of one SR and one CR. Ideally, if the CR is 100% pure, the expected background yield in SR can be written as:

$$N_{\text{SR}}^{\text{exp}} = \mu_{\text{MC}} \cdot N_{\text{SR}}^{\text{MC}} \quad \text{with} \quad \mu \equiv \frac{N_{\text{CR}}^{\text{data}}}{N_{\text{CR}}^{\text{MC}}} \quad (6.1)$$

here, μ is the above-mentioned normalisation scale factor. Furthermore, a so-called Transfer Factor (TF) can be defined as the ratio of the MC yields in SR and in CR, allowing the redefinition of the expected background yield in SR, as it follows:

$$N_{\text{SR}}^{\text{exp}} = T_f \cdot N_{\text{CR}}^{\text{data}} \quad \text{with} \quad T_f \equiv \frac{N_{\text{SR}}^{\text{MC}}}{N_{\text{CR}}^{\text{MC}}} \quad (6.2)$$

This procedure allows a data-driven estimation of the expected background yields in SR relying on the MC simulation only for the computation of the TF, and it is widely employed by several SUSY analyses in ATLAS. Furthermore, it also allows to determine $N_{\text{SR}}^{\text{exp}}$ with an uncertainty given by the Poisson error on the $N_{\text{CR}}^{\text{data}}$ and the uncertainty on the CR-to-SR extrapolation. Unfortunately though there are several background processes to be normalised in an independent set of CRs, and these usually suffer contaminations from other background processes. The above-mentioned equations then turn into something less easy to solve, for which statistical tools are needed. In particular, a system of n equations (Equation 6.3), with n number of background processes to control, is employed and needs to be solved to obtain the various normalisation factors:

$$\left\{ \begin{array}{l} N_{\text{CR},1}^{\text{data}} = \mu_1 N_{\text{CR},1}^{\text{MC},1} + \mu_2 N_{\text{CR},1}^{\text{MC},2} + \dots + \mu_n N_{\text{CR},1}^{\text{MC},n} \\ N_{\text{CR},2}^{\text{data}} = \mu_1 N_{\text{CR},2}^{\text{MC},1} + \mu_2 N_{\text{CR},2}^{\text{MC},2} + \dots + \mu_n N_{\text{CR},2}^{\text{MC},n} \\ \dots \\ N_{\text{CR},n}^{\text{data}} = \mu_1 N_{\text{CR},n}^{\text{MC},1} + \mu_2 N_{\text{CR},n}^{\text{MC},2} + \dots + \mu_n N_{\text{CR},n}^{\text{MC},n} \end{array} \right. \quad (6.3)$$

Here, μ_i is the normalisation factor for the i^{th} process; $N_{\text{CR},j}^{\text{MC},i}$ is the number of event, taken only from the MC simulation, that passed the j^{th} CR selection; $N_{\text{CR},k}^{\text{data}}$ is the number of observed event in the k^{th} CR. Such procedure is validated in so-called VRs, designed when the CR are too far - in terms of parameter space - from the SRs. The purpose of VR is to provide a *bridge* between the CRs and the SRs to avoid large extrapolations and avoid any potential biases hidden in the TFs, as shown in Figure 6.1. It is important to stress that VRs are expected not to yield any excess and match the SM predictions within uncertainties. The data-MC agreement in VRs represents a green light toward the unblinding of the blinded SRs.

For the estimation of the major sources of reducible background 1-lepton and 2-lepton CRs are employed. In particular, a 2-lepton CR is used for the estimation of the $Z + \text{jets}$ background (CRZ) and a 1-lepton CR is employed for the estimation of $t\bar{t}$ (CRT), single top (CRST), and $W + \text{jets}$ (CRW) backgrounds. Additionally, a dedicated set of variable is employed:

N_ℓ : number of leptons in the event;

p_T^ℓ : transverse momentum of the leading lepton;

$m_{\ell\ell}$: invariant mass of the Same Flavour Opposite Sign (SFOS) lepton pair in the event;

$m_T(\ell, E_T^{\text{miss}})$: transverse mass calculated from the E_T^{miss} and the transverse momentum of the lepton;

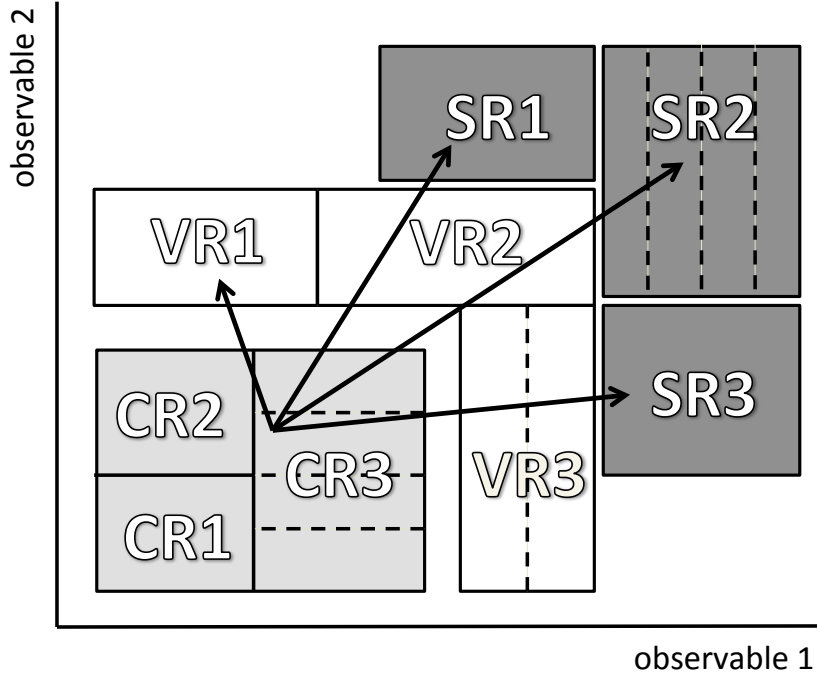


Figure 6.1: A schematic view of an analysis strategy with multiple CRs, VRs, and SRs using two observables. The CR-to-SR extrapolation is verified by employing VRs that lie in the extrapolation phase space (taken from [148]).

$E_T^{\text{miss}'}$: the transverse momenta of the selected leptons are added to the $\mathbf{p}_T^{\text{miss}}$, e.g. to mimic the $Z \rightarrow v\bar{v}$ decays in the SRs, forming the quantity $E_T^{\text{miss}'}$. Essentially, this is a corrected version of E_T^{miss} to treat the leptons as neutrinos. The *prime* notation is used for all the variables that depend on $E_T^{\text{miss}'}$.

6.1.1 Control regions

The background estimation strategy is based on five independent CRs to control $Z + \text{jets}$, $t\bar{t}$, single top, $W + \text{jets}$, and $t\bar{t}+Z$. Where enough statistics is available CRs are designed to estimate backgrounds in different kinematic regions of the SRs. A description of the nominal background estimation strategy is given below, except for the estimation of the irreducible background $t\bar{t}+Z$, which will be discussed in Section 6.2 as a different technique is employed. The remaining backgrounds such as di-bosons and multi-jet are estimated directly using the yields obtained from MC simulations. A detailed description of all the selections employed for the estimation of the above-mentioned backgrounds can be found in Appendix B.

$Z + \text{jets CR (CRZ)}$ The estimation of the $Z \rightarrow v\bar{v}$ background is performed via the design of 2-lepton $Z \rightarrow \ell\ell$ CR. Although the branching fraction of the $Z \rightarrow \ell\ell$ is smaller than $Z \rightarrow v\bar{v}$,

a purer CR can be obtained. As all the SRs (exception made for SRD) have requirements on the E_T^{miss} selection, jet multiplicity, and b -tagged jets, in order to ensure as little CR-to-SR extrapolation as possible, the same kinematic cuts are applied in CRZ. SRA and SRB share a set of two Z CRs: one is shared by the TT and TW categories due to statistical limitations and one is dedicated to the T0 category (CRZAB-TT-TW, CRZAB-T0). A common Z CR is used for SRDs (CRZD). Finally, a Z CR with higher H_T requirements is used for SRE. The CRs are defined by using events passing a single-lepton trigger, and in addition requiring a cut on 2 SFOS leptons is applied. To reduce the top contamination, an upper cut at $E_T^{\text{miss}} < 50$ GeV, and a lower cut at 100 GeV are applied. Furthermore, a Z -mass window cut on the invariant mass of the leptons pair is applied, to reduce other backgrounds contamination. A detailed CR definition is given in Table B.1

$t\bar{t}$ CR (CRT) As already mentioned, these CRs are all defined by using events required to pass a E_T^{miss} trigger. In addition, in order to emulate the hadronic τ decays in the SRs the lepton is treated as a non- b -tagged jet in the computation of all jet-related variables. Similarly to CRZ, CRT is then further divided to address the various SRs;

$W + \text{jets CR (CRW)}$ CRW, very similar to CRT, also employs a E_T^{miss} trigger, but here 1 b -jet only is required. In addition, a looser and inverted cut on $m_{\text{jet},R=1.2}^0$, together with a requirement $\Delta R(b_{0,1}, \ell)_{\min}$, defined as the minimum ΔR between the two jets with the highest b -tag weight and the selected lepton, ensures that CRW is orthogonal with CRT;

Single top CR (CRST) In CRST, also similar to CRT and CRW, two b -jets are required. Furthermore, the requirement on the ΔR of the two leading-weight b -jets is necessary to reject a large part of the remaining $t\bar{t}$ background.

6.1.2 Validation regions

To validate the estimation of the various backgrounds, VRs are employed where possible. In particular, the following VRs are defined:

$Z + \text{jets VR (VRZ)}$ 0-lepton VRs are designed to validate the background estimate for $Z + \text{jets}$ in the SRs. Similarly to the strategy used in CR, dedicated sets of VRs are employed: VRZAB, VRZD, VRZE. No VRZ is designed for SRC due to the negligible contribution of the Z background in this region. In practice, to ensure orthogonality to the SRs, the requirement on one or more of the following variables is inverted: $\Delta R(b, b)$, $m_{\text{jet},R=1.2}^0$, $m_{\text{jet},R=0.8}^0$. A detailed list of the VRZ selections, after the common pre-selection shown in Table 5.2, is shown in Table B.4.

$t\bar{t}$ VR (VRTT) Following the same strategy discussed so far, in order to validate the $t\bar{t}$ background, 0-lepton VRs sharing the same common pre-selection close to the SRA and SRB definitions are designed for each of the top categories: VRTA-TT, VRTA-TW, VRTA-T0, VRTB-TT, VRTB-TW, VRTB-T0. To ensure orthogonality with the SRs the $m_T^{b,\min}$ requirement is inverted in all VRs. In particular, for the definition of VRTA, the SRA requirements

are unchanged except for $m_{T2}^{\chi^2}$ which is not being applied, $100 < m_T^{b,\min} < 200$ GeV, and the E_T^{miss} requirement being loosened by 100 GeV. The requirements for VRTB are the same as in the SRs except for $m_T^{b,\min}$, being changed to $100 < m_T^{b,\min} < 200$ GeV for VRTB-TT, $140 < m_T^{b,\min} < 200$ GeV for VRTB-TW, and $160 < m_T^{b,\min} < 200$ GeV for VRTB-T0. The VRTC keeps the same requirements as Signal Region C except for the looser requirements of $m_S > 100$ GeV, $p_T^{4,S} > 40$ GeV and $N_{\text{jet}}^S > 4$. The $\Delta\phi(\text{ISR}, \mathbf{p}_T^{\text{miss}})$ requirement is inverted and $m_V/m_S < 0.6$, where m_V is the transverse mass defined by the visible objects of the sparticle system and the E_T^{miss} , is applied in addition to the existing selection. The VR VRTD, targeting SRD, is formed by applying the following requirements: $100 < m_T^{b,\min} < 200$ GeV, $p_T^{0,b} + p_T^{1,b} > 300$ GeV, $p_T^3 > 80$ GeV, and $m_T^{b,\max} > 300$ GeV. All other requirements are applied exactly as in SRD-low except for the requirement on p_T^4 which is not applied. Finally, VRTE, dedicated to SRE, ensures a minimum extrapolation as it applies the same requirements on the number of b -jets, $m_{\text{jet},R=0.8}^0$, and $m_{\text{jet},R=0.8}^1$, and inverts the $m_T^{b,\min}$ requirement to $100 < m_T^{b,\min} < 200$ GeV;

$W + \text{jets VR (VRW)}$ For the validation of the $W + \text{jets}$ background a unique 1-lepton 1- b -jet VR is used to test such background in all the SRs, with the only differences with respect to CRW being, $\Delta R(b_{0,1}, \ell)_{\min}$, which is greater than 1.8 in the VR plus two additional requirements, namely $m_T^{b,\min} > 150$ GeV and $m_{\text{jet},R=1.2}^0 < 70$ GeV which are included in the definition of VRW. Further details

Ultimately, in order to determine the normalisations of the SM backgrounds for Z , $t\bar{t}$, W , single top, $t\bar{t}+Z$, and their estimates, in each SRs, the observed numbers of events in the various CRs are included in a binned profile likelihood fit, which will be discussed in Section 7.1. A simultaneous fit, to best match the observed data in each CR, taking into account all the contributions from the various backgrounds, is performed to determine the SM background normalisation factors.

6.2 Estimation of the irreducible background

The production of top pairs in association with a vector boson ($t\bar{t}+V$) is the second most important background in most SRs. Precisely, such background is completely dominated by $t\bar{t}+Z(\rightarrow \nu\nu)$, as the $t\bar{t}+W(\rightarrow \ell\nu)$ contribution in SR is negligible due to the presence of the lepton in the final state. As already anticipated in various parts of this work, $t\bar{t}+Z(\rightarrow \nu\nu)$ yields a final state with kinematic properties identical to the signal searched for, namely two top quarks (six jets, if both tops are fully reconstructed) and E_T^{miss} from the neutrinos coming from the Z decay. Unfortunately, as of today, although the ATLAS collaboration has allocated some effort on this, no SM measurement of such process has been published, especially due to the presence of large E_T^{miss} making the isolation of such signature quite difficult.

A data-driven technique, similar to the one adopted in [149], is employed to estimate its background. The normalisation of $t\bar{t}+Z$ in SR is estimated by designing a 1-lepton-1-photon

$t\bar{t}+\gamma$ control region (CRTTGamma). Despite the differences in cross-section ($\sigma_{t\bar{t}+Z}^{\text{aMC@NLO}} \sim 150$ pb, $\sigma_{t\bar{t}+\gamma}^{\text{aMC@NLO}} \sim 215$ pb), the validity of the technique is supported by the similarities of the $t\bar{t}+Z$ and $t\bar{t}+\gamma$ Feynman diagrams, as shown in Figure 6.2. This CR is designed to minimise the differences between the two processes and keep the theoretical uncertainties from the extrapolation of the γ to the Z low.

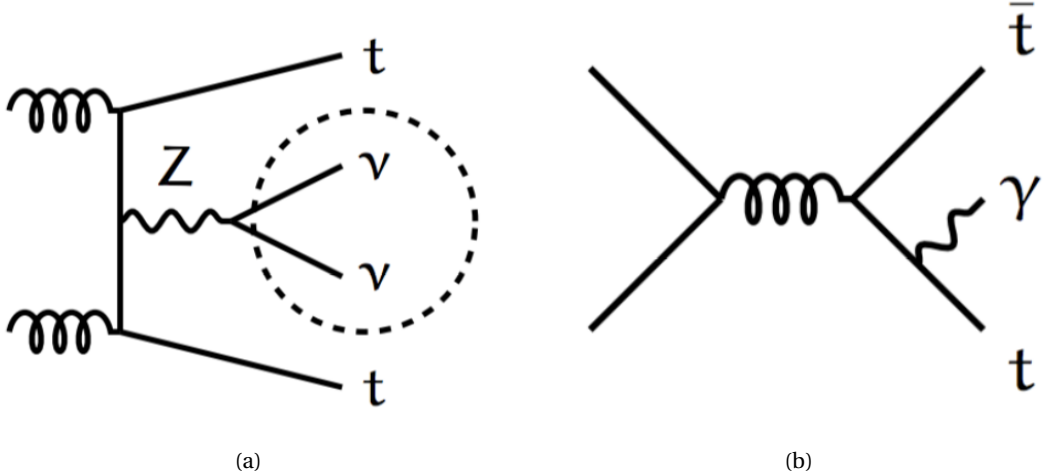


Figure 6.2: Diagrams of the production of top-antitop pairs associated with a Z boson (a) and a photon (b).

The strategy is based on the addition of the transverse momentum of the γ in the event (p_T^γ) to the computation of the E_T^{miss} to mimic the neutrinos from the Z decay. In this context, the γ p_T is approximately the missing transverse momentum, $p_T^\gamma \sim E_T^{\text{miss}}$.

Events in this CR are required to pass the same lepton triggers and lepton- p_T requirements required in all the other 1-lepton CRs. In addition, an isolated photon with $p_T^\gamma > 150$ GeV is required. Figure 6.3 shows the truth-level p_T distributions of the Z and the γ . The former is taken from the $t\bar{t}+Z$ MC sample and obtained by requiring a basic SR-like selection comprising at least four jets, two of which b -tagged, zero baseline and signal leptons, and a lower cut of 150 GeV on the p_T of the Z . The latter is taken from the $t\bar{t}+\gamma$ MC sample and obtained by requiring a basic CR-like selection including at least four jets, two of which b -tagged, 1 lepton and 1 photon, and a lower cut of 150 GeV on the p_T of the γ . The agreement found in Figure 6.3 ensures the applicability of the method and, more importantly, that the shape of the p_T distributions of the two bosons, taken from the two MC samples, is essentially the same in the whole kinematic range. This, in turn, ensures that the extrapolation of the $t\bar{t}+Z$ yield in SR from the CR (p_T^γ to SR (E_T^{miss})) will be safe. In addition, similarly to what is done for the Z CRs, the photon p_T is used for the estimation of E_T^{miss} -related variables. Finally, In order to avoid double-counting of $t\bar{t}$ simulated events where a hard photon is emitted, the MCTruthClassifier [150] tool is employed to perform a truth-level selection of photons irradiated by a top quark. Table 6.1 shows the detailed selection applied.

The estimation of the $t\bar{t}+Z$ yields in SR is based on an approximation of what was already

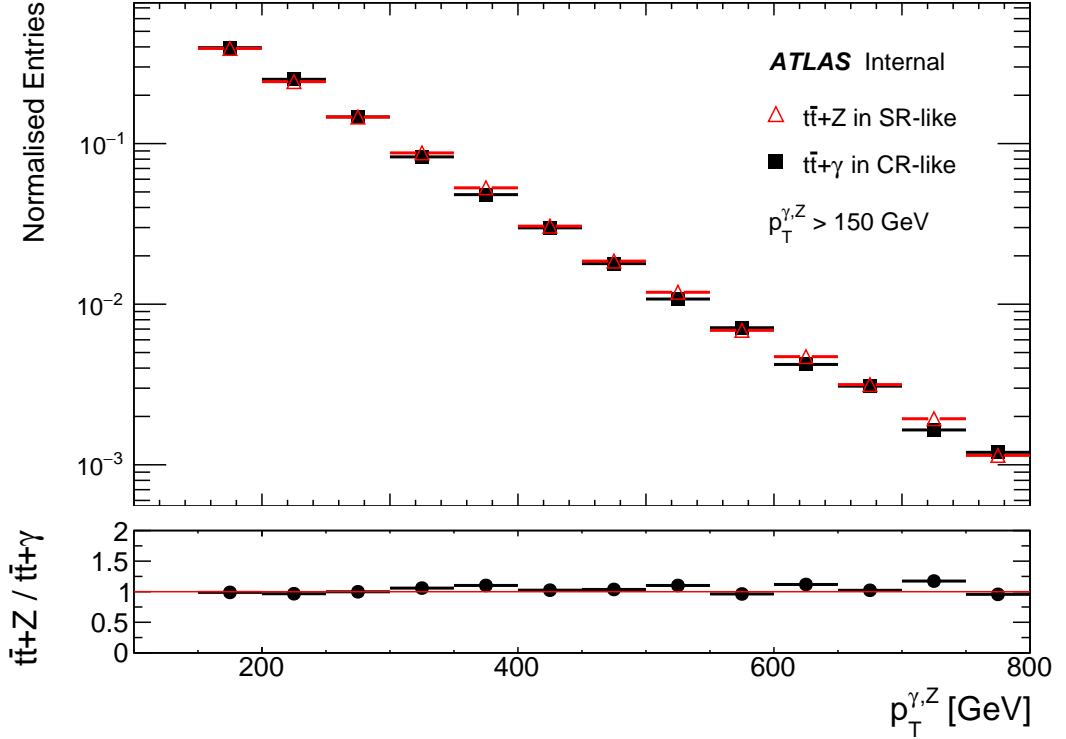


Figure 6.3: Ratio plot of the p_T of the Z and γ bosons at truth level obtained by requiring CR-like and SR-like selections as described in the text.

shown in Equations 6.2 and 6.3:

$$N_{t\bar{t}+Z,\text{SR}}^{\text{exp}} \sim N_{t\bar{t}+\gamma,\text{CR}}^{\text{obs}} \cdot \frac{N_{t\bar{t}+Z,\text{SR}}^{\text{MC}}}{N_{t\bar{t}+\gamma,\text{CR}}^{\text{MC}}} \quad \text{with} \quad T_f \equiv \frac{N_{t\bar{t}+Z,\text{SR}}^{\text{MC}}}{N_{t\bar{t}+\gamma,\text{CR}}^{\text{MC}}} \quad (6.4)$$

where, $N_{t\bar{t}+Z,\text{SR}}^{\text{exp}}$ is the expected $t\bar{t}+Z$ yields in SR, $N_{t\bar{t}+\gamma,\text{CR}}^{\text{obs}}$ is the observed number of $t\bar{t}+\gamma$ events in $t\bar{t}+\gamma$ CR, $N_{t\bar{t}+Z,\text{SR}}^{\text{MC}}$ is the number of $t\bar{t}+Z$ events falling into the SRs, and $N_{t\bar{t}+\gamma,\text{CR}}^{\text{MC}}$ is the number of $t\bar{t}+\gamma$ events in $t\bar{t}+\gamma$ CR taken from the MC simulation. As previously mentioned, if the CR were 100% pure (no contamination of other background processes) Equation 6.4 would not be approximated, but exact.

Table 6.2 shows the breakdown of the various processes entering into the CRTTGamma selection shown in Table 6.1. The purity¹ reached is 87% and a normalisation factor of 1.29 is obtained.

Additionally the agreement between the observed data and the MC predictions was checked in the E_T^{miss} and $m_T(\ell, E_T^{\text{miss}})$ distributions, shown in Figure 6.4, to rule out any potential fake lepton that would show up at low values of $m_T(\ell, E_T^{\text{miss}})$. The agreement found in the low $m_T(\ell, E_T^{\text{miss}})$ region is a reasonable indication of no significant fake contributions.

Figures 6.5 and 6.6 show a selection of the distributions of those variables on which an

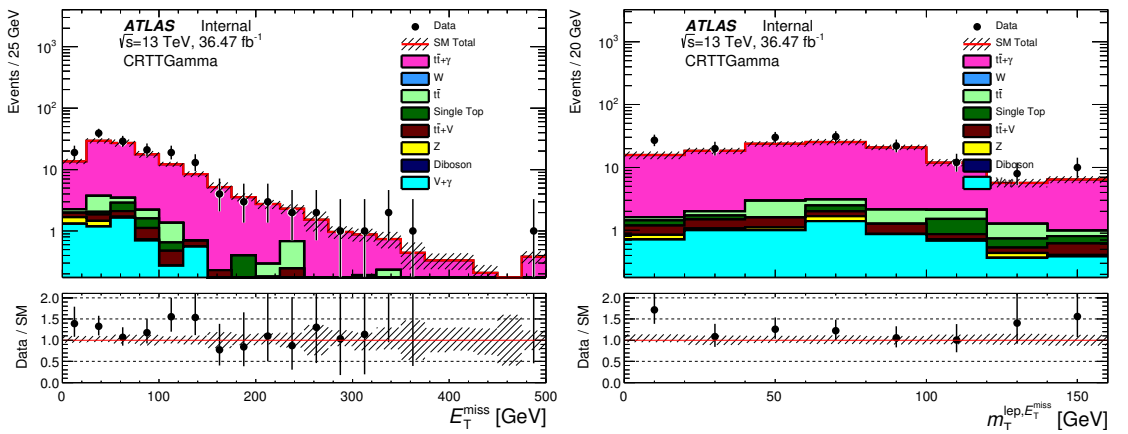
¹ Defined as the Number of $t\bar{t}+\gamma$ events divided by the total number of simulated events.

Table 6.1: Selection criteria for CRTTGamma.

Selection	CRTTGamma
Trigger	lepton
N_ℓ	1
Lepton p_T	28 GeV
N_γ	1
γp_T	> 150 GeV
N_{jets}	≥ 4
Jet p_T	(80, 80, 40, 40) GeV
$N_{b-\text{jets}}$	≥ 2

Table 6.2: Background composition of $t\bar{t}+\gamma$ CR. Pre-fit yields, statistical and detector systematic uncertainties shown. $\mu_{t\bar{t}+\gamma}$ is the background normalisation factor obtained from the fit that will be discussed in Section 7.1.

Process	Yield
$t\bar{t}+\gamma$	111.76 ± 1.45
$V+\gamma$	6.29 ± 0.63
$t\bar{t}$	5.14 ± 1.20
$t\bar{t}+V$	2.34 ± 0.25
single Top	2.07 ± 0.80
Z	0.66 ± 0.17
W	0.04 ± 0.02
Total MC	128.29 ± 2.17
Data	161.00 ± 12.69
CRTTGamma (87%)	
$\mu_{t\bar{t}+\gamma}$	1.29 ± 0.12

Figure 6.4: Distributions of the E_T^{miss} and $m_T(\ell, E_T^{\text{miss}})$ for fake lepton checks. Agreement at low $m_T(\ell, E_T^{\text{miss}})$ is an indication of no significant contributions from fake leptons. The ratio between data and MC is given in the bottom panel. The hashed area in both the top and lower panel represents the uncertainty due to MC statistics.

extrapolation from CR to SR is needed. In particular, the distributions of p_T^γ , $m_{T2}^{x^2}$, $m_T^{b,\min}$ (corrected with the photon p_T), $m_T^{b,\max}$ (corrected with the photon p_T), H_T , and $\Delta R(b, b)$, are shown in Figures 6.5 (a), (b), (c), (d), (e), and (f), respectively. Additionally, the distributions of all the jet masses, $m_{\text{jet},R=1.2}^0$, $m_{\text{jet},R=1.2}^1$, $m_{\text{jet},R=0.8}^0$, $m_{\text{jet},R=0.8}^1$ are shown in Figure 6.6 (a), (b), (c), and (d), as also on these an extrapolation is needed.

Finally, a 0-lepton $t\bar{t}+\gamma$ VR was also considered but it was found to have a too low $t\bar{t}+\gamma$ contribution, with $\gamma + \text{jets}$ being the main contaminant and it was therefore dropped. Nevertheless, the use of the same kinematic selection in CR and SR, together with the good data/MC agreement found in the main distributions, gives confidence in the accuracy of the method.

6.3 Systematic uncertainties

An overview of the sources of systematic uncertainty, relevant for the analysis presented in this thesis, will be presented in this section. In particular, as both experimental effects and theoretical modelling of signal and background processes produce sources of uncertainty, these will be discussed in two separate paragraphs.

6.3.1 Experimental uncertainties

For each of the reconstructed physics objects an experimental uncertainty is assigned. These uncertainties are estimated by dedicated calibrations of each physics object, such as electrons, muons, jets, b -jets, and E_T^{miss} . The systematic uncertainties are implemented within the MC samples which are modified by varying the relevant quantities. A list of experimental uncertainties is presented here:

JES and Jet Energy Resolution (JER): these uncertainties arise from the measured momentum of the jets, which need to be calibrated to the right energy scale [151] as described in Section 4.2. Ref. [151] provides an extensive presentation of a set of three uncorrelated variations that is employed to evaluate the impact of JES uncertainty, while the JER uncertainty is estimated by varying a single parameter [152]; these uncertainties are dominant in this analysis given the high jet multiplicity requirement of the selections.

b -tagging: because of the two b -tagged jets requirement in both signal and the majority of background estimations, the b -tagging is a main source of uncertainty. Scale factor uncertainties in b -tagging depend on the kinematics of the jet and also on the jet flavour. Three kinds of uncertainties on the b -jet weight, called *nominal*, *up*, and *down*, are calculated, propagating the estimated uncertainties to the scale factors for b -jets. Additionally, the variations are applied separately to b -jets, c -jets and light jets, with flavour determined from the truth information in the simulated MC samples;

E_T^{miss} Soft-term Resolution and Scale: scale and resolution uncertainties of individual objects need to be propagated to E_T^{miss} . Specific systematic uncertainties on the scale and resolu-

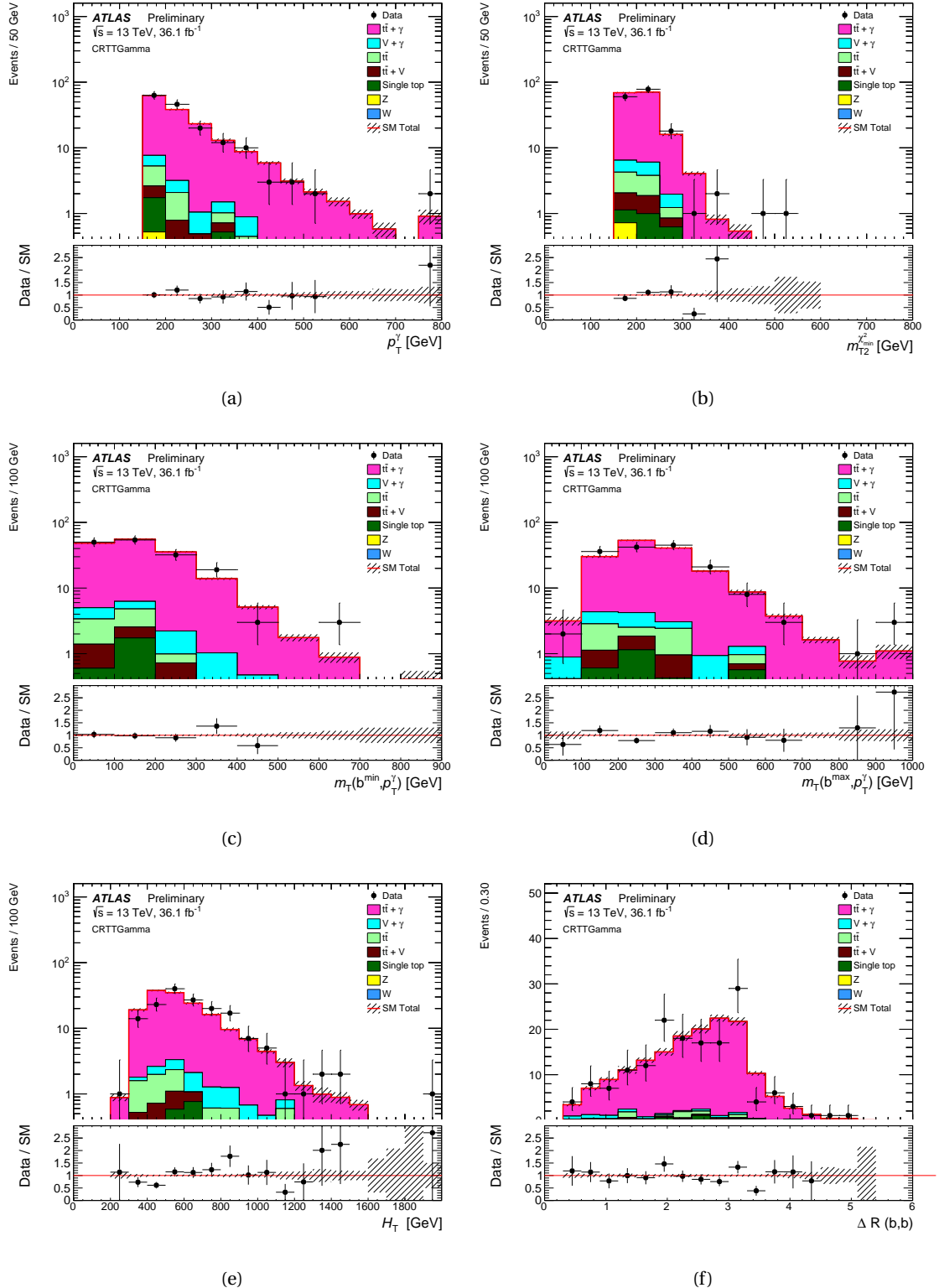


Figure 6.5: Data/MC distributions of the photon p_T (a), $m_{\chi_2}^2$ (b), $m_T^{b,\text{min}}$ (c), $m_T^{b,\text{max}}$ (d), H_T (e), $\Delta R(b,b)$ (f). The ratio between data and MC is given in the bottom panel. The hashed area in both the top and lower panel represents the uncertainty due to MC statistics. The rightmost bin includes overflow events.

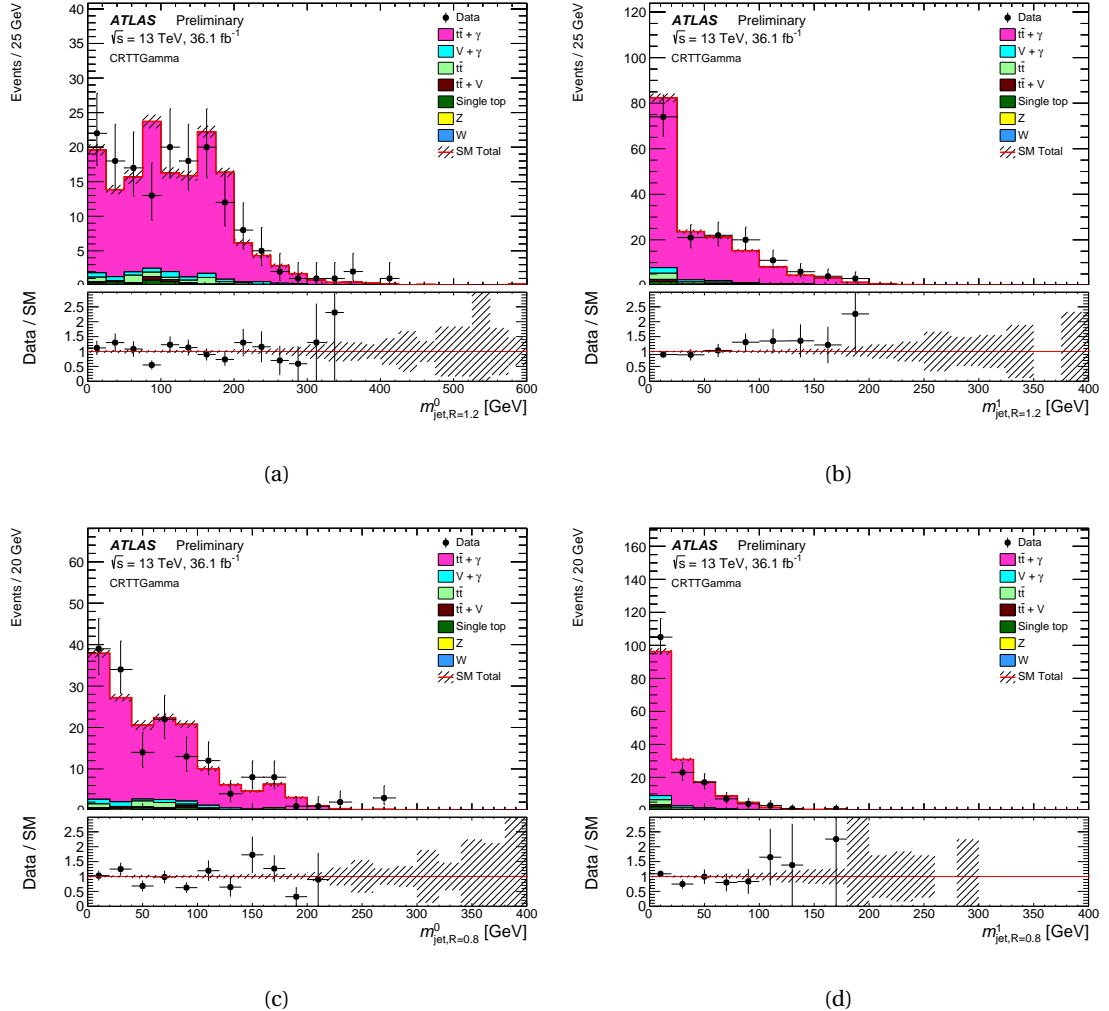


Figure 6.6: Data/MC distributions of the re-clustered jet masses, $m_{\text{jet},R=1.2}^0$ (a), $m_{\text{jet},R=1.2}^1$ (b), $m_{\text{jet},R=0.8}^0$ (c), $m_{\text{jet},R=0.8}^1$ (d). The ratio between data and MC is given in the bottom panel. The hashed area in both the top and lower panel represents the uncertainty due to MC statistics. The rightmost bin includes overflow events.

tion of the E_T^{miss} soft term are derived through *in-situ* methods using $Z \rightarrow \mu\mu$ events [114] and considered in this analysis;

Jet vertex Tagger (JVT): p_T -dependent JVT Scale Factors (SFs) are modified within the uncertainties, obtained from dedicated measurements in $Z \rightarrow \mu\mu$ events [101];

Lepton efficiencies: lepton reconstruction and identification efficiencies have contributions to the backgrounds. For electrons, the uncertainties originate from the e/gamma resolution and scale and from the electron reconstruction efficiency. Similarly, for muons the uncertainties originate from the muon resolution and reconstruction efficiency, the isolation and the momentum scale;

Pileup: an event-level weight is employed to correct the distribution of the pileup parameter μ in the MC samples, to be matched to the one observed in the 2015 + 2016 dataset. Nevertheless, if the selections of the analysis are not sensitive to pileup the impact of the

reweighting should be negligible. The uncertainty due to pileup reweighting is treated as a two-sided variation in the event weights;

Trigger: trigger efficiency SFs are also a source of uncertainty, and they are therefore implemented using results taken from dedicated measurements [50];

Luminosity: lastly a 3.2% uncertainty on the luminosity of the 2015+2016 dataset is added [153].

Ultimately, Table 6.3 shows the main sources of experimental systematic uncertainty in the SM background estimates for SRA and SRB: the main sources are the JER and the JES, which reaches the 17% in SRC5; the b -tagging efficiency, which is nowhere larger than 9%; the E_T^{miss} soft term, mostly significant in SRC5 where it reaches 15%; the pile-up modelling which reaches the 14% in SRC5. The jet- and lepton-related uncertainties are propagated to the calculation of the E_T^{miss} , and additional uncertainties in the energy and resolution of the soft term are also included [154]. Finally, lepton reconstruction and identification uncertainties are also considered but have a small impact [4]. Equally, Table 6.4 show the uncertainties for SRC, SRD, and SRE.

Table 6.3: Systematic uncertainties, larger than 1% for at least one SR, for SRA and SRB in percent relative to the total background estimates. $\mu_{t\bar{t}+Z}$, $\mu_{t\bar{t}}$, μ_Z , μ_W , and $\mu_{\text{single top}}$ refer to the uncertainties due to the normalisation from a CR for a given SR and background. The theory uncertainties are the total uncertainties for a given background.

	SRA-TT	SRA-TW	SRA-T0	SRB-TT	SRB-TW	SRB-T0
Total syst. unc.	24	23	15	19	14	15
$t\bar{t}$ theory	10	6	3	10	11	12
$t\bar{t}+V$ theory	2	<1	<1	1	<1	<1
Z theory	1	3	2	<1	1	<1
Single top theory	6	3	5	3	4	5
Di-boson theory	<1	2	<1	<1	<1	<1
$\mu_{t\bar{t}}$	<1	<1	<1	2	2	1
$\mu_{t\bar{t}+Z}$	6	3	2	4	3	2
μ_Z	6	10	7	5	6	4
μ_W	1	1	1	2	1	2
$\mu_{\text{single top}}$	5	3	5	4	4	5
JER	10	12	4	3	4	3
JES	4	7	1	7	4	<1
b -tagging	1	3	2	5	4	4
E_T^{miss} soft term	2	2	<1	1	<1	<1
Multi-jet estimate	1	<1	<1	2	2	<1
Pileup	10	5	5	8	1	3

Table 6.4: Systematic uncertainties, larger than 1% for at least one SR, for SRC, SRD, and SRE in percent relative to the total background estimates. $\mu_{t\bar{t}+Z}$, $\mu_{t\bar{t}}$, μ_Z , μ_W , and $\mu_{\text{single top}}$ refer to the uncertainties due to the normalisation from a CR for a given SR and background. The theory uncertainties are the total uncertainties for a given background.

	SRC1	SRC2	SRC3	SRC4	SRC5	SRD-low	SRD-high	SRE
Total syst. unc.	31	18	18	16	80	25	18	22
$t\bar{t}$ theory	27	11	14	11	71	12	10	11
$t\bar{t}+V$ theory	<1	<1	<1	<1	<1	<1	<1	1
Z theory	<1	<1	<1	<1	<1	<1	<1	2
W theory	<1	<1	1	3	2	<1	<1	1
Single top theory	3	2	2	3	<1	5	6	12
$\mu_{t\bar{t}}$	4	6	6	5	5	1	1	<1
$\mu_{t\bar{t}+Z}$	<1	<1	<1	<1	<1	2	2	4
μ_Z	<1	<1	<1	<1	<1	4	5	5
μ_W	<1	<1	1	3	3	3	1	2
$\mu_{\text{single top}}$	3	2	2	3	<1	5	6	6
JER	4	10	6	5	10	3	6	4
JES	4	5	2	2	17	8	4	5
b -tagging	2	2	<1	2	4	9	7	<1
E_T^{miss} soft term	1	3	2	3	15	4	3	2
Multi-jet estimate	12	3	<1	<1	<1	2	2	<1
Pileup	<1	1	<1	2	14	9	<1	2

6.3.2 Theory uncertainties

The theoretical uncertainty in each signal region is evaluated by considering variations with respect to the nominal settings and choices for the event generation. For each of the considered variations, the systematic uncertainty is estimated as an uncertainty on the TF, previously defined in Equation 6.2. In particular, the following recipe is followed for the main backgrounds;

$V + \text{jets}$: the uncertainties on the production of W/Z bosons plus jets are estimated by varying the parameters within the Sherpa MC samples related to the factorisation, renormalisation, resummation and CKKW matching scales. The theory uncertainty on the normalisation of the W/Z boson production is then obtained by comparing the MC predictions on the TF. The uncertainty on the transfer factor is computed with the following equation:

$$\Delta_X = \frac{T_f^{\text{up}} - T_f^{\text{down}}}{T_f^{\text{up}} + T_f^{\text{down}}} \quad (6.5)$$

where X is the systematic variation; the resulting impact on the total background yields

from the $Z + \text{jets}$ theoretical uncertainties reaches a maximum of 3% and the uncertainties from the $W + \text{jets}$ sample variations are less than 3%.

top production: theory systematics on the $t\bar{t}$ and single top (Wt) backgrounds are evaluated as the difference between the predictions of the nominal MC samples, described in Section 5.5.1, and alternative samples with different generators. A number of uncertainties contribute to the total $t\bar{t}$ theory uncertainties: the extra radiation emitted by the initial and final state of the scattering process, estimated using modified parameters in the nominal Powheg+Pythia generator; hadronisation and PS uncertainties are obtained by comparing the yields of the nominal sample with those of alternative MC samples generated with Powheg and showered with Herwig, and the event-generator uncertainty is estimated by comparing Powheg+Herwig with an alternative MadGraph+Herwig; lastly, an extra source of uncertainty is produced by the combined modelling of the $t\bar{t}$ and single top (Wt) processes, whose final states produced are the same and are therefore a quantum mechanical interference affects them. Such effect is estimated using dedicated LO samples of $t\bar{t}$, Wt , and inclusive $WWbb$ production. These are generated with MadGraph, and the sum of $t\bar{t}$ and Wt predictions is compared to the $WWbb$ prediction. The largest impact of the total $t\bar{t}$ theory systematic uncertainties on the total background yields arises for SRC and it varies from 11% to 71% by tightening the R_{ISR} requirement.

$t\bar{t}+V$: for the irreducible $t\bar{t}+V$ background, the theoretical uncertainty is estimated using the following variations: renormalisation and factorisation scales varied up and down by a factor of two; the choice of PDF, in both $t\bar{t}+V$ and $t\bar{t}+\gamma$ MC simulations; a comparison between MC@NLO and OpenLoops+SHERPA generators. The uncertainties on the TFs, obtained as previously mentioned, were calculated using such method resulting in a maximum uncertainty of 2% in SRA-TT.

di-bosons: a 50% uncertainty is used for the di-bosons estimate;

SUSY signal: theory systematic uncertainties on the signal samples are generally dominated by the uncertainties on the choice of the PDF set and on the renormalisation and factorisation scales [155]. Such uncertainties range across the various SRs between 10% and 25% for the $\tilde{t} \rightarrow t^{(*)}\tilde{\chi}_1^0$ grid. The cross-section uncertainty is $\sim 15 - 20\%$ for direct stop production and $\sim 15 - 30\%$ for gluino production [126, 127, 128, 30] depending on the top-squark and gluino masses.

RESULTS AND STATISTICAL INTERPRETATION

7

*In God we trust. All others must
bring data.*

William E. Deming

The results of this analysis were published in a paper in the Journal of High Energy Physics in September 2017 [4]. A previous version of the analysis was also made public, using 13.3 fb^{-1} collected at $\sqrt{s} = 13\text{ TeV}$, with an earlier subset of the whole 2015 + 2016 dataset, documented in an ATLAS conference note [140]. Although both versions contain the author's contribution on the optimisation of the SRs and the estimation of the irreducible background $t\bar{t} + Z(\rightarrow \nu\nu)$, only the results of the most recent analysis will be hereby discussed, as it represents the most updated, improved and extended version. The chapter is structured as it follows: Section 7.1 is dedicated to a brief overview of the statistical analysis and the tools employed; the results together with their interpretations will be shown in Section 7.2. In addition, the results of the background estimation procedure, previously presented in Chapter 6, will be shown in Appendix A for a Dark Matter analysis.

7.1 Statistical analysis

Although a basic estimate of the value of the relevant parameters in signal and control regions can be obtained by solving systems as the one in Equation 6.3, a statistic tool, that takes into account all the uncertainties (statistical and systematic), is needed to produce quantitative results. The statistical tool - widely used in the ATLAS SUSY working group - to produce the analysis results is the `HistFitter` framework [148]. In particular, such framework is used for the implementation of two procedures: parameter estimation, such as SM background normalisation factors in Equation 6.3, and hypothesis test, which allow to measure the parameters from a given dataset, and to check the compatibility of the results obtained from the data analysis with a given hypothesis. `HistFitter` uses a frequentist¹ approach, where an event's probability is

¹ Frequentism is an interpretation of probability which defines an event's probability as the limit of its relative frequency in a large number of trials.

defined as the limit of its relative frequency in a large number of trials.

7.1.1 Estimation of the parameters and the statistical hypothesis testing

The interpretation of the data in control, validation, and SRs needs the of the SM background normalisation factors, μ_b , and the signal strength, μ_s . Given a set of selection cuts, the expected number of events in a region R can be calculated as:

$$N_R = \mu_s N_s + \sum_i \mu_b^i N_b^i \quad (7.1)$$

Here, N_b^i and N_s^i are the expected MC yields for the i^{th} background and the signal, respectively. Taking into account all the systematic uncertainties, a set of so-called *nuisance parameters* describing how signal and background are affected by the uncertainties can be introduced, and Equation 7.1 will be modified as it follows:

$$N_R = \mu_s N_s \left(1 + \sum_j \theta_s^j \sigma_s^j \right) + \sum_i \mu_b^i N_b^i \left(1 + \sum_j \theta_b^{ij} \sigma_b^{ij} \right), \quad (7.2)$$

θ_s^j is the j^{th} nuisance parameter. The numbers σ_s^j and σ_b^{ij} are the yields after taking into account the effect of the systematics, on the signal and backgrounds, respectively. Equation 7.2 is built to reflect a $\pm 1\sigma$ variation due to the systematic error σ when $\theta = \pm 1$, and to return the nominal (non varied) yields when $\theta = 0$.

A likelihood function, L , containing all the relevant parameters and information from the analysis, allows the extraction of the SM background normalisation factors, μ_b , signal strength, μ_s , and the nuisance parameters θ . The number of observed events in every SR or CR can be used to constrain the free parameters contained in the likelihood function, of which a general expression is the following:

$$\begin{aligned} L(N^{\text{obs}}, \boldsymbol{\theta}^0 | \mu_s, \mu_b, \boldsymbol{\theta}) &= P_{\text{SR}} \times P_{\text{CR}} \times C_{\text{syst}} = \\ &= \prod_{i \in \text{CR, SR}} P(N_i^{\text{obs}} | N_i(\mu_s, \mu_b, \boldsymbol{\theta})) \times C_{\text{syst}} \end{aligned} \quad (7.3)$$

This is the product of Poisson distributions of event counts in SRs or CRs (P_{SR} , P_{CR}), times a distribution describing the impact of the systematic uncertainties, C_{syst} . The Poisson factors contain the normalisation factors μ_s , μ_b , and the nuisance parameters $\boldsymbol{\theta}$ which is introduced to constrain the systematic uncertainty in the fit. C_{syst} can be generally treated as a unit Gaussian such that the fitted values of θ_i are expected to be approximately 0 ± 1 , allowing to reproduce the expected size of the systematic uncertainties using Equation 7.2. Further details can be found in Ref. [148]. The values of the relevant SM background normalisation parameters are then obtained by a Maximum Likelihood Estimation (MLE), once the likelihood in Equation 7.3 is constructed. Such procedure is discussed in detail in Ref. [156].

To determine whether a BSM signal is discovered, or excluded, a statistical procedure known as *statistical hypothesis testing* is employed [157]. A so-called null hypothesis H_0 , to be tested against an alternative H_1 , is defined. In particular, the discovery test for a BSM signal, is made by choosing H_0 and H_1 as the background-only and the signal-plus-background hypotheses, respectively. On the contrary, if such test returns a negative result, namely no BSM signal is found, exclusion limits are set by inverting the procedure.

The testing procedure is based on the following: a test statistic t , with a probability distribution $f(t)$ is defined together with a function of the observed data that assumes large values if the data are incompatible with the null hypothesis (H_0). Pseudo-experiments (also known as *toys*) are employed in large number to determine the shape of $f(t)$. In such toys, all the values of the physical observables can be randomly generated under the null hypothesis.

The null hypothesis (H_0) is tested through the computation of a p -value, which represents the probability of observing a larger incompatibility of the data with the predictions in an infinite number of repetitions of the experiment under the assumption that H_0 is valid. Once the distribution $f(t)$ is known, the computation of the p -value can be carried out as:

$$p = \int_{t_{\mu, \text{obs}}}^{\infty} f(t) dt \quad (7.4)$$

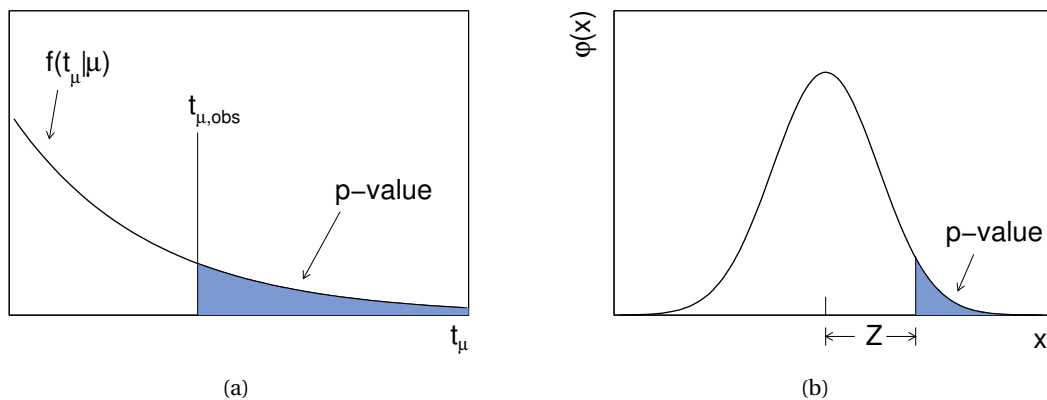


Figure 7.1: Illustration of the relation between the p -value obtained from an observed value of the test statistic t_μ (a), and the standard normal distribution showing the relation between the significance Z and the p -value (taken from [158]).

where, as shown in Figure 7.1 (a), $f(t)$ is integrated from the observed value of the test statistic, $t_{\mu, \text{obs}}$, to infinity. As a matter of fact, an equivalent quantity is instead considered, which is equivalent to the p -value: the significance, Z . For convenience, the p -value is converted into the significance, Z , defined as the number of standard deviations σ from the mean of a Gaussian distribution for which the integral of the tail of the curve is equal to p :

$$Z = \Phi^{-1}(1 - p) \quad (7.5)$$

Here, Φ^{-1} is the inverse of the cumulative distribution of the Gaussian, as it can be seen from

Figure 7.1 (b). The particle physics community has chosen $Z = 5$ ($Z = 3$) as the minimum value of significance needed to claim a discovery (evidence) against the background-only hypothesis, respectively. Such value of significance correspond to a p -value of 2.87×10^{-7} and $p = 0.0013$, respectively. A significance of 1.64σ ($p = 0.05$) is instead accepted to exclude a given signal model.

The choice of an appropriate test t is an important step in the statistical hypothesis testing procedure. From Equation 7.3 a statistic test can be obtained as it follows:

$$\lambda(\mu_s) = \frac{L(\mu_s, \hat{\theta})}{L(\hat{\mu}_s, \hat{\theta})} \quad (7.6)$$

where the vector θ takes into account the background normalisation factors and the nuisance parameters related to the systematic uncertainties. The numerator $L(\mu_s, \hat{\theta})$ is the maximum for a given value of μ_s , while the denominator $L(\hat{\mu}_s, \hat{\theta})$ corresponds to the absolute maximum of the likelihood function. As shown in Equation 7.6, $0 < \lambda < 1$: the larger the values the better the agreement of the data with the hypothesis being tested. It is possible to define a test statistic, with the range required by the definition of the p -value in Equation 7.4, as $t_{\mu, \text{obs}} = -2 \ln \lambda(\mu)$, where the larger the values the lower the compatibility between the observed data and the hypothesis being tested. Two test statistics can be defined, one for discovery and one for exclusion: the former tests the background-only hypothesis and employs a Profile Likelihood Ratio (PLR) function with $\mu_s = 0$; the test can be defined as:

$$q_0 = \begin{cases} -2 \ln \lambda(0) & \hat{\mu}_s \geq 0 \\ 0 & \hat{\mu}_s < 0 \end{cases} \quad (7.7)$$

The test statistic q_0 is set to 0 for negative $\hat{\mu}_s$ such that the exclusion of the background-only hypothesis, when a deficit of events is observed in the SRs, can be avoided. The latter, employed for the exclusion of a signal model, employs a test statistic which can be defined as:

$$q_\mu = \begin{cases} -2 \ln \lambda(\mu_s) & \hat{\mu}_s \leq \mu_s \\ 0 & \hat{\mu}_s > \mu_s \end{cases} \quad (7.8)$$

where, the signal strength, μ_s , assumed to be non-zero in the null hypothesis.

Unfortunately, for signal models to which the analysis is poorly sensitive, Equation 7.8 can return a non-negligible probability and, although it can be argued that any constrain on such models should not be put, it is still possible that in the signal-plus-background hypothesis low p -values can be obtained when the observed events in the SRs are fewer than the predicted ones. The introduction of an alternative Figure of Merit (FoM) for the exclusion can be employed [159]:

$$\text{CL}_s = \frac{p_{\mu_s}}{1 - p_b} \quad (7.9)$$

where p_b and p_{μ_s} correspond to the p -values of the background-only and signal-plus-background hypotheses, respectively. A 95% Confidence Level (CL) is reached when $CL_s < 0.05$, i. e. a threshold of $Z = 2$. Ultimately, when discovery and exclusion test statistics show similar distributions, this will translate into a numerator and denominator of the same order (Equation 7.9), which guarantees that signals are not excluded, as one would expect.

7.1.2 Discovery and exclusion

The parameter estimation discussed in Section 7.1 is the heart of the estimation of the SM-background normalisation factors which is an essential part of the background estimation procedure discussed in Section 6.1. All the various CR selections are plugged in a likelihood function of the form of Equation 7.3 which is then maximised in order to determine all the normalisation factors, nuisance parameters, and correlations between them. The so-obtained parameters are then used in Equation 7.1.

The statistical hypothesis testing procedure discussed in Section 7.1 is used to evaluate the p -value for the background-only hypothesis to interpret the results in all the SRs. The likelihood function, including all the CRs and the SR being tested, is employed to build a PLR function. The yield predictions in such SR are then determined solely by looking at the SM processes i. e. the signal strength, μ_s , is set to 0. The Equation 7.7 is then used to compute the p -value and the significance, Z , using either toys the relevant asymptotic formula [160].

Finally, if no excess is observed in any of the SRs, the CL_s method is used to set exclusion limits on several signal hypotheses by computing the q_0 and q_μ test statistics under the background-only hypothesis for a given signal strength, employing the minimisation of various likelihood functions.

7.2 Results and Interpretation

In this section the results of this analysis will be presented. The results of the background-only fit and the unblinded SRs, together with the relevant distributions, will be discussed in Section 7.2.1 and 7.2.2, respectively. Finally, in Section 7.2.3 the limits on different signal models will be presented, if no evidence for new physics is found.

7.2.1 Background-only fit

The accuracy of the background estimation strategy, discussed in Chapter 6 is verified through dedicated sets of VRs. As previously anticipated, in such regions the data are expected to match the SM predictions within the uncertainties and the signal contamination is required to be low. Figure 6.1 shows where the VRs should generally lay such that the impact of any potential bias that may affect the TFs can be assessed. Before the blinding procedure of the SRs of the analysis, the necessary condition to be checked is the agreement between data and predictions.

Then the signal, if any, will be expected to appear in the SRs as an excess of events with respect to the background-only hypothesis, with no corresponding effect in the VRs. In the case of a background-only fit, a likelihood fit is performed only using the various CRs described in Section 6.1.1 and Appendix B. Figure 7.2 shows the comparison between observed data and MC predictions of all relevant variables.

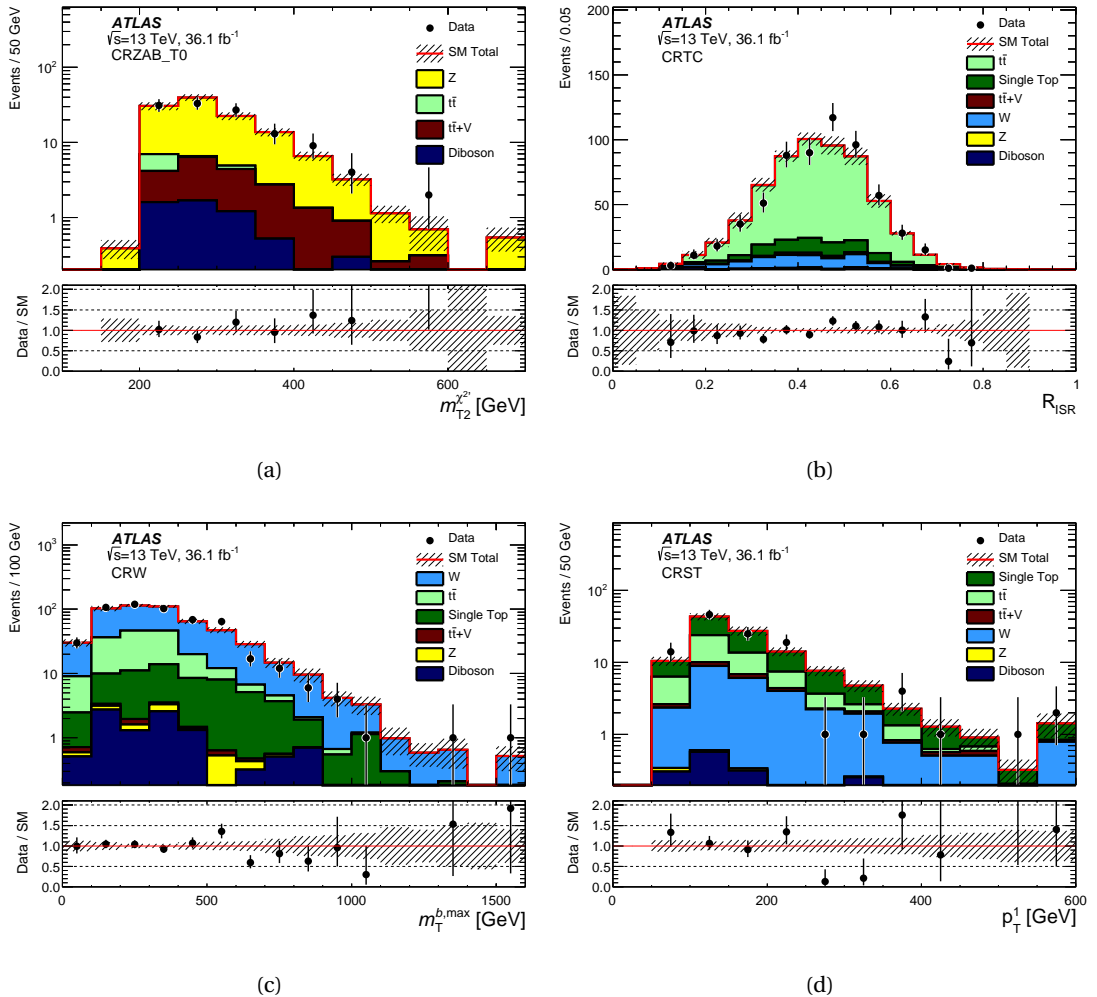


Figure 7.2: Distributions of the most relevant variables: (a) $m_{T_2}^{\chi_2'}$ in CRZAB-T0, (b) $E_T^{\text{miss}'}$ in CRZE, (c) R_{ISR} in CRTC, (d) $m_T^{b,\text{max}}$ in CRW, (e) the transverse momentum of the second-leading- p_T jet in CRST. The stacked histograms show the SM prediction, normalised using scale factors derived from the simultaneous fit to all backgrounds, discussed in Section 7.1. The ratio of data events to the total SM prediction is also shown. The uncertainty band around the SM prediction and in the ratio plot illustrates the combination of MC statistical and detector-related systematic uncertainties. The rightmost bin includes overflow events [4].

The result of the simultaneous fit procedure, described in Section 7.1, performed with the VRs used as test SRs, for each VR is shown in Figure 7.3, which displays the agreement between data and MC predictions. Here, the normalisation factors of the various SM background estimation - all between 0.9 – 1.3 - were used. Additionally, in all the VRs the signal contamination was checked for all the signals considered that have not yet been excluded. The largest signal contamination is $\sim 25\%$ in the VRTs for top-squark masses below 350 GeV and in VRZD and VRZE near top-squark masses of 700 GeV.

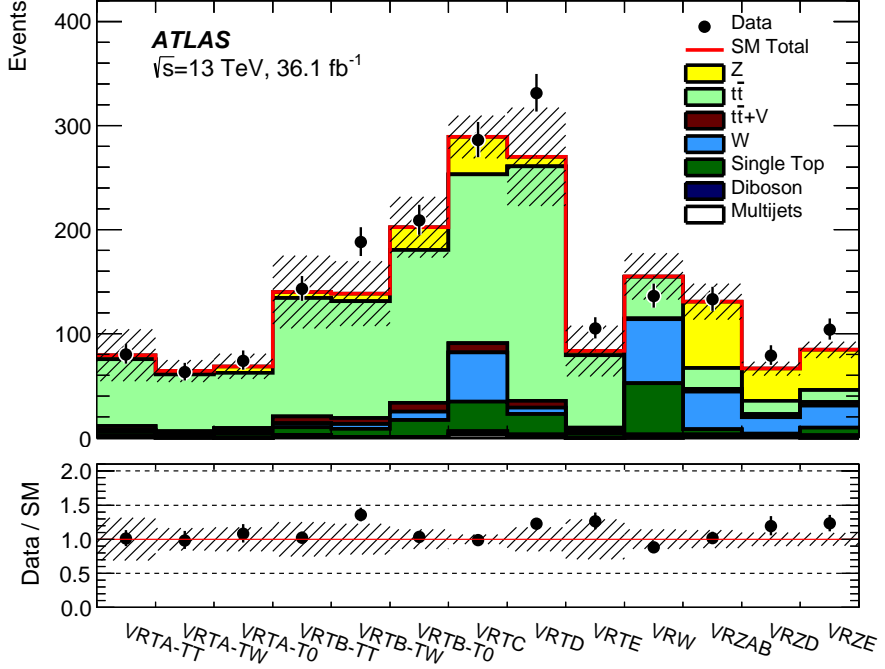


Figure 7.3: Yields for all the VRs after the likelihood fit. The stacked histograms show the SM prediction and the uncertainty band around the SM prediction shows the total uncertainty, which consists of the MC statistical uncertainties, detector-related systematic uncertainties, and theoretical uncertainties in the extrapolation from CR to VR.

7.2.2 Opening Pandora’s box: unblinded SRs

The good agreement found in the CRs and VRs gives confidence in the modelling of the relevant SM backgrounds and their estimation, therefore the SRs can now be unblinded. The event data counts are compared to the expected total number of background events in Tables 7.1, 7.2, and 7.3. Figure 7.4 shows a summary of all the SR yields after having performed the simultaneous likelihood fit.

The analysis yielded no significant excess above the SM prediction in any of the SRs, as it can be seen in Figure 7.4. The smallest p -values are 27%, 27%, and 29% for SRB-T0, SRD-high, and SRA-TT, respectively. The largest deficit in the data is observed in SRC4 where only one event is observed against 7.7 expected background events and this is probably due to the very low statistics.

Figure 7.5 shows the $N - 1$ distributions, obtained by applying all the SR selections but the cut on the variable plotted, of E_T^{miss} , $m_{\text{T}2}^{\chi^2}$, $m_{\text{T}}^{b,\text{max}}$, m_{T} , R_{ISR} , and H_{T} , for the various SRs, with R_{ISR} being shown combining SRC1–5. The background predictions in these distributions are scaled to the values determined from the simultaneous fit. A good data-SM prediction agreement is observed across the whole kinematical range in the displayed plots, confirming once again the reliability of the presented background estimation strategy.

Table 7.1: Observed and expected yields, before and after the fit, for SRA and SRB. The uncertainties include MC statistical uncertainties, detector-related systematic uncertainties, and theoretical uncertainties in the extrapolation from CR to SR [4].

	SRA-TT	SRA-TW	SRA-T0	SRB-TT	SRB-TW	SRB-T0
Observed	11	9	18	38	53	206
Total SM (fit)	8.6 \pm 2.1	9.3 \pm 2.2	18.7 \pm 2.7	39.3 \pm 7.6	52.4 \pm 7.4	179 \pm 26
$t\bar{t}$	0.71 $^{+0.91}_{-0.71}$	0.51 $^{+0.55}_{-0.51}$	1.31 \pm 0.64	7.3 \pm 4.3	12.4 \pm 5.9	43 \pm 22
$W + \text{jets}$	0.82 \pm 0.15	0.89 \pm 0.56	2.00 \pm 0.83	7.8 \pm 2.8	4.8 \pm 1.2	25.8 \pm 8.8
$Z + \text{jets}$	2.5 \pm 1.3	4.9 \pm 1.9	9.8 \pm 1.6	9.0 \pm 2.8	16.8 \pm 4.1	60.7 \pm 9.6
$t\bar{t}+V$	3.16 \pm 0.66	1.84 \pm 0.39	2.60 \pm 0.53	9.3 \pm 1.7	10.8 \pm 1.6	20.5 \pm 3.2
Single top	1.20 \pm 0.81	0.70 \pm 0.42	2.9 \pm 1.5	4.2 \pm 2.2	5.9 \pm 2.8	26 \pm 13
Dibosons	--	0.35 \pm 0.26	--	0.13 \pm 0.07	0.60 \pm 0.43	1.04 \pm 0.73
Multijets	0.21 \pm 0.10	0.14 \pm 0.09	0.12 \pm 0.07	1.54 \pm 0.64	1.01 \pm 0.88	1.8 \pm 1.5
Total SM (exp)	7.1	7.9	16.3	32.4	46.1	162

Table 7.2: Observed and expected yields, before and after the fit. The uncertainties include MC statistical uncertainties, detector-related systematic uncertainties, and theoretical uncertainties in the extrapolation from CR to SR [4].

	SRC1	SRC2	SRC3	SRC4	SRC5
Observed	20	22	22	1	0
Total SM (fit)	20.6 \pm 6.5	27.6 \pm 4.9	18.9 \pm 3.4	7.7 \pm 1.2	0.91 \pm 0.73
$t\bar{t}$	12.9 \pm 5.9	22.1 \pm 4.3	14.6 \pm 3.2	4.91 \pm 0.97	0.63 $^{+0.70}_{-0.63}$
$W + \text{jets}$	0.80 \pm 0.37	1.93 \pm 0.49	1.91 \pm 0.62	1.93 \pm 0.46	0.21 \pm 0.12
$Z + \text{jets}$	--	--	--	--	--
$t\bar{t}+V$	0.29 \pm 0.16	0.59 \pm 0.38	0.56 \pm 0.31	0.08 \pm 0.08	0.06 \pm 0.02
Single top	1.7 \pm 1.3	1.2 $^{+1.4}_{-1.2}$	1.22 \pm 0.69	0.72 \pm 0.37	--
Dibosons	0.39 \pm 0.33	0.21 $^{+0.23}_{-0.21}$	0.28 \pm 0.18	--	--
Multijets	4.6 \pm 2.4	1.58 \pm 0.77	0.32 \pm 0.17	0.04 \pm 0.02	--
Total SM (exp)	25.4	36.0	24.2	9.2	1.1

Table 7.3: Observed and expected yields, before and after the fit, for SRD and SRE. The uncertainties include MC statistical uncertainties, detector-related systematic uncertainties, and theoretical uncertainties in the extrapolation from CR to SR [4].

	SRD-low	SRD-high	SRE
Observed	27	11	3
Total SM (fit)	25.1 ± 6.2	8.5 ± 1.5	3.64 ± 0.79
$t\bar{t}$	3.3 ± 3.3	0.98 ± 0.88	$0.21^{+0.39}_{-0.21}$
$W + \text{jets}$	6.1 ± 2.9	1.06 ± 0.34	0.52 ± 0.27
$Z + \text{jets}$	6.9 ± 1.5	3.21 ± 0.62	1.36 ± 0.25
$t\bar{t}+V$	3.94 ± 0.85	1.37 ± 0.32	0.89 ± 0.19
Single top	3.8 ± 2.1	1.51 ± 0.74	0.66 ± 0.49
Dibosons	--	--	--
Multijets	1.12 ± 0.37	0.40 ± 0.15	--
Total SM (exp.)	22.4	7.7	3.02

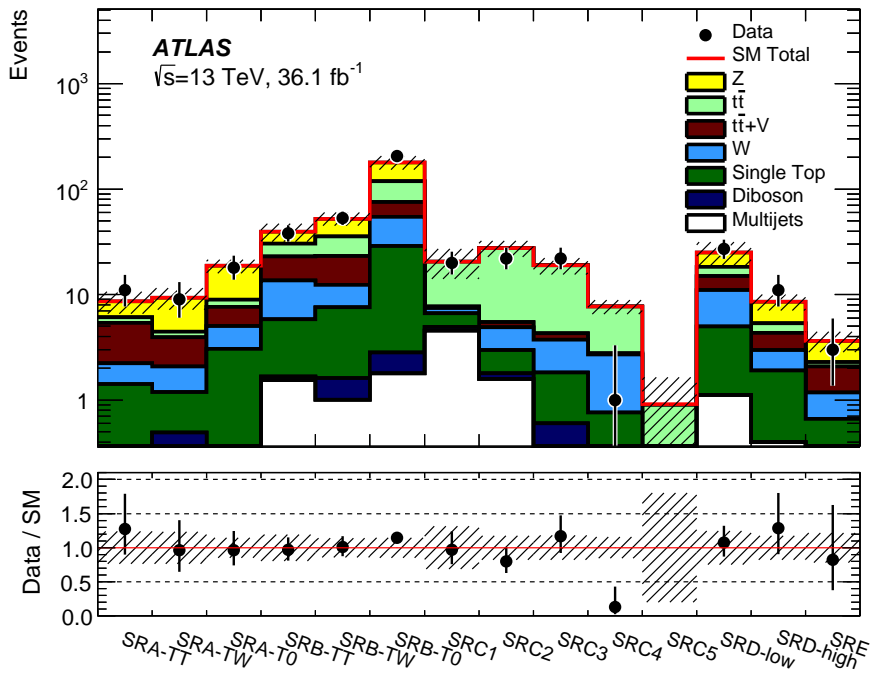


Figure 7.4: Yields for all signal regions after the likelihood fit. The stacked histograms show the SM prediction and the hatched uncertainty band around the SM prediction shows total uncertainty, which consists of the MC statistical uncertainties, detector-related systematic uncertainties, and theoretical uncertainties in the extrapolation from CR to SR [4].

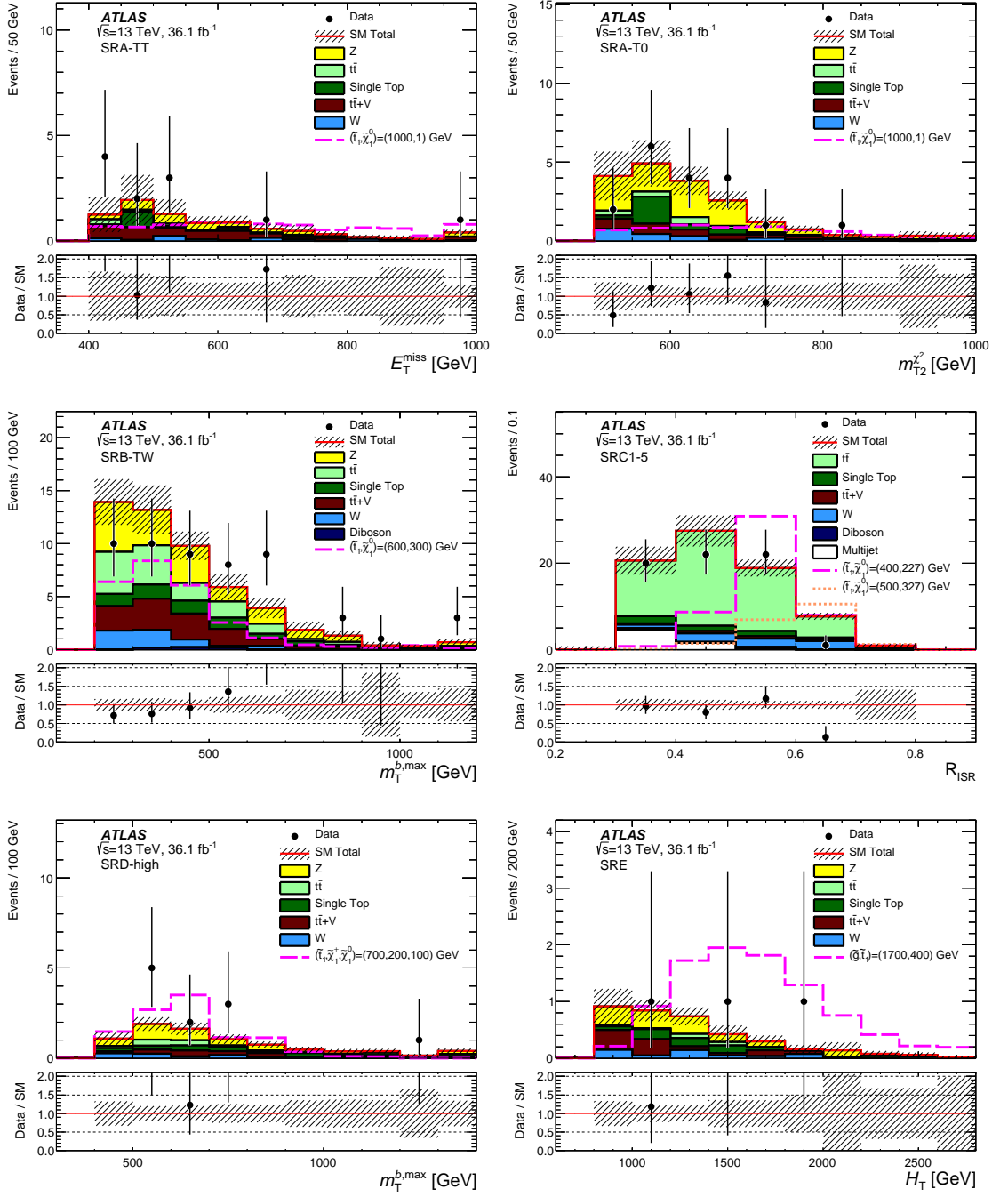


Figure 7.5: Distributions of E_T^{miss} for SRA-TT, $m_{T_2}^{\chi^2}$ for SRA-T0, $m_T^{b,\text{max}}$ for SRB-TW, R_{ISR} for SRC1-5, $m_T^{b,\text{max}}$ for SRD-high and H_T for SRE obtained after having performed the likelihood fit. The stacked histograms show the SM prediction and the hatched uncertainty band around the SM prediction shows the MC statistical and detector-related systematic uncertainties. For each variable, the distribution for a representative signal point is shown [4].

7.2.3 Setting the limits

As no excess over the SM is observed in any of the investigated SRs, exclusion limits are set. In particular, the CL_s method, discussed in Section 7.1, is used to perform the exclusion fits. Model-independent limits on the visible BSM cross section, defined as $\sigma_{\text{vis}} = S_{\text{obs}}^{95} / \int \mathcal{L} dt$, where S_{obs}^{95} is the 95% CL upper limit on the number of signal events, are reported in Table 7.4.

Table 7.4: Left to right: 95% CL upper limits on the average visible cross section ($\langle \sigma A \epsilon \rangle_{\text{obs}}^{95}$) where the average comes from possibly multiple production channels and on the number of signal events (S_{obs}^{95}). The third column (S_{exp}^{95}) shows the 95% CL upper limit on the number of signal events, given the expected number (and $\pm 1\sigma$ excursions of the expected number) of background events. The discovery p -value (p) and the corresponding significance (Z) are shown in the last column [4].

Signal channel	$\langle \sigma A \epsilon \rangle_{\text{obs}}^{95}$ [fb]	S_{obs}^{95}	S_{exp}^{95}	$p (Z)$
SRA-TT	0.30	11.0	$8.7^{+3.0}_{-1.4}$	0.23 (0.74)
SRA-TW	0.27	9.6	$9.6^{+2.8}_{-2.1}$	0.50 (0.00)
SRA-T0	0.31	11.2	$11.5^{+3.8}_{-2.0}$	0.50 (0.00)
SRB-TT	0.54	19.6	$20.0^{+6.5}_{-4.9}$	0.50 (0.00)
SRB-TW	0.60	21.7	$21.0^{+7.3}_{-4.3}$	0.50 (0.00)
SRB-T0	2.19	80	58^{+23}_{-17}	0.13 (1.15)
SRC1	0.42	15.1	$15.8^{+4.8}_{-3.5}$	0.50 (0.00)
SRC2	0.31	11.2	$13.9^{+5.9}_{-3.6}$	0.50 (0.00)
SRC3	0.42	15.3	$12.3^{+4.7}_{-3.4}$	0.27 (0.62)
SRC4	0.10	3.5	$6.7^{+2.8}_{-1.8}$	0.50 (0.00)
SRC5	0.09	3.2	$3.0^{+1.1}_{-0.1}$	0.23 (0.74)
SRD-low	0.50	17.9	$16.4^{+6.3}_{-4.0}$	0.36 (0.35)
SRD-high	0.30	10.9	$8.0^{+3.4}_{-1.3}$	0.21 (0.79)
SRE	0.17	6.1	$6.4^{+1.4}_{-2.4}$	0.50 (0.00)

The detector acceptance multiplied by the efficiency, $A \cdot \epsilon$, is calculated for all the SRs and the equivalent benchmark points. In particular, for signal regions designed to aim at the high-energy final states, SRA and SRE, $A \cdot \epsilon$ is estimated to be 9% and 6% for their respective signal benchmark points, previously discussed in Section 5.1, $m_{\tilde{t}} = 1000$ GeV, $m_{\tilde{\chi}^0} = 1$ GeV, and $m_{\tilde{g}} = 1700$ GeV, $m_{\tilde{t}} = 400$ GeV, $m_{\tilde{\chi}^0} = 395$ GeV. In SRB, SRD-low, and SRD-high the estimates of such values is 1.4%, 0.05%, and 0.5% for $m_{\tilde{t}} = 600$ GeV, $m_{\tilde{\chi}^0} = 300$ GeV; $m_{\tilde{t}} = 400$ GeV, $m_{\tilde{\chi}_1^\pm} = 100$ GeV, $m_{\tilde{\chi}^0} = 50$ GeV; and $m_{\tilde{t}} = 700$ GeV, $m_{\tilde{\chi}_1^\pm} = 200$ GeV, $m_{\tilde{\chi}^0} = 100$ GeV, where the branching ratio, $B(\tilde{t} \rightarrow b \tilde{\chi}_1^\pm) = 100\%$ is assumed for the SRD samples, respectively. The combination of SRC1–5 through the R_{ISR} windows shows an $A \cdot \epsilon$ of 0.08% for $m_{\tilde{t}} = 400$ GeV, $m_{\tilde{\chi}^0} = 227$ GeV. Furthermore, orthogonal signal subregions, namely SRA-TT, SRA-TW, and SRA-T0, are statistically combined by multiplying their likelihood functions, and the same procedure is applied

to the SRB and SRC signal subregions. For the overlapping SRs SRD-low and SRD-high, the signal region with the smallest expected CL_s value is chosen for each signal model. Once the signal subregions are combined or chosen, the signal region with the smallest expected CL_s is chosen for each signal model in the $\tilde{t}-\tilde{\chi}_1^0$ signal grid. The expected limits are determined by setting the nominal event yield in each SR to the mean background expectation; contours that correspond to $\pm 1\sigma$ uncertainties in the background estimates, σ_{exp} , are also evaluated. The observed event yields determine the observed limits for each SR; these are evaluated for the nominal signal cross sections as well as for $\pm 1\sigma$ theory uncertainties in those cross sections, denoted by $\sigma_{\text{theory}}^{\text{SUSY}}$.

The observed (solid red line) and expected (solid blue line) exclusion contours at 95% CL in the $\tilde{t}-\tilde{\chi}_1^0$ mass plane are shown in Figure 7.6. The data excludes top-squark masses between 450 and 950 GeV for $\tilde{\chi}_1^0$ masses below 160 GeV, extending Run-1 limits by 260 GeV. The newly explored “diagonal” case, where $m_{\tilde{t}} \approx m_t + m_{\tilde{\chi}_1^0}$, was also added. Here top-squark masses in the range 235–590 GeV are excluded.

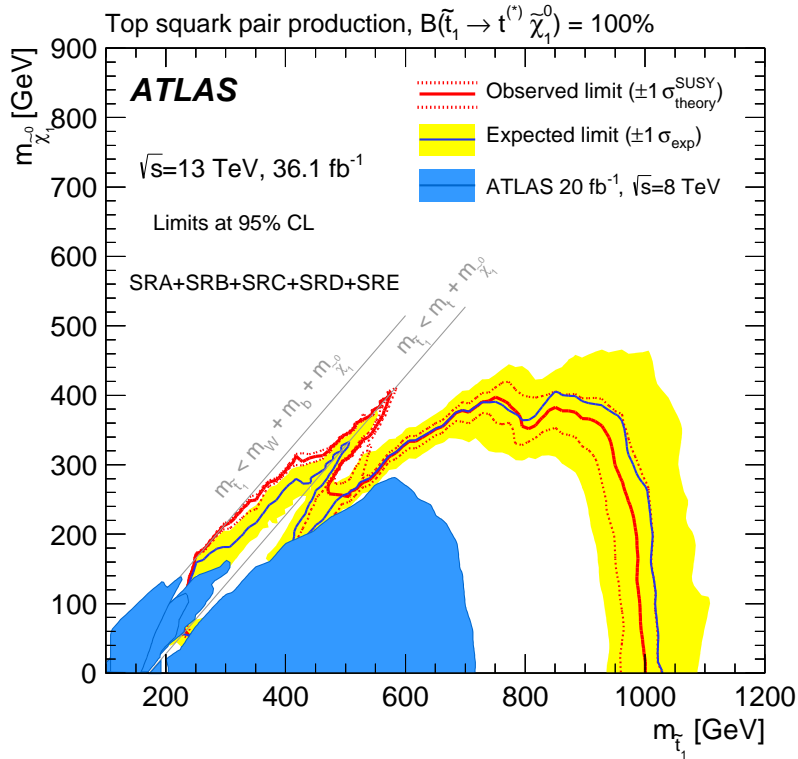


Figure 7.6: Observed (red solid line) and expected (blue solid line) exclusion contours at 95% CL as a function of \tilde{t} and $\tilde{\chi}_1^0$ masses in the scenario where both top squarks decay via $\tilde{t} \rightarrow t^{(*)}\tilde{\chi}_1^0$. Masses that are within the contours are excluded. Uncertainty bands corresponding to the $\pm 1\sigma$ variation of the expected limit (yellow band) and the sensitivity of the observed limit to $\pm 1\sigma$ variations of the signal theoretical uncertainties (red dotted lines) are also indicated [4]. Observed limits from all third-generation Run-1 searches [161] at $\sqrt{s}=8$ TeV overlaid for comparison in blue.

Signal models where top-squark decays into $b\tilde{\chi}_1^\pm$, or into additional massive neutralinos, are interpreted in four different scenarios [4]:

Natural SUSY-inspired mixed grid: a simplified model [162] where $m_{\tilde{\chi}_1^\pm} = m_{\tilde{\chi}_1^0} + 1$ GeV with

only two decay modes, $\tilde{t} \rightarrow b\tilde{\chi}_1^\pm$ and $\tilde{t} \rightarrow t\tilde{\chi}_1^0$, and only on-shell top-quark decays are considered. The same maximal mixing between the partners of the left- and right-handed top quarks and nature of the $\tilde{\chi}_1^0$ (pure bino) as for the $B(\tilde{t} \rightarrow t\tilde{\chi}_1^0) = 100\%$ case is assumed. The branching ratio to $\tilde{t} \rightarrow t\tilde{\chi}_1^0$ is set to 0%, 25%, 50%, and 75%. The limits obtained are shown in Figure 7.7.

Non-asymptotic higgsino: a pMSSM-inspired simplified model with a higgsino LSP, $m_{\tilde{\chi}_1^\pm} = m_{\tilde{\chi}^0} + 5$ GeV, and $m_{\tilde{\chi}_2^0} = m_{\tilde{\chi}^0} + 10$ GeV, assumes three sets of branching ratios for the considered decays of $\tilde{t} \rightarrow t\tilde{\chi}_2^0$, $\tilde{t} \rightarrow t\tilde{\chi}_1^0$, $\tilde{t} \rightarrow b\tilde{\chi}_1^\pm$ [162]. A set of branching ratios with $B(\tilde{t} \rightarrow t\tilde{\chi}_2^0, \tilde{t} \rightarrow t\tilde{\chi}_1^0, \tilde{t} \rightarrow b\tilde{\chi}_1^\pm) = 33\%, 33\%, 33\%$ is considered, which is equivalent to a pMSSM model with the lightest top squark mostly consisting of the superpartner of left-handed top quark and $\tan\beta = 60$ (ratio of vacuum expectation values of the two Higgs doublets). Additionally, $B(\tilde{t} \rightarrow t\tilde{\chi}_2^0, \tilde{t} \rightarrow t\tilde{\chi}_1^0, \tilde{t} \rightarrow b\tilde{\chi}_1^\pm) = 45\%, 10\%, 45\%$ and $B(\tilde{t} \rightarrow t\tilde{\chi}_2^0, \tilde{t} \rightarrow t\tilde{\chi}_1^0, \tilde{t} \rightarrow b\tilde{\chi}_1^\pm) = 25\%, 50\%, 25\%$ are assumed, which correspond to scenarios in which $m_{q\tilde{L}3} < m_{t\tilde{R}}$ (regardless of the choice of $\tan\beta$) and $m_{t\tilde{R}} < m_{q\tilde{L}3}$ with $\tan\beta = 20$, respectively. Here $m_{q\tilde{L}3}$ represents the left-handed third-generation mass parameter and $m_{t\tilde{R}}$ is the mass parameter of the superpartner to the right-handed top-quark. Limits in the $m_{\tilde{t}}$ and $m_{\tilde{\chi}^0}$ plane are shown in Figure 7.8.

Wino-NLSP pMSSM: a pMSSM model where the LSP is bino-like and has mass M_1 and where the NLSP is wino-like with mass M_2 , while $M_2 = 2M_1$ and $m_{\tilde{t}} > M_1$ [162]. Limits are set for both positive and negative μ (the higgsino mass parameter) as a function of the \tilde{t} and $\tilde{\chi}_1^0$ masses which can be translated to different M_1 and $m_{q\tilde{L}3}$, and are shown in Figure 7.9. Only bottom and top-squark production are considered in this interpretation. Allowed decays in the top-squark production scenario are $\tilde{t} \rightarrow t\tilde{\chi}_2^0 \rightarrow h/Z\tilde{\chi}_1^0$, at a maximum branching ratio of 33%, and $\tilde{t} \rightarrow b\tilde{\chi}_1^\pm$. Whether the $\tilde{\chi}_2^0$ dominantly decays into a h or Z is determined by the sign of μ . Along the diagonal region, the $\tilde{t} \rightarrow t\tilde{\chi}_1^0$ decay with 100% branching ratio is also considered. The equivalent decays in bottom-squark production are $\tilde{b} \rightarrow t\tilde{\chi}_1^\pm$ and $\tilde{b} \rightarrow b\tilde{\chi}_2^0$. The remaining pMSSM parameters have the following values: $M_3 = 2.2$ TeV (gluino mass parameter), $M_S = \sqrt{m_{\tilde{t}_1} m_{\tilde{t}_2}} = 1.2$ TeV (geometric mean of top-squark masses), $X_t/M_S = \sqrt{6}$ (mixing parameter between the superpartners of left- and right-handed states, where $X_t = A_t - \mu/\tan\beta$ and A_t is the trilinear coupling parameter in the top-quark sector), and $\tan\beta = 20$. All other pMSSM masses are set to > 3 TeV.

Well-tempered neutralino pMSSM: another pMSSM model in which three light neutralinos and a light chargino, which are mixtures of bino and higgsino states, are considered with masses within 50 GeV of the lightest state [163, 164]. Such model is designed to satisfy the SM Higgs boson mass and the dark-matter relic density ($0.10 < \Omega h^2 < 0.12$, where Ω is energy density parameter and h is the Planck constant [165]) with pMSSM parameters: $M_1 = -(\mu + \delta)$ where $\delta = 20\text{--}50$ GeV, $M_2 = 2.0$ TeV, $M_3 = 1.8$ TeV, $M_S = 0.8\text{--}1.2$ TeV, $X_t/M_S \sim \sqrt{6}$, and $\tan\beta = 20$. For this model, limits are shown in Figure 7.10. Bottom- and top-squark production only are considered in this interpretation. Finally, the signal

grid points were produced in two planes, μ - $m_{\tilde{t}R}$ and μ - $m_{q\tilde{L}3}$, and then projected to the corresponding \tilde{t} and $\tilde{\chi}_1^0$ masses. The remaining pMSSM masses are set to > 3 TeV.

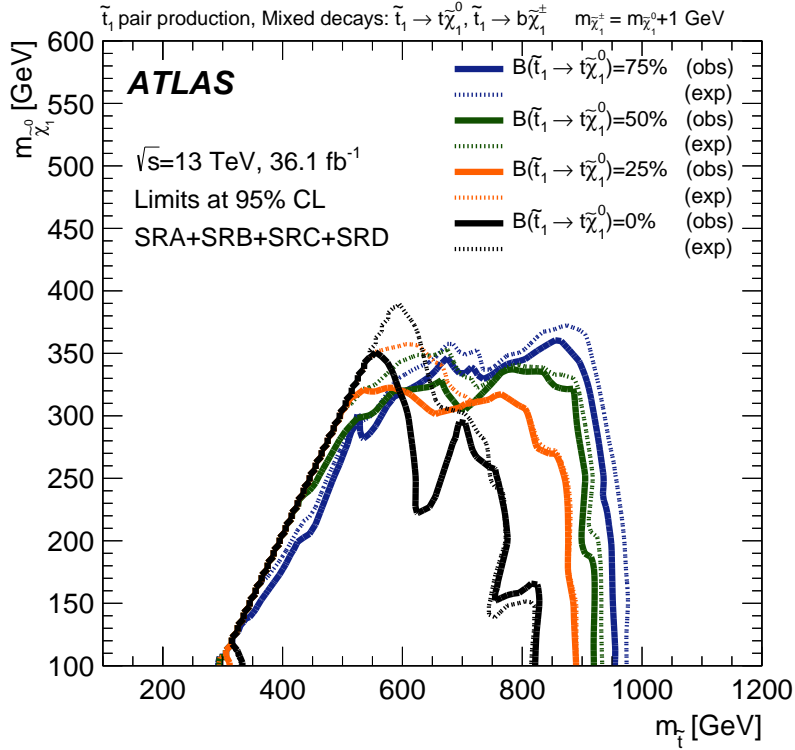


Figure 7.7: Observed (solid line) and expected (dashed line) exclusion contours at 95% CL as a function of \tilde{t} and $\tilde{\chi}_1^0$ masses and branching ratio to $\tilde{t} \rightarrow t\tilde{\chi}_1^0$ in the natural SUSY-inspired mixed grid scenario where $m_{\tilde{\chi}_1^\pm} = m_{\tilde{\chi}_1^0} + 1$ GeV (taken from [4]).

The SRE results are interpreted for gluino-mediated top-squark production via gluino decays in terms of the \tilde{t} - \tilde{g} mass plane with $\Delta m(\tilde{t}, \tilde{\chi}_1^0) = 5$ GeV. Figure 7.11 shows the exclusion plot of gluino masses up to $m_{\tilde{g}} = 1800$ GeV with $m_{\tilde{t}} < 800$ GeV.

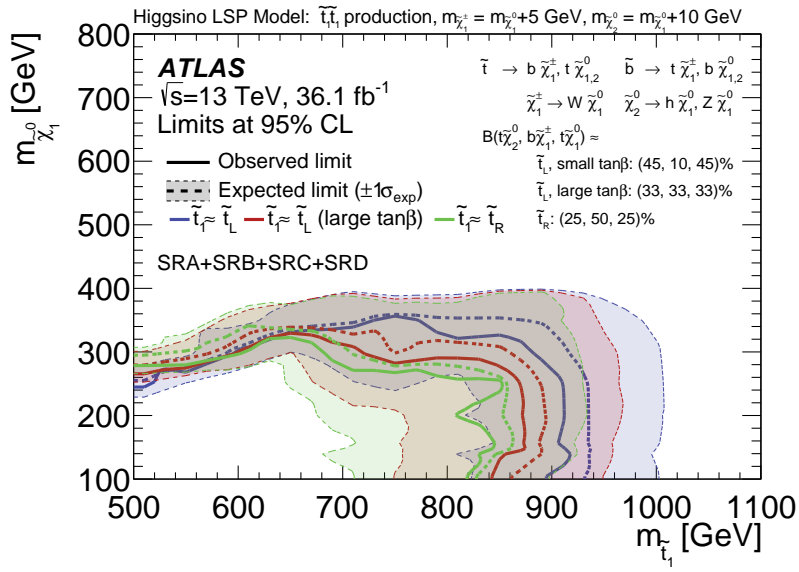


Figure 7.8: Observed (solid line) and expected (dashed line) exclusion contours at 95% CL as a function of $m_{\tilde{t}}$ and $m_{\tilde{\chi}_1^0}$ for the pMSSM-inspired non-asymptotic higgsino simplified model for a small $\tan\beta$ with $B(\tilde{t} \rightarrow t\tilde{\chi}_2^0, \tilde{t} \rightarrow t\tilde{\chi}_1^0, \tilde{t} \rightarrow b\tilde{\chi}_1^\pm) = 45\%, 10\%, 45\%$ (blue), a large $\tan\beta$ with $B(\tilde{t} \rightarrow t\tilde{\chi}_2^0, \tilde{t} \rightarrow t\tilde{\chi}_1^0, \tilde{t} \rightarrow b\tilde{\chi}_1^\pm) = 33\%, 33\%$, 33% (red), and a small \tilde{t}_R with $B(\tilde{t} \rightarrow t\tilde{\chi}_2^0, \tilde{t} \rightarrow t\tilde{\chi}_1^0, \tilde{t} \rightarrow b\tilde{\chi}_1^\pm) = 25\%, 50\%, 25\%$ (green) assumption. Uncertainty bands correspond to the $\pm 1\sigma$ variation of the expected limit(taken from [4]).

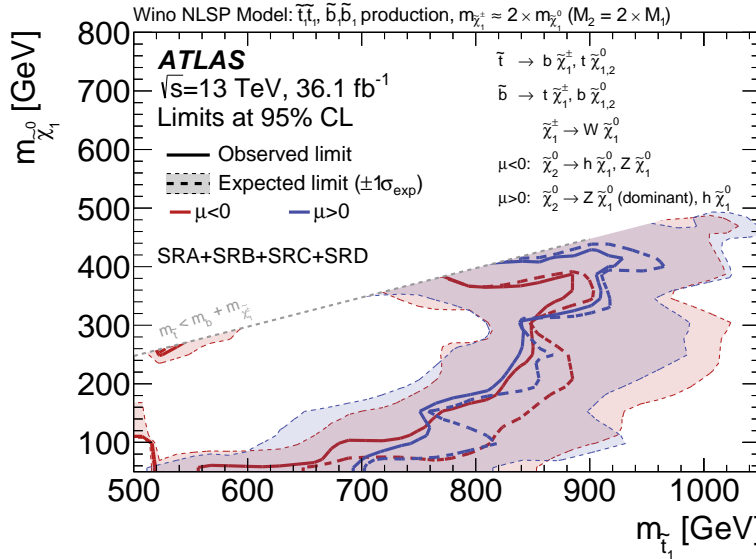
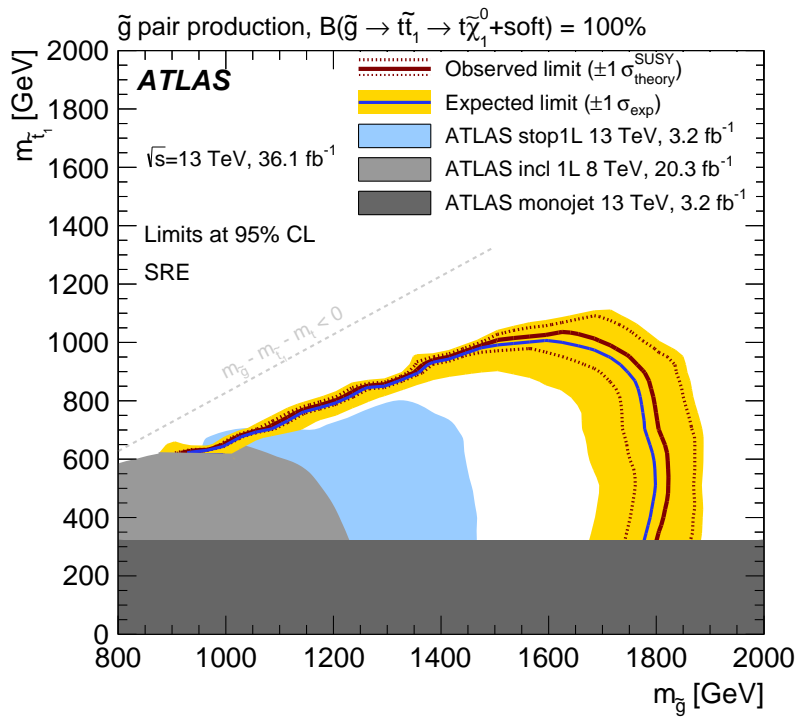
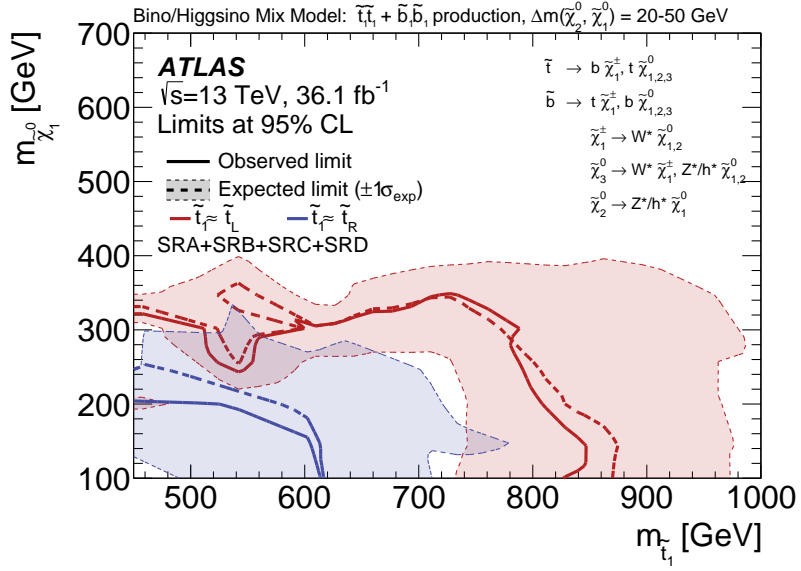


Figure 7.9: Observed (solid line) and expected (dashed line) exclusion contours at 95% CL as a function of \tilde{t} and $\tilde{\chi}_1^0$ masses for the Wino NLSP pMSSM model for both positive (blue) and negative (red) values of μ . Uncertainty bands correspond to the $\pm 1\sigma$ variation of the expected limit (taken from [4]).



CONCLUSIONS

*Every new beginning comes from
some other beginning's end.*

Seneca

The main outcome presented in this thesis is the best results to date of the search for the supersymmetric partner of the top quark in all-hadronic final states using the full 36.1 fb^{-1} dataset (2015 + 2016) of pp collisions at a centre-of-mass energy $\sqrt{s} = 13\text{ TeV}$ delivered by the LHC and collected by the ATLAS detector [4]. The $t\bar{t} + Z(\rightarrow \nu\nu)$ irreducible SM background and the relative theory uncertainties were estimated using a data-driven $t\bar{t}+\gamma$ CR and scenarios in which R -parity is conserved were targeted and final states with high- p_T jets and large missing transverse momentum, were addressed using selection criteria optimised accordingly. No significant deviation between the expected Standard Model events and the data was found.

A statistical interpretation of the results was carried out in order to set 95% CL exclusion limits on the parameters of the models considered resulting in the exclusion of top-squark masses in the range $450 - 1000\text{ GeV}$ for $\tilde{\chi}_1^0$ masses below 160 GeV improving the Run-1 results [136] by almost 400 GeV . A new SR was designed to address the diagonal case, $m_{\tilde{t}_1} \sim m_t + m_{\tilde{\chi}_1^0}$, where top-squark masses in the range $235 - 590\text{ GeV}$ are excluded. Additionally, limits that take into account an additional decay of $\tilde{t}_1 \rightarrow b\tilde{\chi}_1^\pm$ were set excluding top-squark masses between 450 and 850 GeV for neutralino masses below 240 GeV and $B(\tilde{t}_1 \rightarrow t\tilde{\chi}_1^0) = 50\%$ for $m_{\tilde{\chi}^\pm} = m_{\tilde{\chi}_1^0} + 1\text{ GeV}$. Limits were also derived in two pMSSM models, where one model assumes a wino-like NLSP and the other model is constrained by the dark-matter relic density. In addition, limits were set in terms of one pMSSM-inspired simplified model where $m_{\tilde{\chi}_1^\pm} = m_{\tilde{\chi}_1^0} + 5\text{ GeV}$ and $m_{\tilde{\chi}_2^0} = m_{\tilde{\chi}_1^0} + 10\text{ GeV}$. Gluino masses were constrained to be above 1800 GeV for \tilde{t}_1 masses below 800 GeV for gluino-mediated top squark production where $m_{\tilde{t}_1} = m_{\tilde{\chi}_1^0} + 5\text{ GeV}$.

The data-driven estimation of the irreducible $t\bar{t} + Z(\rightarrow \nu\nu)$ background and its relative theory uncertainties were also used in another ATLAS search, for dark matter produced in association with third-generation quarks [168], of which a brief overview was presented. Here, mediator masses between 10 and 50 GeV for scalar mediators, assuming couplings equal to unity and a dark-matter mass of 1 GeV , were excluded at 95% CL. Finally, even though the analysis

was expected to be sensitive to models with pseudoscalar mediators with masses between 10 and 100 GeV, limits could not be set for this model for the coupling assumption of $g = 1.0$ due to a small excess in the observed data.

$t\bar{t}+Z$ ESTIMATION FOR A DARK MATTER SEARCH

A

The data-driven background estimation technique, already discussed in Section 6.2, and the theory uncertainties calculation prescription presented in Section 6.3, were also used in the search for dark matter produced in association with third-generation quarks, which was published in October 2017 in the Eur. Phys. J. [168]. The author’s contribution to this analysis only regarded the $t\bar{t}+Z$ background estimation and the computation of the relevant theory uncertainties and, as such, only these two topics will be hereby covered.

A.1 Overview of the analysis

The analysis also used 36.1 fb^{-1} of pp collisions delivered by the LHC and recorded with the ATLAS detector, and it targeted final states with either bottom- or top-quark pairs and missing transverse momentum. In particular, only the final state with two top quarks and missing transverse momentum, as shown in Figure A.1, will be considered here. The 0ℓ final state of this analysis essentially yields an experimental signature identical to the one discussed in Chapter 5, namely 4 or more jets, two of which b -tagged, and missing transverse momentum. For such reason, the physics objects used in this analysis, and the variables employed for the design of a $t\bar{t}+\gamma$ CR to estimate the $t\bar{t}+Z$ background, are the same as those already extensively discussed in Chapters 5, and 6.

Five SRs are employed in this analysis: SRb1, SRb2, SRt1, SRt2, and SRt3. SRb1 and SRb2 are optimised for models in which DM is produced in association with one or two b -quarks and these will not be further considered as the author did not contribute to this part of the analysis. SRt1, SRt2, and SRt3, are optimised to isolate events in which DM is produced in association with a top-antitop pair, that either decays fully hadronically (SRt1 and SRt2) or dileptonically (SRt3) [168]. While the $t\bar{t} + Z(\rightarrow \nu\nu)$ is an irreducible background in SRt1 and SRt2, it is neg-

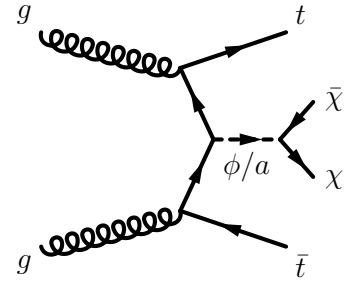


Figure A.1: Representative diagram at the lowest order for spin-0 mediator associated production with top quarks $t\bar{t}+\phi/a$ (taken from [168]).

Table A.1: Summary of the kinematic and topology-dependent selections for signal regions SRt1 and SRt2 [168]. SRt3 is not reported as it was not relevant for the estimation of the $t\bar{t}+Z$ background.

Observable	SRt1	SRt2
Trigger		E_T^{miss}
anti- k_t $R = 0.4$ jets	≥ 4 , $p_T > 80, 80, 40, 40$ GeV	
$N_{b\text{-jets}}$		≥ 2
N_ℓ		0
E_T^{miss} [GeV]		> 300
p_T leading b -jet [GeV]		> 20
$m_{\text{jet}, R=0.8}^0$ [GeV]	> 80	-
$m_{\text{jet}, R=0.8}^1$ [GeV]	> 80	-
$m_T^{b,\text{min}}$ [GeV]	> 150	> 200
$m_T^{b,\text{max}}$ [GeV]	> 250	-
$\Delta R(b, b)$		> 1.5
$E_T^{\text{miss}} / \sqrt{\sum E_T}$ [$\sqrt{\text{GeV}}$]	-	> 12
$\Delta\phi(j, \mathbf{p}_T^{\text{miss}})$ [rad]		> 0.4
$E_T^{\text{miss,track}}$ [GeV]		> 30
$\Delta\phi(\mathbf{p}_T^{\text{miss}}, \mathbf{p}_T^{\text{miss,track}})$ [rad]		$< \pi/3$

ligible in SRt3 and therefore such SR will be neglected here. SRt1 and SRt2 have a very similar background composition as the one discussed in Chapter 5 and they target low (< 100 GeV) and high (between 100 and 350 GeV) mediator mass assumptions, respectively. Table A.1 shows the SRt1 and SRt2 selections.

A.2 The estimation of the irreducible $t\bar{t}+Z$ background

As in the $t\bar{t}\ell$ analysis - the search for top squarks in all-hadronic final states presented in Chapters 5, 6, and 7 - the $t\bar{t}+V$ events, and in particular $t\bar{t}+Z$ events where the Z boson decays into neutrinos, represent an irreducible background for the SRs targeting dark matter produced in association with top quarks (Figure A.1). Once again, a data-driven approach is employed to estimate such background. In particular, events with $p_T^\gamma > m_Z$ resembling $t\bar{t} + Z(vv)$ ones are selected. The CR γ selection, detailed in Table A.2, allows to select events with exactly one energetic tight photon and at least one lepton from the decay of the $t\bar{t}$ system. Such CR essentially is identical to the one in Table 6.1 already shown in Section 6.2 (page 80), except for the applied trigger which is a single-photon instead of a 1-lepton trigger. This strategy was found to allow the CR CR γ to better mimic the hard kinematic requirements of the two SRs targeting the sig-

Table A.2: Summary of the CR γ selection for the $t\bar{t}+Z$ background estimation.

Observable	CR γ
Trigger	photon
N_{jets}	≥ 4
$N_{b-\text{jets}}$	≥ 2
N_{γ}	1
p_{T}^{γ} [GeV]	> 150
N_{ℓ}	1
$p_{\text{T}}(\ell_1)$ [GeV]	> 28

Table A.3: Background composition of $t\bar{t}+\gamma$ CR. Pre-fit yields, statistical and detector systematic uncertainties shown.

Process	Yield
$t\bar{t}+\gamma$	89.50 ± 2.02
$V + \gamma$	5.01 ± 1.12
$t\bar{t}$	4.26 ± 0.94
$t\bar{t} + V$	1.79 ± 0.23
single Top	1.86 ± 0.52
Z	0.56 ± 0.13
W	0.03 ± 0.01
Total MC	103.01 ± 2.69
Data	124
CRγ purity (87%)	
$\mu_{t\bar{t}+\gamma}$	1.22 ± 0.13

nal in Figure A.1 [168]. Finally, in order to mimic the expected missing transverse momentum spectrum of $Z \rightarrow v\bar{v}$ events, the p_{T} of the photon (p_{T}^{γ}) is vectorially added to the $\mathbf{p}_{\text{T}}^{\text{miss}}$, to form a variable called $E_{\text{T},\gamma}^{\text{miss}}$.

A.3 Results

A normalisation factor for the $t\bar{t}+Z$ SM background, $\mu_{t\bar{t}+Z} = 1.22$, was obtained by performing the background-only fit - employing the same procedure discussed in Chapter 7 - including all the SM backgrounds. Figure A.2 shows the distribution of $E_{\text{T},\gamma}^{\text{miss}}$ in CR γ where a very good data/MC agreement was found. Lastly, by employing the same procedure discussed in Section 6.3 the theory uncertainties were computed and found to be between 6% – 10% across the various SRs. Additionally, Table A.3 shows the background composition of CR γ , where an 87% purity was reached.

The data is found to be compatible with the background prediction in each one of the SRs. In particular, in each SR the observed yield in data is above the expected background but within 1.3 standard deviations of its uncertainty, too low to suggest the presence of any of the searched signal. A model-independent fit [148], where both CRs and SRs are included, is employed to derive 95% CL upper limits on the visible cross-section of new BSM processes, defined as cross-section times acceptance times efficiency ($\langle\sigma Ae\rangle_{\text{obs}}^{95\%}$) and obtained as the upper limit on the number of BSM events divided by the total integrated luminosity. No systematic uncertainties for the signal are assumed for such limits and any possible signal contamination in the CRs is neglected.

Figures A.3 and A.4 show upper limits at 95% CL on $\sigma/\sigma(g=1.0)$, namely the signal cross-section scaled to the signal cross-section for coupling $g=1$. To derive the results for the fully hadronic $t\bar{t}$ final state the region SRt1 or SRt2 with the best expected sensitivity is used. The

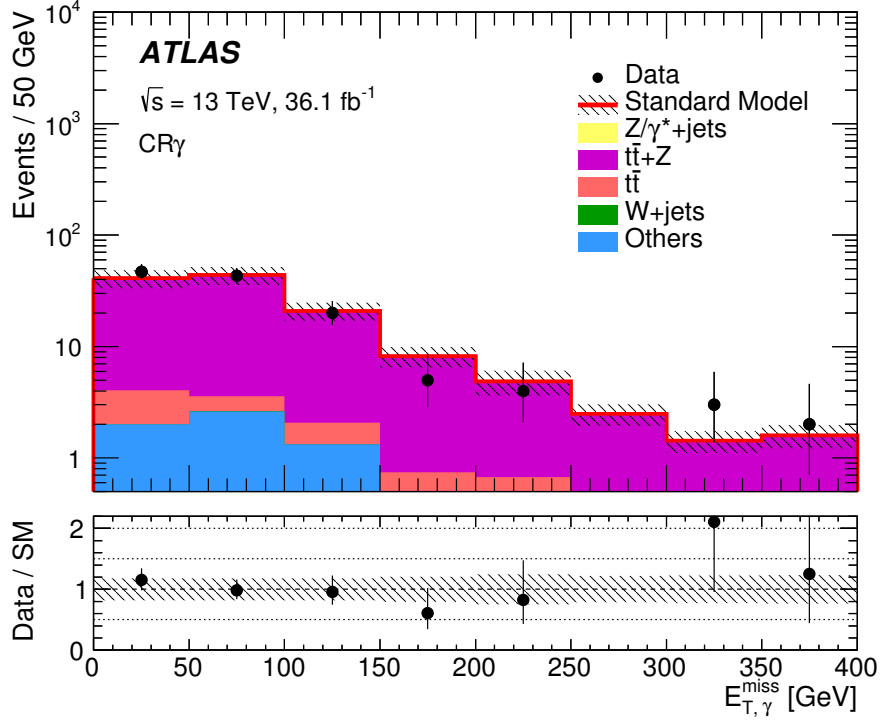


Figure A.2: Comparison of the data with the post-fit Monte Carlo prediction of the $E_{T,\gamma}^{\text{miss}}$ distribution in CR γ . The bottom panel shows the ratio of the data to the MC prediction. The band includes all systematic detector-related and theory uncertainties. The last bins include overflows, where applicable (taken from [168]).

SRt1 was originally optimised for low-mass scalar mediators, while SRt2 was optimised for high-mass scalar mediators and pseudoscalar mediators. However, SRt1 is strongly affected by systematic uncertainties in the $t\bar{t}$ modelling and therefore SRt2 sets more stringent limits for the whole parameter space. These limits are obtained both as a function of the mediator mass, assuming a specific DM mass of 1 GeV (Figure A.3), and as a function of the DM mass, assuming a specific mediator mass of 10 GeV (Figure A.4). Both the scalar and pseudoscalar mediator cases are considered. The sensitivity for $t\bar{t} + \phi/a$ on-shell decays is approximately constant for masses below 100 GeV, with SRt3 excluding the $g = 1$ assumption for scalar mediator masses up to 50 GeV. For a given mediator mass the acceptance of the analysis is independent of the value of the DM mass as long as $m(\phi/a) > 2m(\chi)$ is fulfilled. Under these conditions, exclusion limits for DM masses differing from the one presented can be inferred from the result shown in Figure A.3. Due to the smaller Yukawa enhancement of $b\bar{b} + \phi/a$ final states, it is possible to exclude cross-sections 300 times the nominal values for $g = 1$.

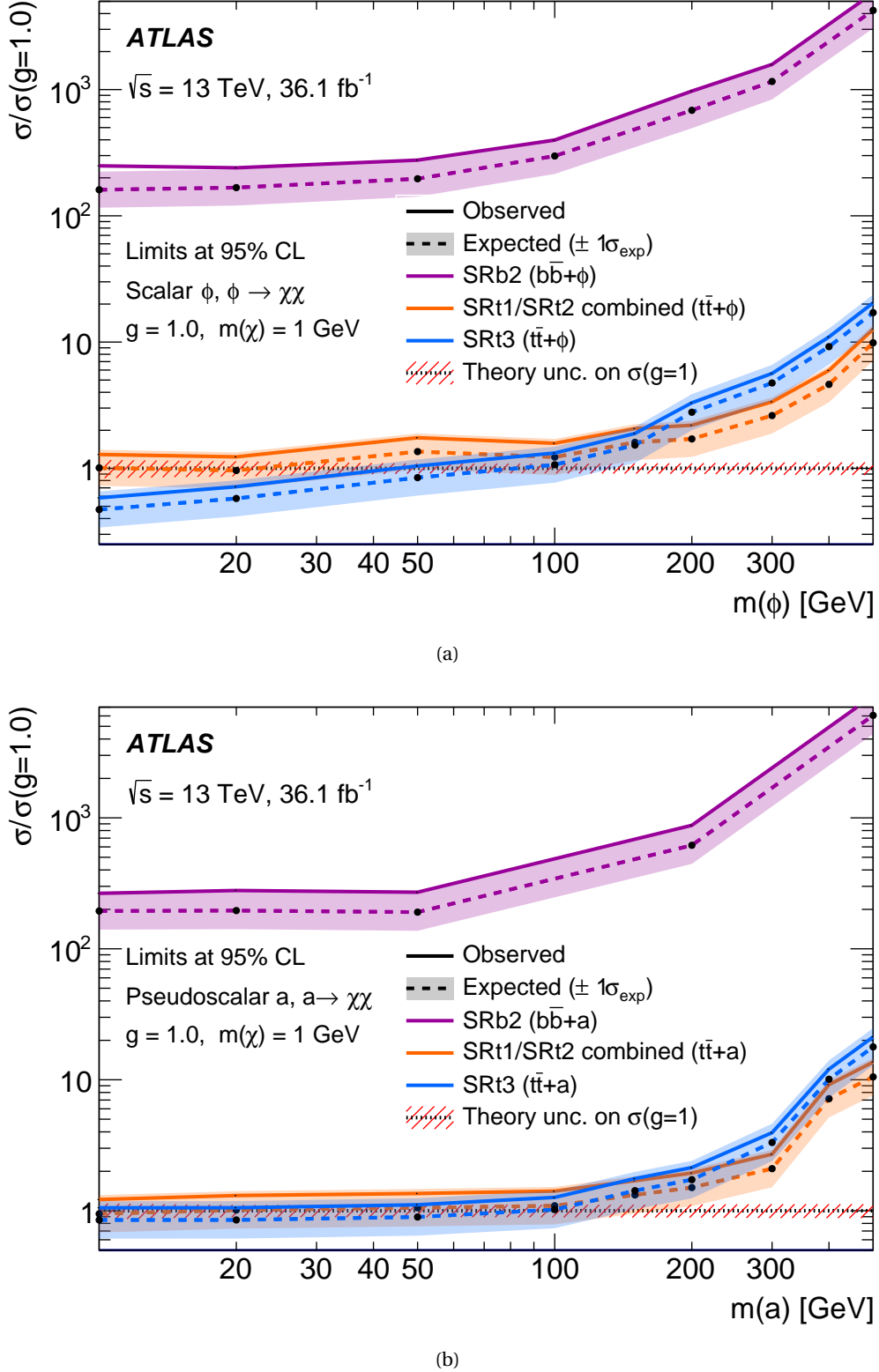


Figure A.3: Exclusion limits for colour-neutral $t\bar{t}/b\bar{b}+\phi$ scalar (a) and $t\bar{t}/b\bar{b}+a$ pseudoscalar (b) models as a function of the mediator mass for a DM mass of 1 GeV. The limits are calculated at 95% CL and are expressed in terms of the ratio of the excluded cross-section to the nominal cross-section for a coupling assumption of $g = g_q = g_\chi = 1$, where g_χ is the DM-mediator coupling, and g_q the flavour-universal SM-mediator coupling. The solid (dashed) lines shows the observed (expected) exclusion limits for the different signal regions, according to the colour code specified in the legend. To derive the results for the fully hadronic $t\bar{t}$ final state the region SRt1 or SRt2 providing the better expected sensitivity is used (taken from [168]).

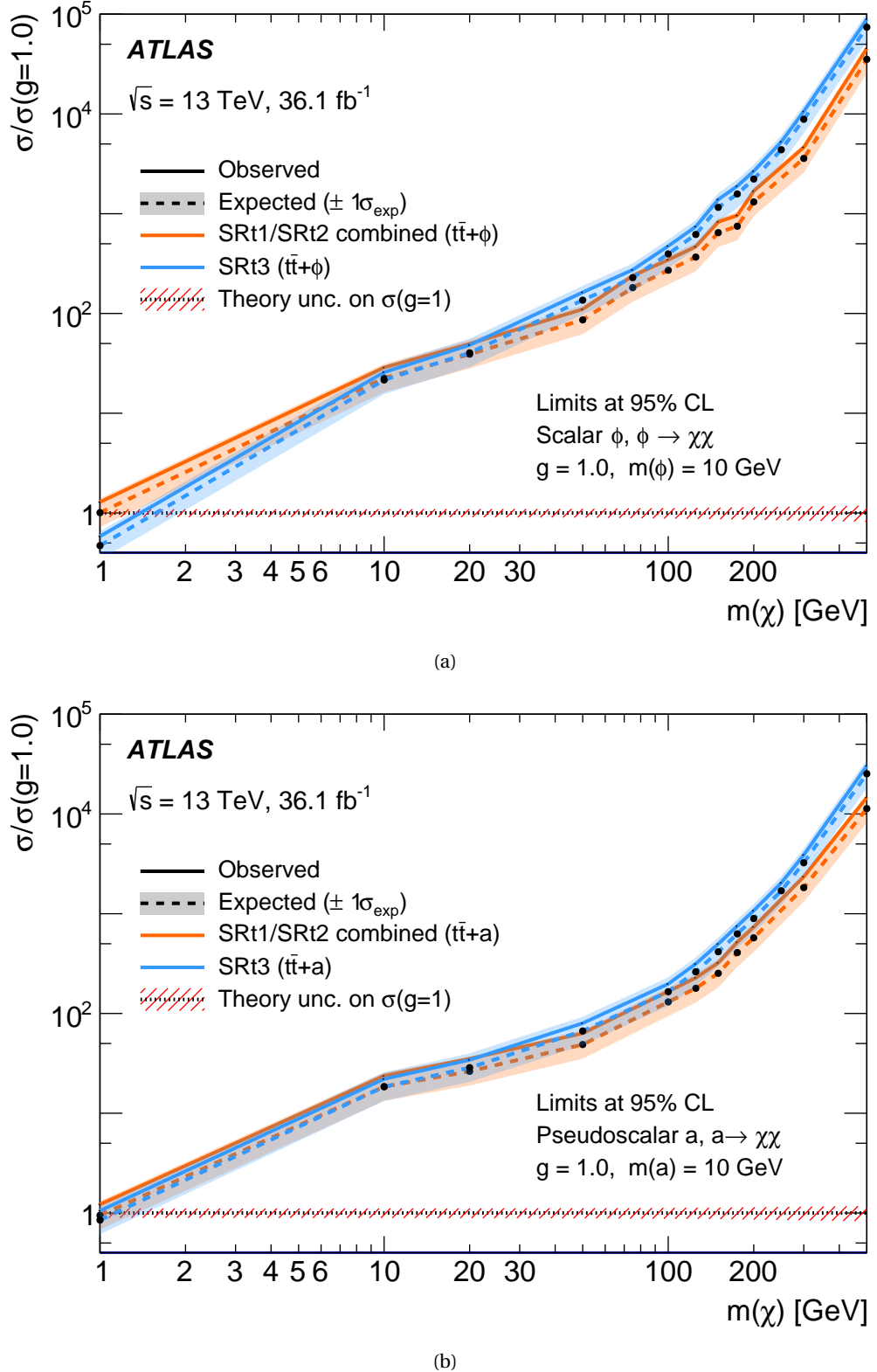


Figure A.4: Exclusion limits for colour-neutral $t\bar{t} + \phi$ scalar (a) and $t\bar{t} + a$ pseudoscalar (b) models as a function of the DM mass for a mediator mass of 10 GeV. The limits are calculated at 95% CL and are expressed in terms of the ratio of the excluded cross-section to the nominal cross-section for a coupling assumption of $g = g_q = g_\chi = 1$, where g_χ is the DM–mediator coupling, and g_q the flavour-universal SM–mediator coupling. The solid (dashed) lines shows the observed (expected) exclusion limits for the different signal regions, according to the colour code specified in the legend. To derive the results for the fully hadronic $t\bar{t}$ final state the region SRt1 or SRt2 providing the better expected sensitivity is used (taken from [168]).

SUMMARY OF THE BACKGROUND ESTIMATION

B

A summary with the all the detailed selections of the presented CRs is given in Tables B.1 (CRZ), B.2 (CRT), and B.3 (CRW and CRST). Additionally, Tables B.4, B.5, B.6 show the detailed selections for the VRs of the $Z + \text{jets}$ and $t\bar{t}$ backgrounds in SR, respectively. The details about the estimation of $t\bar{t}+Z$ are omitted as it has been extensively discussed in Section 6.2.

Table B.1: Selection criteria for the $Z + \text{jets}$ control regions used to estimate the $Z + \text{jets}$ background contributions in the SRs.

Selection	CRZAB-TT-TW	CRZAB-T0	CRZD	CRZE
Trigger		electron or muon		
N_ℓ		2 SFOS		
p_T^ℓ		$> 28 \text{ GeV}$		
$m_{\ell\ell}$		[86,96] GeV		
E_T^{miss}		$< 50 \text{ GeV}$		
$E_T^{\text{miss}'}$		$> 100 \text{ GeV}$		
N_{jet}		≥ 4		
$N_{b-\text{jet}}$		≥ 2		
$p_T^0, p_T^1, p_T^2, p_T^3$		80, 80, 40, 40 GeV		
$m_{\text{jet}, R=1.2}^0$	$> 120 \text{ GeV}$		-	
$m_{\text{jet}, R=1.2}^1$	$> 60 \text{ GeV}$	$< 60 \text{ GeV}$	-	
$m_T^{b,\text{min}'}$	-		$> 200 \text{ GeV}$	
$m_T^{b,\text{max}'}$	-		$> 200 \text{ GeV}$	-
H_T	-		$> 500 \text{ GeV}$	

Table B.2: Selection criteria for the $t\bar{t}$ CRs used to estimate the $t\bar{t}$ background contributions in the SRs.

Table B.3: Selection criteria for the $W + \text{jets}$ and single-top CR definitions.

Selection	CRW	CRST
Trigger	E_T^{miss}	
E_T^{miss}		> 250 GeV
N_ℓ		1
p_T^ℓ		> 20 GeV
N_{jet}		≥ 4 (including lepton)
$p_T^0, p_T^1, p_T^2, p_T^3$		80, 80, 40, 40 GeV
$N_{b-\text{jet}}$	1	≥ 2
$\left \Delta\phi(\text{jet}^{0,1}, \mathbf{p}_T^{\text{miss}}) \right $		> 0.4
$m_T(\ell, E_T^{\text{miss}})$		[30, 100] GeV
$\Delta R(b, \ell)_{\min}$		> 2.0
$\Delta R(b, b)$	-	> 1.5
$m_{\text{jet}, R=1.2}^0$	< 60 GeV	> 120 GeV
$m_T^{b,\min}$	-	> 200 GeV

Table B.4: Selection criteria for the Z VRs used to validate the Z background estimates in the SRs.

Selection	VRZAB	VRZD	VRZE
N_{jet}	≥ 4	≥ 5	≥ 4
Jet $p_{\text{T}}^0, p_{\text{T}}^1$	$> 80, > 80 \text{ GeV}$	$> 150, > 80 \text{ GeV}$	$> 80, > 80 \text{ GeV}$
$N_{b\text{-jet}}$		≥ 2	
τ -veto	yes		no
$m_{\text{T}}^{b,\text{min}}$		$> 200 \text{ GeV}$	
$m_{\text{T}}^{b,\text{max}}$	-	$> 200 \text{ GeV}$	-
$m_{\text{jet},R=1.2}^0$	$< 120 \text{ GeV}$		-
$m_{\text{jet},R=0.8}^0$		-	$< 120 \text{ GeV}$
$\Delta R(b, b)$	< 1.0	< 0.8	< 1.0
$E_{\text{T}}^{\text{miss}}/\sqrt{H_{\text{T}}}$		-	$> 14 \sqrt{\text{GeV}}$
H_{T}	-		$> 500 \text{ GeV}$

Table B.5: Validation region definitions, in addition to the requirements presented in Table 5.2 for VRTA and VRTB.

VRT	Selection	TT	TW	T0
	$m_{\text{jet},R=1.2}^0$		$> 120 \text{ GeV}$	
	$m_{\text{jet},R=1.2}^1$	$> 120 \text{ GeV}$	$60 - 120 \text{ GeV}$	$< 60 \text{ GeV}$
	$m_{\text{T}}^{b,\text{min}}$	$> 100, < 200 \text{ GeV}$	$> 140, < 200 \text{ GeV}$	$> 160, < 200 \text{ GeV}$
	Number of b -jets		≥ 2	
A	$m_{\text{jet},R=0.8}^0$		$> 60 \text{ GeV}$	
	$\Delta R(b, b)$	> 1		-
	$E_{\text{T}}^{\text{miss}}$	$> 300 \text{ GeV}$	$> 400 \text{ GeV}$	$> 450 \text{ GeV}$
B	$\Delta R(b, b)$		> 1.2	
	$m_{\text{T}}^{b,\text{max}}$		$> 200 \text{ GeV}$	

Table B.6: Summary of the selection for the 0-lepton top VRs VRTC, VRTD, and VRTE, in addition to the requirements presented in Table 5.2.

Selection	VRTC	VRTD	VRTE
τ -veto	-	yes	-
N_{jets}	≥ 4	≥ 5	≥ 4
jet p_T^1	-	$> 150 \text{ GeV}$	-
jet p_T^3	-	$> 80 \text{ GeV}$	-
$N_{b-\text{jets}}$	≥ 1		≥ 2
b-jet $p_T^0 + p_T^1$	-	$> 300 \text{ GeV}$	-
$m_T^{b,\text{min}}$	-	$> 100, < 200 \text{ GeV}$	
$m_T^{b,\text{max}}$	-	$> 300 \text{ GeV}$	-
$m_{\text{jet},R=0.8}^0$		-	$> 120 \text{ GeV}$
$m_{\text{jet},R=0.8}^1$		-	$> 80 \text{ GeV}$
$\Delta R(b, b)$	-	> 0.8	-
N_{jet}^S	≥ 4		-
$N_{b-\text{jet}}^S$	≥ 1		-
$p_{T,b}^{0,S}$	$\geq 40 \text{ GeV}$		-
$p_T^{4,S}$	$> 40 \text{ GeV}$		-
p_T^{ISR}	$\geq 400 \text{ GeV}$		-
m_S	$> 100 \text{ GeV}$		-
m_V/m_S	< 0.6		-
$\Delta\phi(\text{ISR}, \mathbf{p}_T^{\text{miss}})$	< 3.00		-

Table B.7: Summary of the selection for the 1-lepton $W+\text{jets}$ validation region. The signal lepton is treated as a jet. The same E_T^{miss} triggers as mentioned in Table 5.2 are used.

Selection	VRW
Number of leptons	1
Number of jets (incl. lepton)	≥ 4
p_T of jets (incl. lepton) in GeV	(80,80,40,40)
Number of b -jets	≥ 2
$\min \left \Delta\phi \left(\text{jet}^{0-1}, \mathbf{p}_T^{\text{miss}} \right) \right $	> 0.4
E_T^{miss}	$> 250 \text{ GeV}$
$m_T(\ell, E_T^{\text{miss}})$	$> 30, < 100 \text{ GeV}$
$m_{\text{jet},R=1.2}^0$	$< 70 \text{ GeV}$
$m_T^{b,\text{min}}$	150 GeV
$\Delta R(b_{0,1}, \ell)_{\text{min}}$	> 1.8

GLOSSARY

ALICE	A Large Ion Collider Experiment	20
AOD	Analysis Objects Data	
ATLAS	A Toroidal LHC ApparatuS	2
BDT	Boosted Decisions Tree	54
BR	Branching Ratio	62
BSM	Beyond Standard Model	22
CERN	European Organization for Nuclear Research	9
CKKW	Catani-Krauss-Kuhn-Webber	46
CL	Confidence Level	94
CMS	Compact Muon Solenoid	20
CM	centre-of-mass	72
CPU	Central Processing Unit	37
CR	Control Region	68
CSC	Cathode Strip Chamber	30
CTP	Central Trigger Processor	32
DIS	Deep Inelastic Scattering	44
DM	Dark Matter	11
ECAL	Electromagnetic Calorimeter	24
EM	electromagnetic	50
ESD	Event Summary Data	
FCNC	Flavour Changing Neutral Currents	16
FoM	Figure of Merit	68
FSR	Final State Radiation	44
FTF	Fast Track Finder	37

FTK	Fast TracKer	31
GUT	Grand Unification Theory	11
HCAL	Hadronic Calorimeter	28
HEP	High-Energy Physics	46
HLT	High Level Trigger	31
IBL	Insertable B-Layer	25
ID	Inner Detector	23
ISR	Initial State Radiation	44
JES	Jet Energy Scale	53
JER	Jet Energy Resolution	84
JVT	Jet vertex Tagger	54
L1	Level-1	31
L1Calo	L1 Calorimeter	32
L1Muon	L1 Muon	32
L1Topo	Level-1 Topological	34
LAr	Liquid Argon	28
LEIR	Low Energy Ion Ring	22
LEP	Large Electron-Positron Collider	9
LH	Likelihood	49
LHC	Large Hadron Collider	1
LHCb	Large Hadron Collider beauty	20
LHCf	Large Hadron Collider forward	22
LINAC2	Linear Accelerator 2	21
LINAC3	Linear Accelerator 3	22
LO	Leading Order	45
LS1	Long Shut down 1	21
LSP	Lightest Supersymmetric Particle	15
MC	Monte Carlo	43
ME	Matrix Element	45
MDT	Monitored Drift Tube	30
MIP	Minimum Ionising Particle	51
MLE	Maximum Likelihood Estimation	91
MLM	Michelangelo L. Mangano	46

MoEDAL	Monopole & Exotics Detector At the LHC	22
MS	Muon Spectrometer	23
MSSM	Minimal Supersymmetric Standard Model.....	3
MV2	Multivariate algorithm.....	54
NLO	Next-to-Leading Order	45
NLSP	Next Lightest Supersymmetric Particle	18
OR	Overlap Removal.....	59
PDF	Parton Distribution Function.....	44
PLR	Profile Likelihood Ratio.....	93
pMSSM	Phenomenological MSSM	16
PS	Parton Shower	46
PSB	Proton Synchrotron Booster.....	21
PV	Primary Vertex.....	26
QCD	Quantum Chromodynamics.....	6
QED	Quantum Electrodynamics	4
QFT	Quantum Field Theory.....	4
RDO	Raw Data Object	
RJR	Recursive Jigsaw Technique	72
ROI	Region of Interest	32
ROS	Read-Out System	32
RPC	<i>R</i> -Parity Conserving	31
RPC	Resistive-Plate Chamber.....	31
SCT	SemiConductor Tracker	23
SF	Scale Factor	86
SFOS	Same Flavour Opposite Sign	77
SM	Standard Model	1
SPS	Super Proton Synchrotron.....	21
SR	Signal Region	ii
SUSY	Supersymmetry.....	1
SV	Secondary Vertex	25
TDAQ	Trigger and Data Acquisition	32
TF	Transfer Factor.....	77
TGC	Thin-Gap Chamber	30

TOTEM	TOTal cross section, Elastic scattering and diffraction dissociation Measurement at the LHC	22
TRT	Transition Radiation Tracker	23
UE	Underlying Event	44
VEV	Vacuum Expectation Value	8
VR	Validation Region	68
WIMP	Weakly Interacting Massive Particle	11
WP	Working Point	49

BIBLIOGRAPHY

- [1] W. Thompson, *Angular Momentum: An Illustrated Guide to Rotational Symmetries for Physical Systems*. No. v. 1 in A Wiley-Interscience publication. Wiley, 1994.
<https://books.google.co.uk/books?id=025fXV4z0B0C>.
- [2] The ATLAS Collaboration, *Observation of a New Particle in the Search for the Standard Model Higgs Boson with the ATLAS Detector at the LHC*, Phys.Lett. **B716** (2012), arXiv:1207.7214 [hep-ex].
- [3] CMS Collaboration, *Observation of a new boson at a mass of 125 GeV with the CMS experiment at the LHC*, Phys.Lett. **B716** (2012), arXiv:1207.7235 [hep-ex].
- [4] The ATLAS Collaboration, *Search for a scalar partner of the top quark in the jets plus missing transverse momentum final state at $\sqrt{s}=13$ TeV with the ATLAS detector.*,
- [5] M. Herrero, *The Standard Model*, <https://arxiv.org/abs/hep-ph/9812242>.
- [6] M. E. Peskin, D. V. Schroeder, *An Introduction to Quantum Field Theory*. Westview Press, 1995.
- [7] W. N. Cottingham and D. A. Greenwod, *An introduction to the standard model*. Cambridge, 1998.
- [8] L. Lederman and C. Hill, *Symmetry and the Beautiful Universe*. Prometheus Books, 2004. <https://books.google.co.uk/books?id=X2QPAQAAQAAJ>.
- [9] A. Pich, *The Standard Model of Electroweak Interactions*, arXiv:1201.0537 [hep-ph].
- [10] Particle Data Group Collaboration, C. Patrignani et al., *Review of Particle Physics*, Chin. Phys. **C40** no. 10, (2016) 100001.
- [11] S. Weinberg, *The quantum theory of fields. Vol. 2: Modern applications*. Cambridge University Press, 2013.
- [12] S. L. Glashow, *Partial Symmetries of Weak Interactions*, Nucl. Phys. **22** (1961) 579–588.

- [13] A. Salam and J. Ward, *Electromagnetic and weak interactions*, Physics Letters **13** no. 2, (1964) 168 – 171.
<http://www.sciencedirect.com/science/article/pii/0031916364907115>.
- [14] S. Weinberg, *A Model of Leptons*, Phys. Rev. Lett. **19** (1967) 1264–1266.
<https://link.aps.org/doi/10.1103/PhysRevLett.19.1264>.
- [15] P. W. Higgs, *Broken Symmetries and the Masses of Gauge Bosons*, Phys. Rev. Lett. **13** (1964) 508–509.
- [16] J. Goldstone, A. Salam and S. Weinberg, *Broken Symmetries*, Phys. Rev. **127** (1962) 965–970.
- [17] ATLAS Collaboration, “Summary plots from the ATLAS Standard Model physics group.”
https://atlas.web.cern.ch/Atlas/GROUPS/PHYSICS/CombinedSummaryPlots/SM/ATLAS_a_SMSummary_TotalXsect/ATLAS_a_SMSummary_TotalXsect.png.
- [18] S. Weinberg, *Implications of Dynamical Symmetry Breaking*, Phys. Rev. **D19** (1976) 1277–1280.
- [19] Super-Kamiokande Collaboration, Y. Fukuda et al., *Evidence for oscillation of atmospheric neutrinos*, Phys. Rev. Lett. **81** (1998) 1562–1567, arXiv:hep-ex/9807003 [hep-ex].
- [20] SNO Collaboration, *Measurement of the Rate of $\nu_e + d \rightarrow p + p + e^-$ Interactions Produced by 8B Solar Neutrinos at the Sudbury Neutrino Observatory*, Phys. Rev. Lett. **87** (2001).
- [21] The official website of the Nobel Prize.
https://www.nobelprize.org/nobel_prizes/physics/laureates/2015/.
- [22] E. Kh. Akhmedov, et. al, *Seesaw mechanism and structure of neutrino mass matrix*, Phys. Lett. **B478** (1999).
- [23] V. C. Rubin and W. K. Ford, Jr., *Rotation of the Andromeda Nebula from a Spectroscopic Survey of Emission Regions*, Astrophysical Journal **159** (1970) 379.
- [24] M. H. Jones, R. J. A. Lambourne, and S. Serjeant, *An Introduction to Galaxies and Cosmology (2nd ed)*. Cambridge University Press/Open University, Cambridge, January, 2015. <http://oro.open.ac.uk/44361/>.
- [25] S. P. Martin, *A Supersymmetry primer*, arXiv:hep-ph/9709356 [hep-ph]. [Adv. Ser. Direct. High Energy Phys.18,1(1998)].
- [26] R. Barbieri and G. F. Giudice, *Upper Bounds on Supersymmetric Particle Masses*, Nucl. Phys. **B306** (1988) 63–76.
- [27] F. Jegerlehner, *The hierarchy problem of the electroweak Standard Model revisited*, arXiv:1305.6652 [hep-ph].

- [28] H. E. Haber and G. L. Kane, *The Search for Supersymmetry: Probing Physics Beyond the Standard Model*, Phys. Rept. **117** (1985) 75–263.
- [29] K. Hidaka and A. Bartl, *Impact of bosonic decays on the search for the lighter stop and sbottom squarks*, Phys. Lett. **B501** (2001) 78–85, arXiv:hep-ph/0012021 [hep-ph].
- [30] C. Borschensky, M. Kramer, A. Kulesza, M. Mangano, S. Padhi, T. Plehn, and X. Portell, *Squark and gluino production cross sections in pp collisions at $\sqrt{s} = 13, 14, 33$ and 100 TeV*, Eur. Phys. J. C **74** (2014) 3174, arXiv:1407.5066 [hep-ph].
- [31] O. S. Brüning, P. Collier, P. Lebrun, S. Myers, R. Ostojic, J. Poole and P. Proudlock, *LHC Design Report*, <https://cds.cern.ch/record/782076>.
- [32] J.M. Jowett, M. Schaumann, R. Alemany, R. Bruce, M. Giovannozzi, P. Hermes, W. Hofle, M. Lamont, T. Mertens, S. Redaelli, J. Uythoven, J. Wenninger, *The 2015 Heavy-Ion Run of the LHC*, <http://accelconf.web.cern.ch/accelconf/ipac2016/papers/tupmw027.pdf>.
- [33] C. Lefèvre, *The CERN accelerator complex*, <http://cds.cern.ch/record/1260465>.
- [34] The ATLAS Collaboration, *The ATLAS experiment at the CERN Large Hadron Collider*, Journal of Instrumentation **3** no. 08, (2008) S08003. <http://stacks.iop.org/1748-0221/3/i=08/a=S08003>.
- [35] CMS Collaboration, *The CMS experiment at the CERN LHC*, Journal of Instrumentation **3** no. 08, (2008) S08004. <http://stacks.iop.org/1748-0221/3/i=08/a=S08004>.
- [36] LHCb Collaboration, *The LHCb Detector at the LHC*, JINST (2008).
- [37] ALICE Collaboration, *The ALICE experiment at the CERN LHC*, Journal of Instrumentation **3** no. 08, (2008) S08002. <http://stacks.iop.org/1748-0221/3/i=08/a=S08002>.
- [38] TOTEM Collaboration, *The TOTEM Experiment at the CERN Large Hadron Collider*, Journal of Instrumentation **3** no. 08, (2008) S08007. <http://stacks.iop.org/1748-0221/3/i=08/a=S08007>.
- [39] LHCf Collaboration, *LHCf experiment: Technical Design Report*. Technical Design Report LHCf. CERN, Geneva, 2006. <http://cds.cern.ch/record/926196>.
- [40] J. Pinfold, *The MoEDAL experiment at the LHC*, EPJ Web Conf. **145** (2017) 12002.
- [41] A. Yamamoto, Y. Makida, R. Ruber, Y. Doi, T. Haruyama, F. Haug, H. ten Kate, M. Kawai, T. Kondo, Y. Kondo, J. Metselaar, S. Mizumaki, G. Olesen, O. Pavlov, S. Ravat, E. Sbrissa, K. Tanaka, T. Taylor, and H. Yamaoka, *The ATLAS central solenoid*, Nuclear Instruments and Methods in Physics Research Section A: Accelerators, Spectrometers, Detectors and Associated Equipment **584** no. 1, (2008) 53 – 74. <http://www.sciencedirect.com/science/article/pii/S0168900207020414>.

- [42] The ATLAS Collaboration, *The ATLAS Inner Detector commissioning and calibration*, Eur. Phys. JC**70**, arXiv:1004.5293.
- [43] The ATLAS Collaboration, *ATLAS Insertable B-Layer Technical Design Report*, <https://cds.cern.ch/record/1291633>.
- [44] G. A. et al., *ATLAS pixel detector electronics and sensors*, Journal of Instrumentation **3** no. 07, (2008) P07007. <http://stacks.iop.org/1748-0221/3/i=07/a=P07007>.
- [45] A. Bingül, *The ATLAS TRT and its Performance at LHC*, Journal of Physics: Conference Series **347** no. 1, (2012) 012025. <http://iopscience.iop.org/article/10.1088/1742-6596/347/1/012025/meta>.
- [46] The ATLAS Collaboration, *Studies of the performance of the ATLAS detector using cosmic-ray muons*, The European Physical Journal C **71** no. 3, (2011) 1593. <https://doi.org/10.1140/epjc/s10052-011-1593-6>.
- [47] The ATLAS Collaboration, *ATLAS liquid-argon calorimeter: Technical Design Report*, <https://cds.cern.ch/record/331061>.
- [48] The ATLAS Collaboration, *ATLAS muon spectrometer: Technical design report*, <https://cds.cern.ch/record/331068>.
- [49] The ATLAS Collaboration, *Fast TrackEr (FTK) Technical Design Report*, <https://cds.cern.ch/record/1552953>.
- [50] The ATLAS Collaboration, *Performance of the ATLAS Trigger System in 2015*, Eur. Phys. J. C**77** (2017), arXiv:1611.09661 [hep-ex].
- [51] E. Simoni, *The Topological Processor for the future ATLAS Level-1 Trigger: from design to commissioning*, arXiv:1406.4316.
- [52] The ATLAS Collaboration, *Performance of the ATLAS Trigger System in 2010*, Eur. Phys. J C**72** (2012), arXiv:1110.1530 [hep-ex].
- [53] The ATLAS Collaboration, *The ATLAS Level-1 Calorimeter Trigger*, Journal of Instrumentation **3** no. 03, (2008) P03001. <http://stacks.iop.org/1748-0221/3/i=03/a=P03001>.
- [54] The ATLAS Collaboration, *Expected Performance of the ATLAS Experiment - Detector, Trigger and Physics*, arXiv:0901.0512 [hep-ex].
- [55] F. Miano for the ATLAS Collaboration, *The design and performance of the ATLAS Inner Detector trigger for Run 2 LHC collisions at $\sqrt{s} = 13$ TeV*, PoS **ICHEP2016** (2016) 856.
- [56] The ATLAS Collaboration, *Performance of primary vertex reconstruction in proton-proton collisions at $\sqrt{s} = 7$ TeV in the ATLAS experiment*, tech. rep., CERN.

- [57] N. Ruthmann, Y. Nakahama, and C. Leonidopoulos, *Trigger Menu in 2016*, Tech. Rep. ATL-COM-DAQ-2016-137, CERN, Geneva, Sep, 2016.
<https://cds.cern.ch/record/2216366>.
- [58] The ATLAS Collaboration, “Missing energy trigger public results.” <https://twiki.cern.ch/twiki/bin/view/AtlasPublic/MissingEtTriggerPublicResults>.
- [59] W. Lukas, *Fast Simulation for ATLAS: Atlfast-II and ISF*, J. Phys.: Conf. Ser **396** no. 022031, (2012).
- [60] The ATLAS Collaboration, *ATLAS Computing : technical design report.*,
<https://cds.cern.ch/record/837738>.
- [61] G. Barrand, et. al, *GAUDI - A software architecture and framework for building HEP data processing applications.*, [http://dx.doi.org/10.1016/S0010-4655\(01\)00254-5](http://dx.doi.org/10.1016/S0010-4655(01)00254-5).
- [62] A. Buckley et al., *General-purpose event generators for LHC physics*, Phys. Rept. **504** (2011) 145–233, arXiv:1101.2599 [hep-ph].
- [63] R. P. Feynman, *Very High-Energy Collisions of Hadrons*, Phys. Rev. Lett. **23** (1969) 1415–1417. <https://link.aps.org/doi/10.1103/PhysRevLett.23.1415>.
- [64] T.-M. Yan and S. D. Drell, *The Parton Model and its Applications*, Int. J. Mod. Phys. **A29** (2014) 0071, arXiv:1409.0051 [hep-ph].
- [65] J. D. Bjorken, *Asymptotic Sum Rules at Infinite Momentum*, Phys. Rev. **179** (1969) 1547–1553. <https://link.aps.org/doi/10.1103/PhysRev.179.1547>.
- [66] M. Dobbs and J. B. Hansen, *The HepMC C++ Monte Carlo event record for High Energy Physics*, Computer Physics Communications **134** no. 1, (2001) 41 – 46.
<http://www.sciencedirect.com/science/article/pii/S0010465500001892>.
- [67] ZEUS, H1 Collaboration, F D. Aaron et al., *Combined Measurement and QCD Analysis of the Inclusive ep Scattering Cross Sections at HERA*, JHEP **01** (2010) 109, arXiv:0911.0884 [hep-ex].
- [68] J. M. Campbell, J. Houston and W. Stirling, *Hard Interactions of Quarks and Gluons: A Primer of LHC Physics*, Rept. Prog. Phys **70** no. 1, (2007).
- [69] V. N. Gribov and L. N. Lipatov, *Deep inelastic e p scattering in perturbation theory*, Sov. J. Nucl. Phys. **15** (1972) 438–450. [Yad. Fiz.15,781(1972)].
- [70] G. Altarelli and G. Parisi, *Asymptotic Freedom in Parton Language*, Nucl. Phys. **B126** (1977) 298–318.
- [71] CTEQ Collaboration, J. Botts, J. G. Morfin, J. F. Owens, J.-w. Qiu, W.-K. Tung, and H. Weerts, *CTEQ parton distributions and flavor dependence of sea quarks*, Phys. Lett. **B304** (1993) 159–166, arXiv:hep-ph/9303255 [hep-ph].

- [72] G. Corcella, et al., *HERWIG 6: an event generator of hadron emission reactions with interfering gluons (including supersymmetric processes)*, J. High Energy Phys. **JHEP(2001)** (2001).
- [http://iopscience.iop.org/article/10.1088/1126-6708/2001/01/010/meta.](http://iopscience.iop.org/article/10.1088/1126-6708/2001/01/010/meta)
- [73] Torbjörn Sjöstrand and Stephen Mrenna and Peter Skands, *PYTHIA 6.4 physics and manual*, Journal of High Energy Physics **2006** no. 05, (2006) 026.
<http://stacks.iop.org/1126-6708/2006/i=05/a=026>.
- [74] T. Gleisberg et al., *Event generation with SHERPA 1.1*, JHEP **02** (2009) 007.
- [75] Bernd A. Berg, *Introduction to Markov Chain Monte Carlo Simulations and their Statistical Analysis*, arXiv:cond-mat/0410490 [cond-mat].
- [76] S. Catani, F. Krauss, R. Kuhn and B. Webber, *QCD Matrix Elements + Parton Showers*, JHEP 0111 (2001), arXiv:hep-ph/0109231 [hep-ph].
- [77] M. L. Mangano, M. Moretti and R. Pittau, *Multijet Matrix Elements and Shower Evolution in Hadronic Collisions: $Wb\bar{b} + n$ Jets as a Case Study*, Nucl.Phys **B632** (2001), arXiv:0108069 [hep-ph].
- [78] A. Kupco , *Cluster Hadronization in HERWIG 5.9*, arXiv:hep-ph/9906412 [hep-ph].
- [79] B. Andersson, S. Mohanty and F. Soderberg, *Recent Developments in the Lund Model*, arXiv:hep-ph/0212122 [hep-ph].
- [80] R. D. Field, *The Underlying Event in Hard Scattering Processes*, arXiv:hep-ph/0201192 [hep-ph].
- [81] GEANT4 Collaboration, *Geant4 a simulation toolkit*, Nucl. Instrum. Meth. A **506** (2003).
- [82] *Vertex Reconstruction Performance of the ATLAS Detector at " \sqrt{s} = 13 TeV"*, Tech. Rep. ATL-PHYS-PUB-2015-026, CERN, Geneva, Jul, 2015.
<https://cds.cern.ch/record/2037717>.
- [83] R. Frühwirth, W. Waltenberger, and P. Vanlaer, *Adaptive vertex fitting*, J. Phys. **G34** (2007) N343.
- [84] The ATLAS Collaboration, *Electron and photon energy calibration with the ATLAS detector using data collected in 2015 at \sqrt{s} = 13 TeV*, tech. rep., CERN.
- [85] G. Aad et al., *Electron and photon energy calibration with the ATLAS detector using LHC Run 1 data,*
- [86] The ATLAS collaboration, *Electron efficiency measurements with the ATLAS detector using the 2015 LHC proton-proton collision data.*

- [87] The ATLAS Collaboration, “Electron and photon performance public results.” <https://twiki.cern.ch/twiki/bin/view/AtlasPublic/ ElectronGammaPublicCollisionResults>.
- [88] ATLAS Collaboration, The ATLAS Collaboration, *Measurement of the photon identification efficiencies with the ATLAS detector using LHC Run-1 data*, Eur. Phys. J. **C76** no. 12, (2016) 666, arXiv:1606.01813 [hep-ex].
- [89] The ATLAS Collaboration Collaboration, *Photon identification in 2015 ATLAS data*, Tech. Rep. ATL-PHYS-PUB-2016-014, CERN, Geneva, Aug, 2016. <https://cds.cern.ch/record/2203125>.
- [90] The ATLAS Collaboration, *Muon reconstruction performance of the ATLAS detector in proton–proton collision data at $\sqrt{s} = 13$ TeV.*
- [91] The ATLAS Collaboration, “Atlas muon combined performance with the full 2016 dataset.” <https://atlas.web.cern.ch/Atlas/GROUPS/PHYSICS/PLOTS/MUON-2017-001/index.html>.
- [92] The ATLAS Collaboration, *Electron reconstruction and identification efficiency measurements with the ATLAS detector using the 2011 LHC proton-proton collision data*, Eur. Phys. J. **74** no. 7, (2014), arXiv:1404.2240 [hep-ex].
- [93] W. Lampl, et al., *Calorimeter Clustering Algorithms: Description and Performance*, <https://cds.cern.ch/record/1099735>.
- [94] THe ATLAS Collaboration, *Topological cell clustering in the ATLAS calorimeters and its performance in LHC Run 1.*
- [95] The ATLAS Collaboration, *Properties of Jets and Inputs to Jet Reconstruction and Calibration with the ATLAS Detector Using Proton-Proton Collisions at $\sqrt{s} = 7$ TeV.* <http://cds.cern.ch/record/1281310/files/ATLAS-CONF-2010-053.pdf>.
- [96] G. S. M. Cacciari, G. P. Salam, *The Anti- $k(t)$ jet clustering algorithm*, JHEP **0804** (2008), arXiv:0802.1189 [hep-ph].
- [97] The ATLAS Collaboration, *Jet Calibration and Systematic Uncertainties for Jets Reconstructed in the ATLAS Detector at $\sqrt{s} = 13$ TeV*, Tech. Rep. ATL-PHYS-PUB-2015-015, CERN, Geneva, Jul, 2015. <https://cds.cern.ch/record/2037613>.
- [98] The ATLAS collaboration, *Pile-up subtraction and suppression for jets in ATLAS.*
- [99] The ATLAS collaboration, *Jet global sequential corrections with the ATLAS detector in proton-proton collisions at $\text{sqrt}(s) = 8$ TeV,*

- [100] The ATLAS collaboration, *Data-driven determination of the energy scale and resolution of jets reconstructed in the ATLAS calorimeters using dijet and multijet events at $\sqrt{s} = 8 \text{ TeV}$* , Tech. Rep. ATLAS-CONF-2015-017, CERN, Geneva, Apr, 2015.
<https://cds.cern.ch/record/2008678>.
- [101] The ATLAS Collaboration, *Tagging and suppression of pileup jets with the ATLAS detector*, Tech. Rep. ATLAS-CONF-2014-018, CERN, Geneva, May, 2014.
<https://cds.cern.ch/record/1700870>.
- [102] The ATLAS Collaboration, *Identification and rejection of pile-up jets at high pseudorapidity with the ATLAS detector*,.
- [103] N. Bartosik, *Diagram showing the common principle of identification of jets initiated by b-hadron decays*, 2016. http://bartosik.pp.ua/hep_sketches/btagging.
- [104] The ATLAS Collaboration, *Performance of b-Jet Identification in the ATLAS Experiment*,.
- [105] The ATLAS Collaboration, *Performance and Calibration of the JetFitterCharm Algorithm for c-Jet Identification*, Tech. Rep. ATL-PHYS-PUB-2015-001, CERN, Geneva, Jan, 2015.
<http://cds.cern.ch/record/1980463>.
- [106] M. Lehmacher, *b-Tagging Algorithms and their Performance at ATLAS*, Tech. Rep. ATL-PHYS-PROC-2008-052. ATL-COM-PHYS-2008-152, CERN, Geneva, Jul, 2008.
<http://cds.cern.ch/record/1128662>.
- [107] The ATLAS Collaboration, *Secondary vertex finding for jet flavour identification, with the ATLAS detector*, tech. rep., CERN.
- [108] G. Piacquadio and C. Weiser, *A new inclusive secondary vertex algorithm for b-jet tagging in ATLAS*, Journal of Physics: Conference Series **119** no. 3, (2008) 032032.
<http://stacks.iop.org/1742-6596/119/i=3/a=032032>.
- [109] L. Breiman et al., *Classification and Regression Trees*. Chapman & Hall, New York, 1984.
<http://www.crcpress.com/catalog/C4841.htm>.
- [110] R. Brun and F. Rademakers, *ROOT: An object oriented data analysis framework*, Nucl. Instrum. Meth. **A389** (1997) 81–86.
- [111] A. Hoecker, P. Speckmayer, J. Stelzer, J. Therhaag, E. von Toerne, H. Voss, M. Backes, T. Carli, O. Cohen, A. Christov, D. Dannheim, K. Danielowski, S. Henrot-Versille, M. Jachowski, K. Kraszewski, A. Krasznahorkay, Jr., M. Kruk, Y. Mahalalel, R. Ospanov, X. Prudent, A. Robert, D. Schouten, F. Tegenfeldt, A. Voigt, K. Voss, M. Wolter, and A. Zemla, *TMVA - Toolkit for Multivariate Data Analysis*, ArXiv Physics e-prints (2007), [physics/0703039](https://arxiv.org/abs/physics/0703039).
- [112] ATLAS Collaboration, *Optimisation of the ATLAS b-tagging performance for the 2016 LHC Run*, Tech. Rep. ATL-PHYS-PUB-2016-012, CERN, Geneva, Jun, 2016.
<https://cds.cern.ch/record/2160731>.

- [113] The ATLAS Collaboration, “ATLAS Event Displays from papers.” <https://twiki.cern.ch/twiki/bin/view/AtlasPublic/EventDisplayPapers>.
- [114] The ATLAS Collaboration, *Performance of missing transverse momentum reconstruction for the ATLAS detector in the first proton-proton collisions at $\sqrt{s} = 13 \text{ TeV}$* , Tech. Rep. ATL-PHYS-PUB-2015-027, CERN, Geneva, Jul, 2015. <http://cds.cern.ch/record/2037904>.
- [115] J. Alwall, M.-P. Le, M. Lisanti, and J. G. Wacker, *Searching for directly decaying gluinos at the Tevatron*, Phys. Lett. B **666** (2008) 34–37, arXiv:0803.0019 [hep-ph].
- [116] J. Alwall, P. Schuster, and N. Toro, *Simplified models for a first characterization of new physics at the LHC*, Phys. Rev. D **79** (2009) 075020, arXiv:0810.3921 [hep-ph].
- [117] LHC New Physics Working Group Collaboration, D. Alves, *Simplified models for LHC new physics searches*, J. Phys. G **39** (2012) 105005, arXiv:1105.2838 [hep-ph].
- [118] A. Djouadi et al., *The Minimal supersymmetric standard model: Group summary report*, arXiv:9901246 [hep-ph].
- [119] C. F. Berger, J. S. Gainer, J. L. Hewett, and T. G. Rizzo, *Supersymmetry without prejudice*, JHEP **02** (2009) 023, arXiv:0812.0980 [hep-ph].
- [120] J. Alwall, R. Frederix, S. Frixione, V. Hirschi, F. Maltoni, O. Mattelaer, H. S. Shao, T. Stelzer, P. Torrielli, and M. Zaro, *The automated computation of tree-level and next-to-leading order differential cross sections, and their matching to parton shower simulations*, JHEP **07** (2014) 079, arXiv:1405.0301 [hep-ph].
- [121] T. Sjöstrand, S. Mrenna, and P. Z. Skands, *A brief introduction to PYTHIA 8.1*, Comput. Phys. Commun. **178** (2008) 852–867, arXiv:0710.3820 [hep-ph].
- [122] D. J. Lange, *The EvtGen particle decay simulation package*, Nucl. Instrum. Meth. **462** no. 1–2, (2001) 152 – 155.
- [123] R. D. Ball et al., *Parton distributions with LHC data*, Nucl. Phys. B **867** (2013) 244–289, arXiv:1207.1303 [hep-ph].
- [124] H.-L. Lai, M. Guzzi, J. Huston, Z. Li, P. M. Nadolsky, J. Pumplin, and C. P. Yuan, *New parton distributions for collider physics*, Phys. Rev. D **82** (2010) 074024, arXiv:1007.2241 [hep-ph].
- [125] L. Lönnblad and S. Prestel, *Merging multi-leg NLO matrix elements with parton showers*, JHEP **03** (2013) 166, arXiv:1211.7278 [hep-ph].
- [126] W. Beenakker, M. Kramer, T. Plehn, M. Spira, and P. M. Zerwas, *Stop production at hadron colliders*, Nucl. Phys. **B515** (1998) 3–14, hep-ph/9710451.

- [127] W. Beenakker, S. Brensing, M. Kramer, A. Kulesza, E. Laenen, and I. Niessen, *Supersymmetric top and bottom squark production at hadron colliders*, JHEP **1008** (2010) 098, arXiv:1006.4771 [hep-ph].
- [128] W. Beenakker, S. Brensing, M. Kramer, A. Kulesza, E. Laenen, et al., *Squark and gluino hadroproduction*, Int.J.Mod.Phys. **A26** (2011) 2637–2664, arXiv:1105.1110 [hep-ph].
- [129] B. Allanach, *SOFTSUSY: a program for calculating supersymmetric spectra*, Comput. Phys. Commun. **143** (2002) 305–331, arXiv:hep-ph/0104145.
- [130] B. Allanach, P. Athron, L. C. Tunstall, A. Voigt, and A. Williams, *Next-to-minimal SOFTSUSY*, Comput. Phys. Commun. **185** (2014) 2322–2339, arXiv:1311.7659 [hep-ph].
- [131] A. Djouadi, J. Kalinowski and M. Spira, *HDECAY: A Program for Higgs boson decays in the standard model and its supersymmetric extension*, Comput. Phys. Commun. **108** (1998) 56, arXiv:9704448 [hep-ph].
- [132] A. Djouadi, M. Muhlleitner and M. Spira, *Decays of supersymmetric particles: The Program SUSY-HIT (SUspect-SdecaY-Hdecay-InTerface)*, Acta. Phys. Polon. B **38** (2007) 635–644, arXiv:0609292 [hep-ph].
- [133] The ATLAS Collaboration, *Electron efficiency measurements with the ATLAS detector using 2012 LHC proton–proton collision data*.
- [134] The ATLAS Collaboration, *Electron identification measurements in ATLAS using $\sqrt{s} = 13$ TeV data with 50 ns bunch spacing*. <https://cds.cern.ch/record/2048202>.
- [135] The ATLAS Collaboration, *Muon reconstruction performance of the ATLAS detector in proton–proton collision data at $\sqrt{s} = 13$ TeV*.
- [136] The ATLAS Collaboration, *Search for direct pair production of the top squark in all-hadronic final states in proton–proton collisions at $\sqrt{s} = 8$ TeV with the ATLAS detector*, JHEP **09** (2014) 015, arXiv:1406.1122 [hep-ex].
- [137] S. Alioli, P. Nason, C. Oleari, and E. Re, *A general framework for implementing NLO calculations in shower Monte Carlo programs: the POWHEG BOX*, JHEP **06** (2010) 043, arXiv:1002.2581 [hep-ph].
- [138] A. Barr, C. Lester, and P. Stephens, *$m(T2)$: The Truth behind the glamour*, J. Phys. **G29** (2003) 2343–2363, arXiv:hep-ph/0304226 [hep-ph].
- [139] C. Lester and D. Summers, *Measuring masses of semi-invisibly decaying particle pairs produced at hadron colliders*, Physics Letters B **463** no. 1, (1999) 99 – 103.
<http://www.sciencedirect.com/science/article/pii/S0370269399009454>.
- [140] The ATLAS Collaboration, *Search for the Supersymmetric Partner of the Top Quark in the Jets+ E_T^{miss} Final State at $\sqrt{s} = 13$ TeV*.

- [141] R. D. Cousins, J. T. Linnemann, and J. Tucker, *Evaluation of three methods for calculating statistical significance when incorporating a systematic uncertainty into a test of the background-only hypothesis for a Poisson process*, Nuclear Instruments and Methods in Physics Research Section A: Accelerators, Spectrometers, Detectors and Associated Equipment **595** no. 2, (2008) 480 – 501.
<http://www.sciencedirect.com/science/article/pii/S0168900208010255>.
- [142] J. Linnemann, *Measures of Significance in HEP and Astrophysics*, p. , 35. 2003.
[physics/0312059](#).
- [143] L. Moneta, K. Cranmer, G. Schott, and W. Verkerke, *The RooStats project*, in *Proceedings of the 13th International Workshop on Advanced Computing and Analysis Techniques in Physics Research. February 22-27, 2010, Jaipur, India.* <http://acat2010.cern.ch/>. Published online at <http://pos.sissa.it/cgi-bin/reader/conf.cgi?confid=93>, id. #57. 2010. arXiv:1009.1003 [physics.data-an].
- [144] Calum Macdonald, *Searches for supersymmetry in final states containing b-tagged jets with the ATLAS detector*. PhD thesis, University of Sheffield, 2017.
- [145] P. Jackson, C. Rogan, and M. Santoni, *Sparticles in motion: Analyzing compressed SUSY scenarios with a new method of event reconstruction*, Phys. Rev. **D95** no. 3, (2017) 035031, arXiv:1607.08307 [hep-ph].
- [146] H. An and L.-T. Wang, *Opening up the compressed region of top squark searches at 13 TeV LHC*, Phys. Rev. Lett. **115** (2015) 181602, arXiv:1506.00653 [hep-ph].
- [147] S. Macaluso, M. Park, D. Shih, and B. Tweedie, *Revealing Compressed Stops Using High-Momentum Recoils*, JHEP **03** (2016) 151, arXiv:1506.07885 [hep-ph].
- [148] M. Baak, G. J. Besjes, D. Côte, A. Koutsman, J. Lorenz, and D. Short, *HistFitter software framework for statistical data analysis*, Eur. Phys. J. **C75** (2015) 153, arXiv:1410.1280 [hep-ex].
- [149] ATLAS Collaboration, M. Aaboud et al., *Search for top squarks in final states with one isolated lepton, jets, and missing transverse momentum in $\sqrt{s} = 13$ TeV pp collisions with the ATLAS detector*, Phys. Rev. **D94** no. 5, (2016) 052009, arXiv:1606.03903 [hep-ex].
- [150] The ATLAS Collaboration, “Mctruthclassifier.” <https://twiki.cern.ch/twiki/bin/viewauth/AtlasProtected/MCTruthClassifier>.
- [151] The ATLAS Collaboration, *Jet energy scale measurements and their systematic uncertainties in proton-proton collisions at $\sqrt{s} = 13$ TeV with the ATLAS detector*, Phys. Rev. **D96** no. 7, (2017) 072002, arXiv:1703.09665 [hep-ex].

- [152] The ATLAS Collaboration, *Jet energy resolution and selection efficiency relative to track jets from in-situ techniques with the ATLAS detector using proton-proton collisions at a centre of mass energy $\sqrt{s} = 7 \text{ TeV}$* , <https://inspirehep.net/record/1204034>.
- [153] The ATLAS Collaboration, *Improved luminosity determination in pp collisions in $\sqrt{s} = 7 \text{ TeV}$ using the ATLAS detector at the LHC*, Eur. Phys. J. **C73** no. 8, (2013) 2518, arXiv:1302.4393 [hep-ex].
- [154] ATLAS Collaboration, G. Aad et al., *Performance of algorithms that reconstruct missing transverse momentum in $\sqrt{s} = 8 \text{ TeV}$ proton-proton collisions in the ATLAS detector*, Eur. Phys. J. **C77** no. 4, (2017) 241, arXiv:1609.09324 [hep-ex].
- [155] W. Beenakker, et al., *Squark and Gluino Hadroproduction*, Int. J. Mod. Phys. **A26** (2011).
- [156] G. Cowan, *Statistical Data Analysis*. Oxford science publications. Clarendon Press, 1998. <https://books.google.co.uk/books?id=ff8ZyWOnlJAC>.
- [157] G. Cowan, pp. , 321–355. Springer International Publishing, Cham, 2015. https://doi.org/10.1007/978-3-319-05362-2_9.
- [158] G. Cowan, K. Cranmer, E. Gross, and O. Vitells, *Asymptotic formulae for likelihood-based tests of new physics*, Eur. Phys. J. **C71** (2011) 1554, arXiv:1007.1727 [physics.data-an]. [Erratum: Eur. Phys. J.C73,2501(2013)].
- [159] A. L. Read, *Presentation of search results: The CL(s) technique*, J. Phys. **G28** (2002) 2693–2704. [,11(2002)].
- [160] G. Cowan, et al., *Asymptotic formulae for likelihood-based tests of new physics*, Eur. Phys. J. **C71** (2011), arXiv:1007.1727 [physics.data-an].
- [161] ATLAS Collaboration, G. Aad et al., *ATLAS Run 1 searches for direct pair production of third-generation squarks at the Large Hadron Collider*, Eur. Phys. J. **C75** no. 10, (2015) 510, arXiv:1506.08616 [hep-ex]. [Erratum: Eur. Phys. J.C76,no.3,153(2016)].
- [162] M. Papucci, et. al, *Natural SUSYEndures*, arXiv:1110.6926 [hep-ph].
- [163] ATLAS Collaboration, M. Aaboud et al., *Dark matter interpretations of ATLAS searches for the electroweak production of supersymmetric particles in $\sqrt{s} = 8 \text{ TeV}$ proton-proton collisions*, JHEP **09** (2016) 175, arXiv:1608.00872 [hep-ex].
- [164] N. Arkani-Hamed, A. Delgado, and G. F. Giudice, *The Well-tempered neutralino*, Nucl. Phys. **B741** (2006) 108–130, arXiv:hep-ph/0601041 [hep-ph].
- [165] Planck Collaboration, P. A. R. Ade et al., *Planck 2013 results. XVI. Cosmological parameters*, Astron. Astrophys. **571** (2014) A16, arXiv:1303.5076 [astro-ph.CO].
- [166] ATLAS Collaboration, G. Aad et al., *Search for squarks and gluinos in events with isolated leptons, jets and missing transverse momentum at $\sqrt{s} = 8 \text{ TeV}$ with the ATLAS detector*, JHEP **04** (2015) 116, arXiv:1501.03555 [hep-ex].

- [167] ATLAS Collaboration, M. Aaboud et al., *Search for new phenomena in final states with an energetic jet and large missing transverse momentum in pp collisions at $\sqrt{s} = 13$ TeV using the ATLAS detector*, Phys. Rev. **D94** no. 3, (2016) 032005, arXiv:1604.07773 [hep-ex].
- [168] The ATLAS Collaboration, *Search for dark matter produced in association with bottom or top quarks in $\sqrt{s} = 13$ TeV pp collisions with the ATLAS detector*.

This thesis was typeset using the L^AT_EX typesetting system created by Leslie Lamport.
The body text size is set to 11 pt with *Utopia Regular* with *Fourier* font, part of T_EX Live.
The bibliography was typeset using the ATLAS-paper style.